FUNCTIONALIZED NANOMATERIALS FOR T CELL MONITORING AND IMMUNOTHERAPY

HUANG YINGYING

PhD

The Hong Kong Polytechnic University

2025

The Hong Kong Polytechnic University

Department of Biomedical Engineering

Functionalized Nanomaterials for T cell Monitoring and Immunotherapy

HUANG Yingying

A thesis submitted in partial fulfillment of the requirements for the degree of Doctor of Philosophy

August 2024

CERTIFICATE OF ORIGINALITY

I hereby declare that this thesis is my own work and that, to the best of my knowledge and belief, it reproduces no material previously published or written, nor material that has been accepted for the award of any other degree or diploma, except where due acknowledgement has been made in the text.

_____ (Signed)

Huang Yingying (Name of student)

Abstract

T lymphocytes, particularly their antigen-directed cytotoxicity, are pivotal in harnessing the immune system against cancer. Despite advancements in T cell sensing and immunotherapy, current methods often face efficacy limitations and side effects. In recent years, functionalized nanomaterials have garnered significant attention in biosensing and disease treatment. In this thesis, we developed a novel aggregation-induced emission fluorophore (AIEgen) based nanoprobe capable of targeting mouse CD8+ T cells. This nanoprobe can sensitively and selectively distinguish T cells in different differentiation states based on differences in intracellular pH (pHi) generated by metabolic differences. Furthermore, inspired by the crucial role of mature T lymphocytes in cancer therapy, we fabricated aptamer-functionalized methylgermane nanosheet (mGeNS) probes to detect BRCA1, a gene implicated in T-cell immune function. Moreover, leveraging the exceptional photothermal performance of mGeNS, we engineered a mGeNS-based hydrogel platform with near-infrared (NIR) light-controlled drug release kinetics, enabling mGeNS to maintain effective concentrations and a stable photothermal effect at local tumor lesion sites.

In the first work, we aimed to enable non-invasive monitoring of T cell activation and differentiation states by leveraging distinct cellular metabolic pathways (e.g., glycolysis), which are hypothesized to correlate with different pH_i levels. To achieve this, we designed a novel dual emission enhancement nanoplatform composed of AIE dyes, AIEgen@F127-AptCD8, which enables accurate detection of pHi in T cells to "read" the T cell differentiation process. The nanoprobe exhibits a broadly responsive range for pHi values (9.0 to 4.0) and a highly sensitive narrow range for pHi values (7.4 to 6.0), facilitating non-invasive and reliable pHi detection in different cell states. This work demonstrates the specificity and dynamic detection capabilities of this nanoprobe for indirectly and non-invasively monitoring T cell activation and differentiation states.

In the second work, we developed a new biosensor (GeT-NSs@FAM-cDNA) based on a mGe-nanosheet/aptamer platform for the mutant BRCA1 gene detection. This platform utilizes

mGe-nanosheet as a fluorescence quencher, which has been rarely studied in biosensor detection. Compared to traditional fluorescence quenchers such as graphene and MoS_2, mGeNS offers a wide absorption wavelength from the ultraviolet to the NIR region and excellent fluorescence emission at 640 nm. When bound to an organic small molecule fluorescent aptamer (FAM-cDNA), the fluorescence of oligonucleotides is quenched by the mGe-nanosheet due to Van der Waals forces, resulting in a fluorescence "off" state. Upon the addition of the target DNA, the BRCA1 mutant sequence, the fluorescence is restored ("on" state), enabling detection through ratiometric fluorescence emission signals (I_{520}/I_{640} nm). The platform exhibited high selectivity and sensitivity, which was confirmed using mismatched ssDNA and microRNA sequences. This work demonstrates that GeT-NSs@FAM-cDNA nanoprobes can identify the mutant BRCA1 gene with rapid detection (< 30 min) and good sensitivity at the picomolar level without amplification.

In the third study, we focused on delaying the degradation kinetics of mGeNS and enhancing their photothermal stability for tumor therapy. To achieve this, we developed a composite mGeNS-based hydrogel formulation, termed AIMR, which was constructed by encapsulating polyvinylpyrrolidone-modified and doxorubicin-loaded mGeNS (DOX-mGeNS@PVP) into Ca^{2+}-cross-linked sodium alginate hydrogel. Under near-infrared light (NIR) irradiation, the embedded mGeNS@PVP exhibits an excellent photothermal effect with a photothermal conversion efficiency of 60.6%, promoting AIMR degradation and releasing immunomodulatory substances (DOX-mGeNS@PVP and Ca^{2+} ion). This process triggered endoplasmic reticulum (ER) stress and mitochondrial dysfunction, and accelerates the generation of immune-related biomarkers, thereby synergistically amplifying the immunogenic cycle. Furthermore, the AIMR enhances anti-tumor immunity by increasing CD4+/CD8+ T cell infiltration, reducing regulatory T cells, and increasing inflammatory cytokine secretion. Notably, the amplified immunogenic cycle achieves an abscopal effect, effectively inhibiting the growth of distant untreated tumors. This work highlights the potential of smart photothermal agents in hydrogel-based "all-in-one" immunotherapy and inspires the application of mGeNS-

based therapeutic hydrogel platforms in postoperative cancer treatment and personalized biomedicine.

Publications arising from the thesis

1. **+Huang, Y.**, +Zhang, Q., Lam, C.Y., Li, C., Chen, Y., Zhang, R., Zhong, Z., Yan, J., Chen, J., Yin, B.*, Wong, S.H.D.*, Yang, M.*, An Aggregation-Induced Emission-Based Dual Emitting Nanoprobe for Detecting Intracellular pH and Unravelling Metabolic Variations in Differentiating Lymphocytes, ***ACS Nano***, 2024, 18, 24, 15935-15949
2. **Huang, Y.**, Yin, B., Wong, S.H.D.*, Multicomponent Hydrogels in Clinical and Pharmaceutical Applications, Royal Society of Chemistry Books-Multicomponent Hydrogels: Smart Materials for Biomedical Applications, 2023, Chapter 14, 449-501

Conference Proceeding

1. **Huang, Y.**, Wong, S.H.D.*, Yang, M.*, A pH-Sensitive Nanoprobe Based on AIE and FRET For Real-Time Prediction of Activated T Lymphocyte States, 33rd Biosensors conference, Korea, June 2023. Poster presentation
2. **Huang, Y.**, Wong, S.H.D.*, Yang, M.*, An Aggregation-Induced Emission Luminogen-based Dual Emitting Nanoprobe for Precise Intracellular pH Detection and Unveiling of Metabolic Variation in Differentiating Lymphocytes, Biomedical Engineering Conference (BME2023), Hong Kong, August 2023. Poster presentation
3. **Huang, Y.**, Wong, S.H.D.*, Yang, M.*, 2D $GeCH_3$ Nanosheet-Hydrogel Platform Integrating Photothermal Immunochemotherapy, Chemotherapy and Calcium Overloading Inhibits Tumor Recurrent and Metastatic, 11^{th} WACBE World Congress on Bioengineering, Hong Kong, August 2024. Oral presentation
4. **Huang, Y.**, Yang, M.*, AIEgen nanoparticles for T lymphocyte detection, 2024 Doctoral Academic Forum on Biomedical Sensing and Detection, Zheng Jiang, November 2024. Oral presentation

Acknowledgments

Three years of my PhD journey have swiftly passed by, filled with both challenges and triumphs. This dissertation would not have been possible without the support, guidance, and encouragement of many individuals, to whom I am deeply grateful.

First and foremost, I would like to express my deepest gratitude to my supervisor, Professor Yang Mo, for his invaluable guidance, patience, and unwavering support throughout my doctoral studies. His profound knowledge and insightful advice have been instrumental in shaping my research and academic growth. His dedication to his students and his passion for research have been truly inspiring, and I feel extremely fortunate to have had the opportunity to learn from him.

I am also profoundly thankful to my co-supervisor, Professor Wong, Siu Hong Dexter, for his insightful advice, and encouragement, and for always pushing me to strive for excellence. His expertise and constructive feedback have been crucial in refining my research. His enthusiasm and commitment to high standards have motivated me to overcome numerous challenges and to continuously improve my work. I am deeply appreciative of his mentorship and the opportunities he has provided me.

I would like to express my sincere gratitude to Bohan YIN for her constructive suggestions on the experiment. Her hard work and ambition serve as a role model for all of us. My heartfelt thanks also go to Qin ZHANG for her invaluable assistance when I first entered the laboratory and for her guidance on animal experiments.

I am deeply thankful to Jiareng CHEN and Jiaxiang YAN for their insightful discussions on experiments and their support in paper writing. Special thanks to Kam Ning YUEN and Zhiming ZHONG for their early exploration of Chapter 3 of my dissertation.

In addition, I would like to extend my gratitude to other members of the research group (names not listed in order), including Jingyu SHI, Yadi FAN, Feng TIAN, Kwun Hei Willis HO, Yutian GU, Ruolin ZHANG, Yi LIU, Chuanqi LI, Wen YIN, Yucheng MA, Hu LI, Meng XIAO, Honglian WU, Ching Ying Katherine LAM, Jialei SONG, Fu ZHOU, Huang LAI, Luogen LAI, Fengqi WANG, Zhao HE, Xin YANG, Chenyu TANG, Shu XIAO, and Zipei YU, for their

collaboration, camaraderie, and the stimulating discussions that have enriched my research experience. The sense of community and teamwork within our group has been a constant source of motivation and inspiration for my research. I would like to thank all the members of Professor Youhua TAN's research group for frequently lending me experimental supplies and reagents. Your contributions and friendship have been indispensable to my research and personal growth.

I am also grateful to my good friends at PolyU, Shan LIU, and Shiya WANG, as well as all the members of the Hong Kong 01 WeChat group, for their companionship, support, and for making my time here enjoyable and memorable. Special thanks to every member of the R613 office for creating a stimulating and supportive work environment. Your friendship and encouragement have been a constant source of strength for me.

A special thank you to Dongyang LI for his invaluable suggestions and unwavering moral support. His hard work and ambition have inspired me to push myself further and stay dedicated to my work. Thank you for always being there for me, especially during the most challenging times.

I would also like to acknowledge the joy and excitement brought by the 2024 Paris Olympics, which provided a much-needed respite from the monotony of writing my dissertation.

Lastly, I am deeply indebted to my family for their unwavering support, love, and encouragement. Your belief in me has been the foundation of my perseverance and success. To my parents, siblings, and extended family, thank you for always being there for me, for your sacrifices, and for your constant encouragement. Your love and support have been my greatest source of strength.

Thank you all.

Table of Contents

List of Figures

Figure 2.7 *Ex vivo* expansion of CD8+ T cells and organelle colocalization of AIEgen@F127-AptCD8 nanoprobe. (A) (i) Representative CLSM images of colocalization between AIEgen@F127-AptCD8 (blue channel: $\lambda_{ex}/\lambda_{em}$ = 405/450 nm, red channel: $\lambda_{ex}/\lambda_{em}$ = 405/660 nm) and subcellular organelles (green channel: $\lambda_{ex}/\lambda_{em}$ = 488/520 nm) stained with 100 nM Mito-Tracker Green, Lyso-Tracker Green, or ER-Tracker for 30 min in live activated CD8+ T cell, respectively. The scale bar is 10 μm for all figures. The pseudo-color was used to indicate the mapping of pH_i in different cellular compartments. The color strip indicated the pseudo color change observed upon varying the pH. (ii) Statistics of colocalization using Pearson's correlation coefficient. (iii) The table lists the average pH values for the region of interest (ROI) 1-3 regions. (B) Brightfield photos of CD8+ T cells without and with mouse CD3/CD28 Dynabead™ over Day 1, 3, 5, and 7. The scale bar is 100 μm for all figures. (C) Nonactivated and activated CD8+ T (Day 7) cells were stained by nucleus dye Hoechst 33342 and cell membrane dye Dio. The scale bar is 20 μm for all figures. (D) The cell expansion rate of CD8+ T cells before and after activated using CCK-8 assay. (E) IFN-γ expressing of CD8+ T cells following activation at various time points (Day 0, 1, 3, 5, and 7), n=3. All data are represented as mean ± SD (ns: no significance, *p< 0.05, **p< 0.01, ***p< 0.001, n= 3, one-way ANOVA test). (F) The table shows the statistics of T_N, T_E, and T_{CM} cell subtypes of CD8+ T cells at various time points (Day 0, 1, 3, 5, and 7) following activation. (G) Flow cytometry quantification of the expression profile of surface activation markers (CD44/CD62L) on CD8+ T cells before and after activation. The phenotypes are defined as the following: T_N, $CD44^-CD62L^+$; T_E, $CD44^+CD62L^-$; and T_{CM}, $CD44^+CD62L^+$. (H) The relative proportion of the three T cell subsets on different time points of activation. 48

Figure 2.8 Real-time detection of pH_i in CD8+ T cells and entry mechanism of nanoprobe. (A) Schematic illustration of the *in vitro* experimental design. The naïve CD8+ T cells were primed by CD3/CD8 Dynabead™ over different time points. Dynabead™ was removed before pH_i imaging. T cells on Day 0 are nonactivated. (B) Cellular uptake of AIEgen@F127-AptCD8 nanoprobes in the activated CD8+ T cells under various conditions of untreated (positive control), pretreated with nystatin (100 μM) and chlorpromazine (CPZ, 20 μM) for 6 h. The cells

overloading. (A) mGePVP@SAgel induces an increase of intracellular Ca^{2+} in B16F10 cells under laser irradiation. Cell nuclei were stained with DAPI (blue), and the cells were stained with Fura2-AM dye (green). The scale bar is 50 μm for all figures. (B) Mitochondrial membrane potential of B16F10 cells after AIMR treatments detected by the JC-1 (5,5′,6,6′-tetrachloro-1,1′,3,3′-tetraethylbenzimidazolcarbocyanine iodide) assay. The blue and red channel represents J-monomer and J-aggregate, respectively. The scale bar is 50 μm for all figures. (C) Quantification of intracellular Fura2-AM intensity upon different treatments. (D) The JC-1 ratio (J-aggregate fluorescence/J-monomer fluorescence) was calculated according to CLSM. (E) Quantification of the extracellular ATP expression after treatment with various formulations. (F) Western blot assay and (G) relative expression level quantification of cyto c in the cytoplasm, and cleaved caspase 3 expression levels of B16F10 cells respectively after being treated with G1 (ctrl plus laser), G2 (SAgel), G3 (DOX@SAgel), G4 (AIMR), G5 (mGePVP@SAgel plus laser), and G6 (AIMR plus laser) (980 nm, 1 W cm^2, 10 min). ns: no significance, data are presented as the mean with SD (n = 3 independent samples). The data were analyzed by one-way ANOVA with Tukey's multiple comparisons post-test. 98

Figure 4.12 Antitumor efficacy of AIMR on B16F10 tumor-bearing mice model. (A) Experiment outline showing the treatment steps and procedures for evaluating therapeutic outcomes in B16F10 or B16F10-Luc tumor-bearing mice. N = 5 mice per group. (B) The DOX release behavior was measured by IVIS imaging of B16F10 tumor-bearing mice after the intravenous injection of free DOX or postoperative implantation of AIMR with or without NIR irradiation at various injection periods. (C) The Temperature change in tumor under laser irradiation recorded by an infrared thermal camera. (D) Relative mean of PL intensity of DOX and (E) the temperature change after different treatments. (F) *In vivo* bioluminescence intensity and (G) IVIS images to track the growth of subcutaneous injected B16F10-Luc cancer cells in different treatment groups of mice after surgery (980 nm, 1.0 W cm^{-2}, 5 min). (H) The mouse weight, (I) tumor volume, (J) tumor weight, and (K) survival rate after different treatments. The treatment groups are G1 (Surgery), G2 (SAgel), G3 (DOX@SAgel), G4 (AIMR), G5 (mGePVP@SAgel plus laser), and G6 (AIMR plus laser) for the above experiment. N = 5 mice

List of Tables

List of Abbreviations

AIEgens	Aggregation-induced emission luminogens
pH_i	Intracellular pH
mGe	Methylgermanene
NSs	Nanosheets
NIR	Near-Infrared
ER	Endoplasmic reticulum
APCs	Antigen-presenting cells
TCR	T cell receptor
MHC	Major histocompatibility complex
T_N	Naïve T cell
T_{CM}	Central memory T cell
T_E	Effector memory T cell
TME	Tumor microenvironment
LA	Lactate acid
OXPHOS	Oxidative phosphorylation
ATP	Adenosine triphosphate
TILs	Tumor-infiltrating lymphocytes
Tregs	Regulatory T cells
ELISA	Enzyme-linked immunosorbent assay
DCs	Dendritic cells
ALT	Adoptive lymphocyte transfer
ICB	Immune checkpoint blockade
PD-1	Programmed cell death protein 1
TAAs	Tumor-associated antigens
2D	Two-dimensional
Nps	Nanoparticles
ACQ	Aggregation-caused quenching

MoS_2	Molybdenum disulfide
-COOH	Carboxyl
BRCA1	Breast cancer susceptibility gene 1
AuNPs	Gold nanoparticles
ssDNA	Single-stranded DNA
PTT	Photothermal therapy
ICD	Immunogenic cell death
DAMPs	Damage-associated molecular patterns
AIMR	Accelerated immunomodulatory matrix reservoir
IFN-γ	Interferon-γ
MR	Magnetic resonance
MRI	Magnetic resonance imaging
RIM	Restriction of intramolecular motion
RIR	Restriction of intramolecular rotation
RIV	Restriction of intramolecular vibration
AptCD8	Anti-CD8 aptamer
λ_{ex}	Excitation spectrum
λ_{em}	Emission spectrum
D/A	Donor-acceptor
FRET	Förster resonance energy transfer
NMR	Nuclear magnetic resonance
ESI	Electrospray ionization
PL	Photoluminescence
TEA	Triethylamine
PBS	Phosphate-buffered saline
NHS	N-hydroxysuccinimide
EDC	1-ethyl-3-(3-dimethylaminopropyl) carbodiimide
MES	2-(N-morpholino) ethanesulfonic acid)

CA	Citric acid
mAbs	Anti-mouse monoclonal antibodies
FTIR	Fourier-transform infrared spectrum
DI water	Deionized water
TICT	Twisted intramolecular charge-transfer
SEM	Scanning electron microscopy
DLS	Dynamic Light Scattering
TEM	Transmission electron microscopy
UV-Vis	Ultraviolet-visible
CLSM	Confocal laser scanning microscopy
POC	Pearson's overlap coefficients
ROI	Region of interest
LOD	Limit of detection
2-DG	2-Deoxy-D-glucose
ssDNA	Single-stranded DNA
FAM	Fluorescein amidite
TX100	Triton™ X-100
NMP	N-methyl-2-pyrrolidone
IPA	Isopropyl alcohol
TE	Tris-EDTA
b1mis-DNA	One-base mismatched DNA sequence
b2mis-DNA	Two-base mismatched DNA sequence
nc-DNA	Non-complementary DNA sequence
HRTEM	High-resolution transmission electron microscopy
XRD	X-ray Diffractometer
EEM	Excitation emission matrix
Qe	Quenching efficiency
PTAs	Photothermal reagents

PCE/η	Photothermal conversion efficiency
DOX	Doxorubicin
CAT	Calreticulin
HMGB1	High mobility group box 1
LE	Loading efficiency
T_{max}	Maximum steady temperature
T_{Surr}	Environmental temperature
τ_s	Time constant
IVIS	*In vivo* imaging system
BMDCs	Bone marrow-derived dendritic cells
XPS	X-ray photoelectron spectroscopy
ε	Extinction coefficient
ddH_2O	Double-distilled water
IL-6	Interleukin 6
IFN-γ	Interferon-γ
TNF-α	Tumor necrosis factor α

Chapter 1: Introduction

1.1 Background of T Cell Based Monitoring and Immunotherapy

Cancer remains one of the leading causes of mortality globally, accounting for approximately one out of every six annual fatalities [1]. The development of tumors, particularly malignant ones, arises primarily from the synergistic interplay between genetic determinants and environmental influences [2]. The immune system in safeguarding the host against malignancies has been a focal point of cancer treatment research for decades. T lymphocytes, an integral component of the adaptive immune response, have driven significant advancements in cancer immunotherapy due to their capacity to recognize and eliminate neoplastic cells [3]. The concept of lymphocytes as anti-tumor surveillance mediators was initially proposed by Thomas and Burnett in the mid-20th century, and T cells were later identified as the primary mediators of adaptive immunity [4]. Today, the field of T cell-based cancer immunotherapy is rapidly advancing, addressing the challenges of precisely identifying and characterizing these cells to develop effective T cell detection techniques [5]. The techniques are essential for understanding T cell metabolism and enhancing immunotherapeutic strategies, especially for tumor prognosis [6].

Recently, the convergence of nanotechnology and biotechnology has given rise to the burgeoning field of nanobiotechnology, which has garnered substantial interest amidst the remarkable progress in nanoscale engineering [7-9]. Advancements in functional and molecular imaging biomarkers are enhancing the assessment of targeted therapy efficacy. Nanoprobe imaging technology is an interdisciplinary field that integrates biomedical imaging and materials science and can achieve non-invasive visualization and quantification of the spatiotemporal distribution of biological processes *in vivo* [10]. This powerful approach serves various applications, including diagnostics and therapeutics, particularly in the precise monitoring and manipulation of T cells. This chapter mainly introduces the applications of different functionalized nanomaterials in T cell-based monitoring and immunotherapy.

1.2 Overview of T cell

T cells are divided into two main subsets: CD4+ T cells (helper T cells) and CD8+ T cells (cytotoxic T cells) [11, 12]. Typically, CD4+ T cells orchestrate the overall immune response through interactions with antigen-presenting cells (APCs). In contrast, CD8+ T directly eliminates target cells through cytotoxic mechanisms. This division of labor between the two T cell subsets facilitates a coordinated and effective immune response against pathogens and diseased cells [13]. This section delves deeper into the biology of CD8+ T cells, whose potent cytotoxicity has substantially propelled forward the field of cancer immunotherapy.

1.2.1 T cell Differentiation and Functions

T cell differentiation, encompassing memory and effector subsets, plays a pivotal role in conferring immunity against pathogens [14, 15]. The activation of CD8+ T cells is a multi-step process that ensues after T cell priming. It involves the interaction between the T cell receptor (TCR) and the antigenic peptide-major histocompatibility complex (MHC), the transmission of co-stimulatory or co-inhibitory signals from APCs, and stimulation by extracellular cytokines [16]. Naive CD8+ T cells (T_N) undergo a distinct developmental trajectory upon activation, giving rise to central memory T cells (T_{CM}) and effector T cells (T_E) [17] (**Figure 1.1**). While T_E has a short lifespan, T_{CM} possesses the capacity for long-term persistence. During secondary immune responses, re-exposure to the antigen triggers rapid expansion of memory T cells, eliciting a more robust and expeditious immune reaction compared to the primary response, thereby facilitating efficient pathogen clearance [18]. Although CD8+ T cell subsets undergo autonomous differentiation programs, the kinetics and efficiency of CD8+ T cell proliferation markedly diverge from CD4+ counterparts [19]. Naïve CD8+ T cells appear to initiate their proliferation program more rapidly upon antigen exposure compared to naive CD4+ T cells. In addition, CD8+ T cells exhibit a higher rate of cell division and more rapid proliferation than CD4+ T cells [20]. CD8+ T cells are regarded as the primary drivers of anti-tumor immunity,

delivering pro-apoptotic molecules through the release of cytotoxic granules (perforins or granzymes), thereby inducing targeted cell death [21]. For example, in early-stage colorectal tumors, metastases and occult tumor cells are detectable in the blood, bone marrow, and lymph nodes, potentially exposing systemic effector and memory T cells to infiltrating tumor cells [22]. *In situ* analysis of effector and memory T cells provides insights into the existing cytotoxic capacity and the immune system of responding to tumor cell re-exposure or maintaining equilibrium with cancer [23].

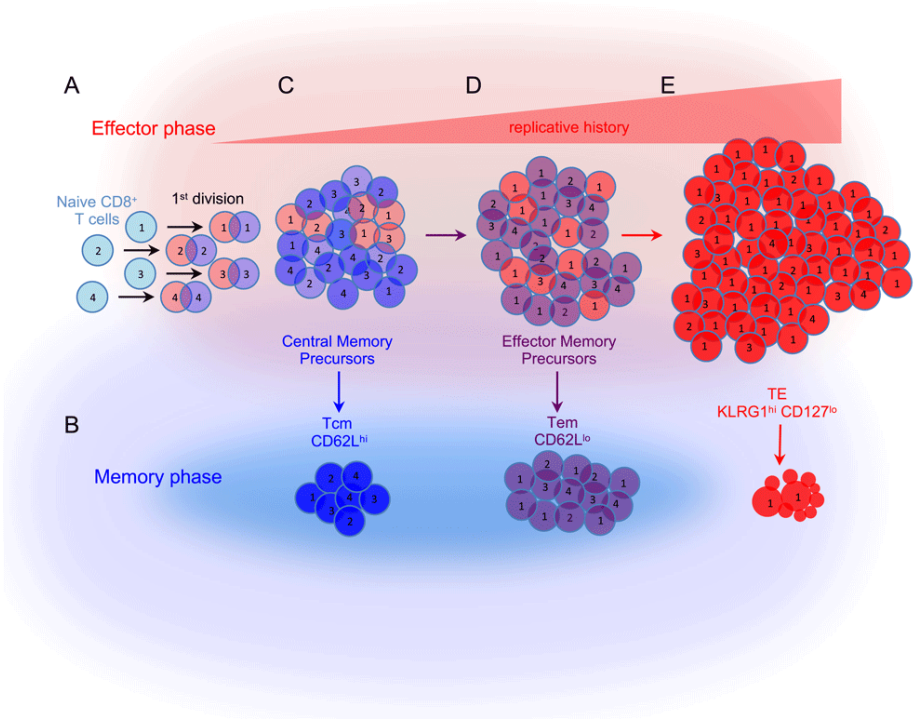

Figure 1.1 Differentiation of CD8+ T cells [24].

The anti-tumor functionality of CD8+ T cells is highly contingent on two crucial factors: CD8+ T cell differentiation and infiltration into the tumor microenvironment (TME) [25, 26]. Various factors and cellular alterations, including DNA methylation [27], transcription factors, cytokines [28], microRNAs [29], and metabolic components [30], contribute to promoting CD8+ T cell differentiation and function (**Figure 1.2**). Among these, metabolic components such as glucose and amino acids (glutamine, tryptophan, and arginine) serve as primary or secondary energy sources driving CD8+ T cell differentiation and function.

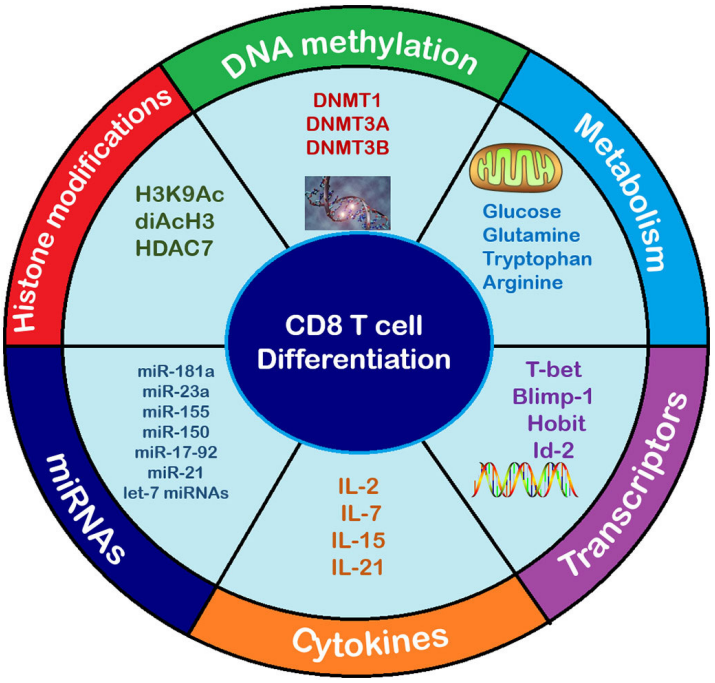

Figure 1.2 Factors that promote CD8+ T cell differentiation [31].

1.2.2 Metabolic Pathways in T cells

Upon activation of the TCR on the surface of CD8+ T cells by APCs of MHC class I, the entry of pyruvate into the mitochondria is inhibited [32] (**Figure 1.3**). Consequently, pyruvate is converted into coenzyme A to participate in the tricarboxylic acid cycle, while cytoplasmic pyruvate is metabolized into lactate by lactate dehydrogenase [33], [34]. This metabolic shift results in an increased reliance on glycolysis with the production of the typical byproduct lactate acid (LA). T_N cells typically exhibit a quiescent state marked by low metabolic activity and catabolic processes. With limited demands for biomolecule synthesis, these cells primarily depend on the oxidative phosphorylation (OXPHOS) pathway of the mitochondrial to generate adenosine triphosphate (ATP) and maintain cellular homeostasis [35]. However, upon activation and expansion, CD8+ T cells undergo a metabolic transition from catabolism to anabolism, where extracellular nutrients drive biosynthesis and ATP production, facilitating proliferation and effector functions [36]. Furthermore, the co-stimulation provided by CD28 enhances the glycolytic activity of CD8+ T cells, thereby facilitating their subsequent proliferation and differentiation.

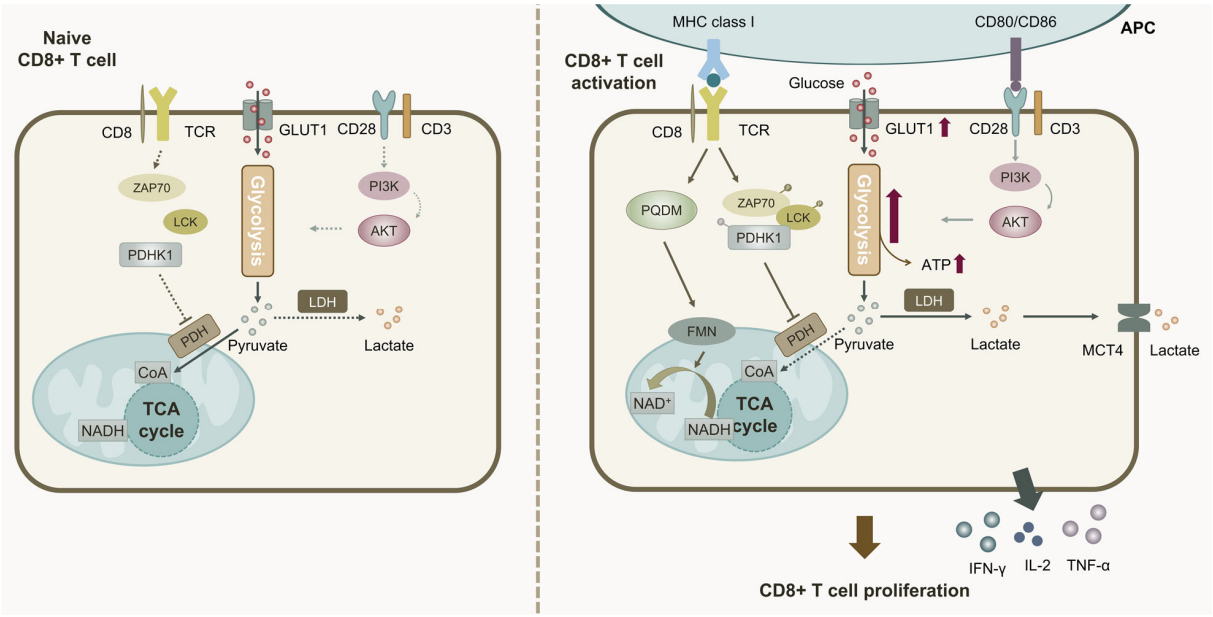

Figure 1.3 Different glycolytic level of naïve and activated CD8+ T cells [37].

1.3 The Importance of Monitoring T Cells

Activated CD8+ T lymphocytes play a crucial role in adaptive immune defense, known for their ability to eliminate cancer cells through multiple mechanisms [38]. Tumor cells evade and impair the adaptive immune system by exploiting mechanisms that normally prevent cytotoxic T cells from mounting destructive autoimmune responses. Therefore, the presence of CD8+ T cells within epithelial tumors has emerged as a robust prognostic marker, indicating better outcomes for numerous tumor types [39]. The specific profiles of these infiltrating immune cells not only correlate with the response to immunotherapy but also serve as valuable indicators, enhancing the ability to predict treatment outcomes across various cancers [40]. This integration of T cell-based monitoring into clinical practice represents a significant stride towards optimizing cancer therapies and improving patient prognoses [3].

1.3.1 T Cell Monitoring Predicts Outcomes in Cancer Therapy

Since T cells express cell-type-specific surface markers, their presence can be more readily estimated within mixed populations comprising tumor, normal tissue, and stromal components [41]. However, different conclusions have been drawn regarding the prognostic value of tumor-

infiltrating lymphocytes (TILs) subsets across various malignancies [42]. While the most common prognostic association is with CD8+ cytotoxic T cells, the presence of FOXP3+ regulatory T cells (Tregs) has also been observed in certain cancers [43]. Emerging studies have revealed elevated levels of Tregs within the total T cell populations isolated from tumor tissue or peripheral blood in patients with various cancers, including breast cancer [44]. Notably, several studies have demonstrated a correlation between intertumoral Tregs and tumor pathogenesis. Understanding the role of different regulatory TIL subsets in the immunopathogenesis of individual cancers is essential for developing effective antitumor immunotherapies.

Moreover, certain genes influencing tumor cell susceptibility to T cell-mediated killing hold prognostic significance. Hu *et al.* employed computational biology approaches to identify hub genes that modulate the sensitivity of tumor cells to TILs, with a particular focus on the STTK gene, which exhibits differential expression in head and neck squamous cell carcinoma [45]. The differentially expressed genes in tumor cells exhibited an enrichment of the STTK gene, and its associated pathway is anticipated to emerge as a potential target for personalized immunotherapy in the treatment of head and neck squamous cell carcinoma, thereby providing a novel therapeutic approach for the management of this malignancy.

1.3.2 Current Approaches of T Cell Monitoring

Evaluation of T lymphocyte subsets and cellular immune function has become an important tool for diagnosis and treatment monitoring of various infectious diseases. Over the years, the field of immune monitoring and a vast array of immunological research has been heavily reliant on immunohistochemistry, and immunofluorescence imaging to assess and quantify cellular heterogeneity and its disease-related implications. Despite their contributions, these methodologies are constrained by their ability to analyze only a limited number of parameters at one time, which in turn impedes a thorough characterization of cellular identities and the intricate composition of cell populations [46].

In contrast, the immune score quantifies tumors based on immune cell infiltration, serving as

a prognostic tool. Early immune scoring methodologies involved the use of whole-section tissue samples stained with immunohistochemistry techniques to manually or digitally quantify CD3+ and CD8+ TILs within the central and invasive margins of the tumor [47]. Cutting-edge advancements in immune scoring leverage comprehensive molecular data obtained through multiplexed imaging approaches, facilitating the concurrent visualization of numerous immune markers within a single tissue section, thereby providing an *in situ* perspective [48]. However, this approach relying on subjective interpretation of stained tissue sections is prone to variability and inaccuracies arising from inconsistencies in staining protocols and result interpretation.

Analyzing the functionality of antigen-specific T cells frequently relies on cytokine detection techniques, including the detection of intracellular cytokines by employing multiparameter flow cytometry and enzyme-linked immunosorbent assay (ELISA), and the evaluation of cytokine mRNA levels through real-time reverse transcription-polymerase chain reaction to monitor the cytokine response of T cells to specific antigens [49]. However, these techniques face significant challenges, including high false positive rates, time-consuming procedures, complexity, and susceptibility to contamination, making them unsuitable for processing large numbers of specimens [50]. Researchers have been increasingly drawn to the domain of single-cell sequencing, driven by the swift progress in technology that has yielded highly precise, sensitive, and high-throughput methodologies for obtaining intricate, multi-dimensional transcriptomic profiles from individual cells [51]. These advancements are instrumental in uncovering previously unknown cellular states and enriching our comprehension of cellular diversity [52]. Meanwhile, emerging technologies including mass cytometry and single-cell RNA sequencing have significantly contributed to our understanding of T cell lineage evolution [53]. These innovative tools are also poised to probe the functionality of antigen-specific T cells within the TME. However, these methodologies typically necessitate cell fixation or lysis, which impedes the capability to track the dynamic fluctuations in transcriptomic and proteomic profiles within the same cell in real-time [54].

Given the crucial role of the immune system and TILs in cancer progression and response to therapy, there is a growing interest in developing immunobiosensing strategies for cancer diagnosis and treatment monitoring. In addition, comprehending immune infiltration within the TME is crucial for improving response rates and advancing the development of novel immunotherapeutic strategies for cancer treatment. Immunobiosensors are analytical devices that leverage the precise interactions between antibodies or other biomolecules and their respective targets to detect and quantify specific analytes in biological samples [55]. Therefore, immunobiosensors can be designed to detect and monitor various immune-related biomarkers, such as cytokines, immune cell subsets, or tumor-associated antigens/genes, providing valuable insights into the immune response in the TME [56].

1.4 Cancer Immunotherapy

Building upon the understanding of immunobiosensing strategies and the role of the immune system in cancer prognosis, the field of cancer immunotherapy aims to harness and enhance the *in vivo* natural immune defenses to combat malignant cells. Immunotherapy has emerged as a promising approach to complement traditional cancer treatments, offering the potential for more targeted and personalized therapeutic interventions. A robust and coordinated immune response possesses the capability to eradicate or compromise the functionality of malignant cells. The following section will explore the fundamental principles underlying cancer immunotherapy, including the intricate cancer immunity cycle, as well as the current approaches and strategies employed to modulate and amplify antitumor immune responses [57].

1.4.1 Principle of Cancer Immunotherapy

Conventional adjuvant cancer therapeutic strategies, including chemotherapy and radiotherapy, can inhibit tumor growth but are hindered by off-target toxicity and limited tumor retention. Recently, cancer immunotherapy has emerged as a promising approach for preventing and inhibiting tumor recurrence after surgery [58]. Immunotherapy operates through various mechanisms: either by enhancing the inherent capabilities of the immune system to more

effectively recognize and destroy cancer cells, or by synthesizing analogs of immune system elements to restore or augment the ability of the immune system to target and eliminate cancer cells [59]. This therapeutic approach aims to make the immune system both more vigorous and more intelligent in its fight against cancer. However, certain tumors generate an immunosuppressive microenvironment characterized by increased expression of immune checkpoint molecules, decreased expression of tumor antigens, and limited infiltration of circulating immune effector cells [60]. These non-immunogenic, non-inflamed ("cold") tumors have a reduced response to immunotherapy and can effectively evade antitumor immune responses. In contrast, inflamed ("hot") tumors are often associated with an immunogenic phenotype, high-density T-cell infiltration, molecular signatures of immune activation, and higher immunotherapy response rates [61].

The cancer immunity cycle is essential for effectively targeting and eliminating cancer cells, involving a sequence of immune responses that unfold in distinct stages. This cycle highlights the intricate process by which the immune system identifies and destroys tumor cells through a series of interdependent steps. Initially, when tumor cells undergo apoptosis or necrosis, they release tumor antigens that are captured by APCs, such as tumor-associated macrophages and dendritic cells (DCs) (**Figure 1.4**) [62]. DCs transport the captured antigens to lymph nodes, thereby generating more tumor-specific CD8+ T cells that bind to tumor cells. The binding triggers the destruction of cancer cells through apoptotic mechanisms, releasing antigens and perpetuating the immune response. This continuous cycle of recognition, attack, and antigen release fuels an ongoing and effective immune attack against the tumor.

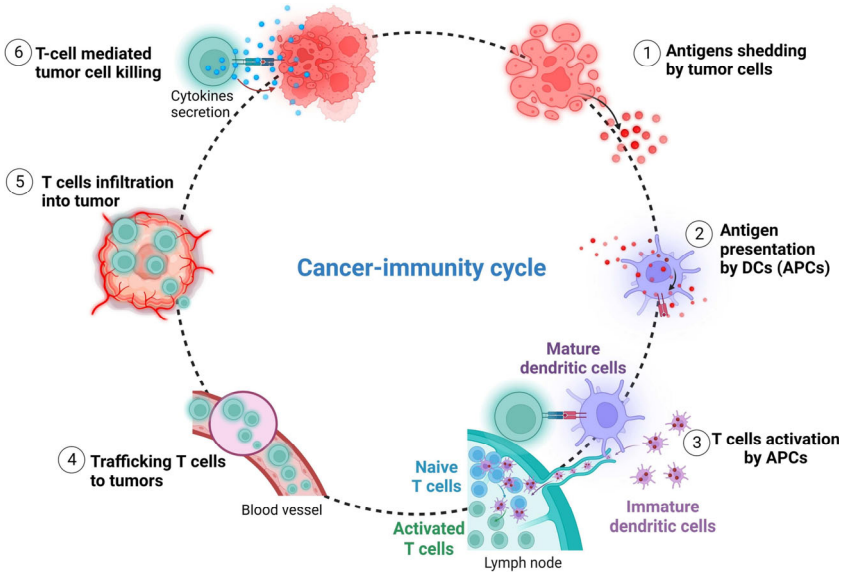

Figure 1.4 Schematic diagram of the immune cycle [62].

The effectiveness of therapies aimed at enhancing anticancer immune responses is significantly impacted by various factors. Adverse TME characterized by its immunosuppressive profiles often correlates with diminished treatment success in cancer therapies. This environment may encompass a variety of immune cells like TAMs, Tregs, NK cells, tumor-associated fibroblasts, and neutrophils, all contributing to immune evasion by the tumor [63].

1.4.2 Current Approaches for Cancer Immunotherapy

Multiple immunotherapeutic strategies are being developed to enhance immune infiltration and activation, including adoptive lymphocyte transfer (ALT), immune checkpoint blockade (ICB), and cancer vaccines [64, 65].

In addition to cancer vaccines, ALT has emerged as a prevalent form of immunotherapy, involving extracting T cells from a cancer patient, identifying antitumor clones, and expanding these cells *in vitro* [66]. In some cases, T cells that target unspecified tumor antigens are also isolated directly from tumor tissues and cultivated. These T cells are then reinfused into the patient, often accompanied by cytokines and/or adjuvants to boost their proliferation and efficacy. ALT offers a significant advantage over traditional cancer vaccines by bypassing the

need for in-patient expansion of tumor-specific T cells, which is particularly challenging in immunocompromised individuals [67].

ICB has received much attention due to its recent successes and has received FDA approval for use in a variety of cancer types. The overall goal of immune checkpoint therapy is to overcome tumor-mediated T cell dysfunction and allow T cell activation, maintaining effector function [68]. "Immune checkpoints" are co-inhibitory molecules located on the surface of T cells that, along with co-stimulatory molecules such as CD28, function to regulate T cell activation [69]. Typically, tumor cells and APCs within the TME often express co-inhibitory ligands that bind to co-inhibitory immune checkpoints on T cells, thereby inhibiting T cell activity. The two best-known co-inhibitory checkpoints are programmed cell death protein 1 (PD-1) and cytotoxic T-lymphocyte-associated antigen 4 [70]. It is the balance of these two molecules that directs an adequate T-cell response to a specific pathogen. Without co-inhibitory molecules, a sustained T cell response in situations such as infection may result in tissue damage and autoimmunity. However, on the other hand, disproportionate co-inhibitory signals may result in an inadequate T-cell response.

Therapeutic cancer vaccines are designed to stimulate immunity by administering preidentified or unknown antigens in the form of DCs, peptide fragments, viruses, or nucleic acid constructs [71]. This stimulation is intended to enhance endogenous immune responses that have failed in their cancer surveillance mission [72]. For example, DCs can be subjected to *ex vivo* stimulation with pro-inflammatory agents and subsequently loaded with tumor-associated antigens (TAAs), thereby generating DCs-based cancer vaccines. This activation leads to morphological alterations that bolster their capacity to activate naive T cells, marked by the enhanced expression of MHC classes I and II, and co-stimulatory molecules on their surface [73]. Unlike ICB and other forms of immunotherapy, which may trigger off-target autoimmune responses, DC vaccines exhibit a minimal risk of severe treatment-related adverse effects [74]. Preidentified antigen cancer vaccines TAAs have been extensively studied in previous studies, despite limited therapeutic efficacy [75]. Personalized cancer vaccines, designed to elicit immune responses against neoantigens, have attracted considerable attention [76]. However, their

widespread clinical implementation remains limited by several challenges, including the complex neoantigen identification process, the complexity of rapid vaccine manufacturing, and insufficient immune responses.

Cancer immunotherapies have shown promise across a variety of malignancies. The therapeutic outcomes demonstrate substantial heterogeneity among different cancer types and individual patients [77]. Furthermore, these immunotherapeutic approaches often need to be used in combination with other treatment modalities, as monotherapy has limited efficacy. Because these immunotherapy methods frequently fail to elicit desired responses in the majority of "cold" tumors [78]. Notably, the immune score based on the evaluation of "cold" and "hot" tumor phenotypes has demonstrated superior prognostic value compared to the traditional TNM staging system. Consequently, the pursuit of novel strategies that can simultaneously target and eradicate tumor cells while concurrently eliciting tissue-specific immune responses has emerged as a prominent area of investigation within the field of clinical cancer research.

1.5 Application of Nanomaterials in T cell Monitoring and Immunotherapy

Recently, the exploitation of diverse nanomaterials has garnered increasing research interest as diagnostic nanoprobes or therapeutic platforms for *in vitro* and *in vivo* applications (**Figure 1.5**) [79, 80]. Nanomaterials have emerged as significant tools in cancer research and diagnosis, attributed to their tiny size, favorable biocompatibility, and substantial atomic number. Advances in nanotechnology have led to promising developments in several aspects of cancer management, targeted drug delivery, genetic monitoring, biomarker detection, and enhancements in immunotherapy techniques. These innovations highlight the potential of nanotechnology to refine and revolutionize approaches to cancer treatment and monitoring.

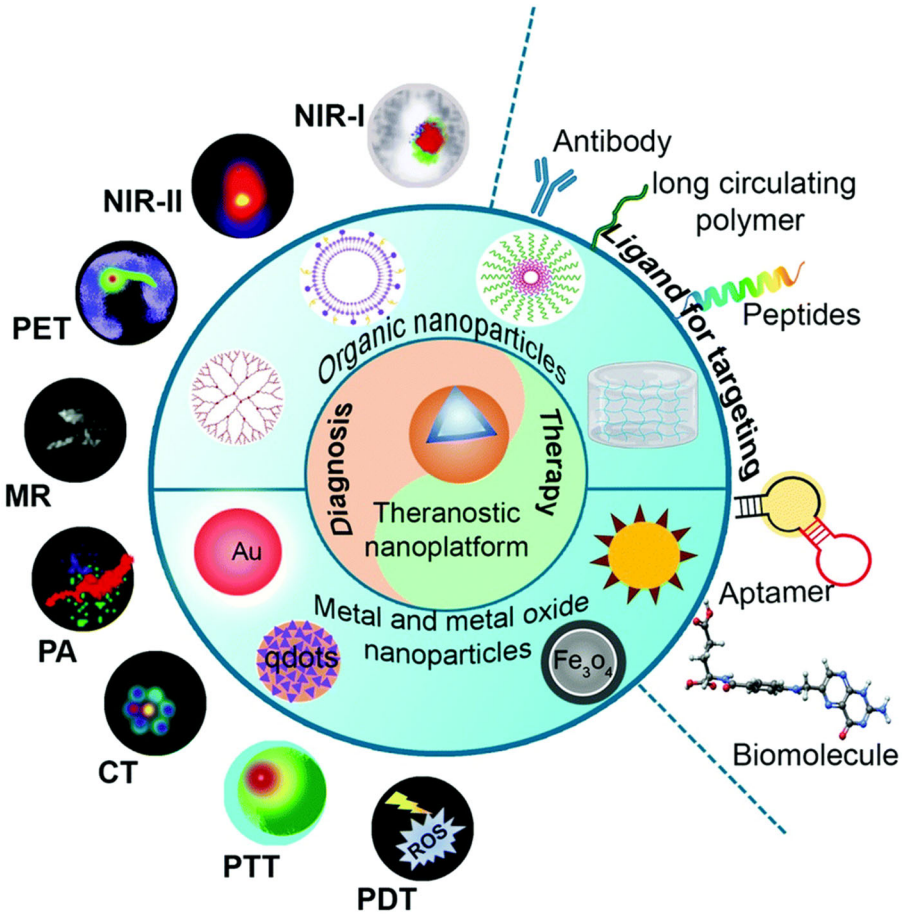

Figure 1.5 Schematic illustration of the diagnostic and therapeutic applications of nanomaterials [81].

1.5.1 Overview of Nanomaterials

Depending on the shape, nanomaterials can exhibit diverse morphologies spanning zero-dimensional (e.g. quantum dots), one-dimensional (e.g. nanorods), two-dimensional (2D, e.g. nanosheets), or three-dimensional structures (e.g. nanosphere, nano gel) [82, 83]. Owing to their distinctive biological functionalities and advantageous biomedical properties, these nanomaterials have garnered extensive development for applications in biomedical engineering [84, 85]. Within the biomedical domain, nanomaterials have garnered significant interest for applications in drug delivery and controlled release systems, owing to their ability to enhance permeability across biological barriers and improve biocompatibility [86, 87]. Furthermore, aptamers are regarded as prospective substitutes for antibodies across numerous domains. The facile introduction of aptamer modifications onto nanomaterials renders them promising candidates for a diverse array of diagnostic and therapeutic applications [88], [89]. Consequently,

this characteristic confers improved efficacy to nanomaterial-based treatments while concurrently mitigating their cytotoxicity towards healthy cells [90]. Below we mainly introduce the three functional materials used in this thesis: fluorescent nanoparticles (Nps), and 2D nanosheets.

Fluorescent Nps have diverse and distinctive optical and electronic properties, as well as facile surface functionalization [91]. Consequently, a variety of organic fluorescent Nps are anticipated to emerge as novel tools for *in vitro* and *in vivo* applications such as bioimaging, diagnostics, drug delivery, and therapy [92], [93]. While exhibiting strong fluorescence in solution, these organic small molecules fluorescent materials often display weak or quenched emission at high concentrations or upon aggregation, a phenomenon termed the aggregation-caused quenching (ACQ) effect [93]. The ACQ phenomenon poses significant limitations on the practical application of organic light-emitting materials [94]. To address this issue, aggregation-induced emission luminogens (AIEgens) have been developed with the primary objective of preventing close intermolecular interactions, thereby reducing the likelihood of quasi-molecule formation [95].

Graphene has sparked considerable interest in 2D layered materials, leading to extensive research efforts in this field [96, 97]. Scientists have made significant progress in developing diverse 2D materials, aiming to surpass the properties of graphene [98, 99]. These materials include transition metal dichalcogenides, such as molybdenum disulfide (MoS_2) [100] and tungsten diselenide [101], hexagonal boron nitride [102], boron nitride-carbon [103], transition metal oxides and hydroxides [104], as well as graphene-like structures such as silicene [105], germanene [106], and stanene [107]. These materials offer unique properties and potential applications in various fields, fueling their widespread attention in recent years [108, 109]. These nanosheets, akin to other materials in the 2D category, boast an exceptionally high ratio of surface area to volume [110]. This characteristic enables their employment as versatile nanoplatforms capable of carrying diverse functional molecules, biomolecules, and pharmaceuticals, thereby facilitating the creation of biological probes or systems for drug delivery [111]. Additionally, the distinctive optical characteristics of 2D nanosheets render them suitable for applications in optical

biosensing and phototherapy [112]. Certain 2D nanosheets exhibit potent fluorescence quenching capabilities, positioning them as novel and effective nano quenchers within the realm of sensitive fluorescent biosensors [113]. Given these distinctive characteristics, 2D nanomaterials have emerged as compelling platforms for a range of cancer theragnostic applications, showcasing their potential in both diagnosis and therapy [114].

1.5.2 Nanomaterials in T Cell Monitoring

Recent progress in nanotechnology, specifically the capacity to manufacture nanoparticles with tailored physicochemical characteristics and highly tunable surface modifications in a precise manner, has led to the development of advanced immunosensors. These sensors integrate the specificity and multifunctionality of antibodies, aptamers, proteins, and other biomolecules with the unique properties inherent to nanoparticles [115]. This synergistic combination has facilitated the design of enhanced immunosensing platforms, leveraging the strengths of both Nps and biomolecular recognition elements [116]. The methods employed to immobilize antibodies or aptamers on the surface of Nps are primarily contingent upon the nature of the interaction with the surface. Consequently, antibodies can be immobilized onto NPs surfaces through non-covalent or covalent binding, affinity-based interactions, or encapsulation processes. The chosen immobilization approach influences the overall performance and characteristics of the resulting immunosensing platform.

Non-covalent immobilization relies on adsorption facilitated by weak interactions, including electrostatic forces, hydrophobic interactions, and van der Waals forces. This approach is relatively cost-effective and time-efficient, typically involving a simple washing procedure for the nanoparticles, followed by incubation with the desired antibody and subsequent removal of excess unbound antibodies [117]. However, this method has several drawbacks, such as the inability to ensure efficient and specific immobilization, weak binding interactions, and potential loss of a portion of the antibodies during subsequent experimental processes [118]. On the other hand, the most widespread method for immobilizing antibodies on nanoparticles and other surfaces is through covalent bonds. This approach allows for increased utilization of

antibodies and, therefore, improved detection capabilities. The presence of free amine and thiol groups in the antibody chain allows for covalent bonds to be formed using different chemistries. The most used is carbodiimide chemistry following the widely used EDC/NHS approach, by forming an amide bond between the carboxyl (-COOH) and free amine groups of the antibody, and Maleimide conjugation to -SH [119].

Breast cancer susceptibility gene 1 (BRCA1) is a tumor suppressor but can increase the risk of breast cancer after mutations. Researchers indicate that reduced expression levels of the BRCA1 gene are associated with elevated counts of CD8+ TILs and inferior survival outcomes in breast cancer patients [120]. Consequently, precise detection of BRCA1 expression becomes a particularly crucial method for quantifying the extent of T cell activation. Liu et al. proposed a label-free fluorescence approach for BRCA1 gene detection utilizing hairpin DNA-templated copper nanoclusters CuNCs (**Figure 1.6A**) [121]. In the absence of the target DNA, the system exhibited strong red emission. Conversely, upon the introduction of the BRCA1 gene, the DNA probe hybridized with the target, inducing a conformational change that led to a decrease in the emission peak intensity. Zhong et al. developed an innovative dual-channel biosensor for the sensitive and precise detection of the BRCA1 gene and thymidine kinase gene, drawing inspiration from gold nanoparticles (AuNPs) loaded with single-stranded DNA (ssDNA), which serve as gene-specific recognition probes and energy acceptors (**Figure 1.6B**) [122]. Upon interaction with the BRCA1 gene target, the complementary binding results in the specific release of carbon dots from the AuNPs. This release triggers a fluorescence recovery, signaling the presence of the BRCA1 gene. Conversely, when the thymidine kinase gene target is detected, it causes the release of a hairpin structure, leading to fluorescence quenching. Nevertheless, both approaches rely on single-channel fluorescence detection, which may interfere with background fluorescence and external environmental factors.

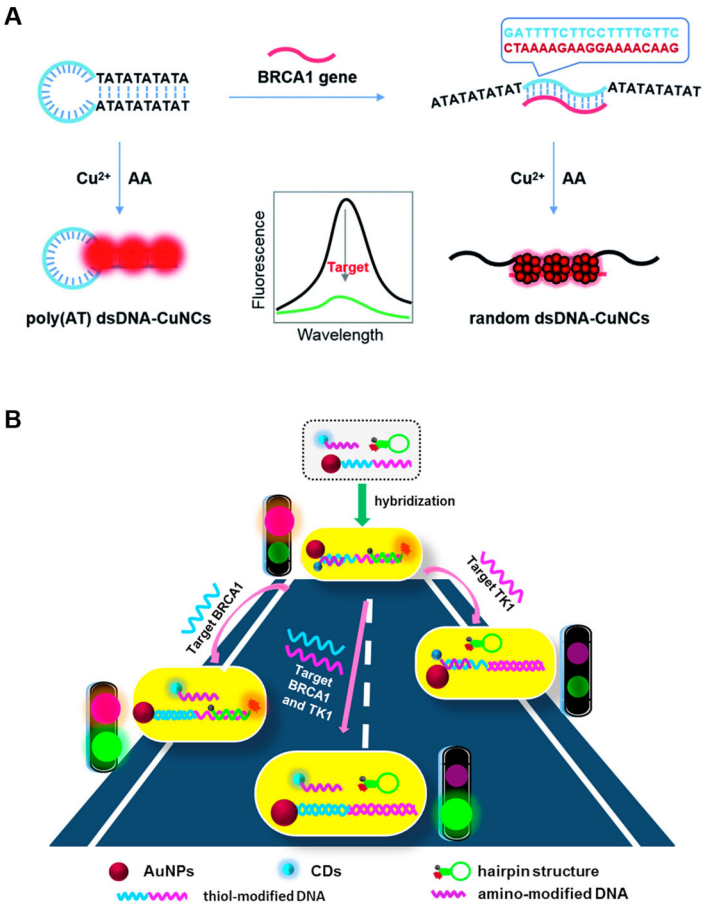

Figure 1.6 Schematic illustration of the (A) DNA-CuNCs-based fluorescent sensor (B) dual-channel sensing strategy based on the synergy of AuNps and CDs [121, 122].

Although numerous studies have investigated the utilization of nanomaterials for optically detecting T cell-related biomarkers and genes, there remains a scarcity of research focusing on their potential for specifically identifying and detecting T cells. Li et al. designed a series of AIE probes (R-TPE-PEG-Chol) for detecting cholesterol on the surface of activated T cells [123] (**Figure 1.7**) . Notably, among these probes, COOH-TPE-PEG-Chol remains non-fluorescent upon integration into the membranes of quiescent T cells. Upon T cell activation, the clustering of TCR triggers the aggregation of membrane cholesterol, prompting the AIE-driven fluorescence emission from COOH-TPE-PEG-Chol. The escalation in fluorescence intensity aligns positively with the activation status of T cells. Nevertheless, this research overlooks discussions on probe sensitivity and the exploration of T cell subtypes post-activation.

Furthermore, the single-emission signal of the fluorescent probe with short emission wavelength (478 nm), fails to mitigate background fluorescence interference.

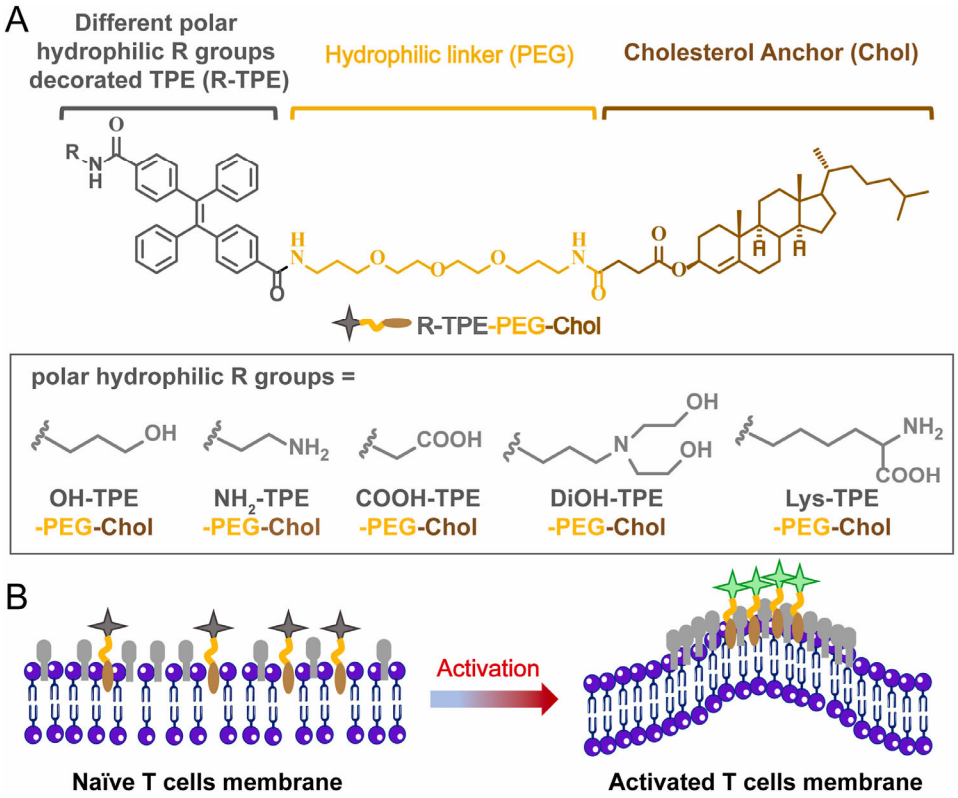

Figure 1.7 Schematic of an AIE probe that visualizes TCR nanoclusters for real-time monitoring of T cell activation [123].

1.5.3 Nanomaterials in T Cell Based Cancer Immunotherapy

Numerous varieties of 2D nanosheets typically demonstrate robust absorption in the near-infrared (NIR) spectrum, rendering them promising options for photothermal therapy (PTT) in cancer treatment [124]. Furthermore, the exceptional specific surface area of 2D nanosheets, along with other advantageous factors, renders them excellent carriers for chemotherapeutic drugs. This enables their seamless integration with chemotherapy, resulting in a synergistic treatment approach that significantly enhances the efficacy of photo-triggered immunotherapy. Importantly, 2D nanosheet-based PTT has the potential to convert immunologically "cold" tumors into the immune-responsive "hot" phenotype through the mechanism of immunogenic cell death (ICD).

Wong *et.al* introduced a novel theragnostic platform, $FePSe_3$@APP@CCM, which incorporates an anti-PD-1 peptide within its core and is enveloped by a CT26 cancer cell membrane (**Figure 1.8**) [125]. This construct serves as a versatile agent for magnetic resonance and photoacoustic imaging, as well as for combined PTT and ICB treatments. The $FePSe_3$@APP@CCM complex demonstrated its ability to effectively eradicate tumors and suppress their growth through PTT, initiated by NIR laser stimulation. This thermal effect also elicited an immune response. Concurrently, the anti-PD-1 peptide component disrupted the PD-1/PD-L1 interaction, thereby enhancing the activity of cytotoxic T cells and fostering robust anti-tumor immunity. The findings from this research underscore the promise of FePSe3-based biomaterials as innovative agents for theragnostic applications. However, modification of the tumor membrane with nanosheets to selectively target tumor cells but simultaneous loading of anti-PD-1 peptides or antibodies to selectively target T cells may inadvertently lead to the destruction of certain T cells within the TME.

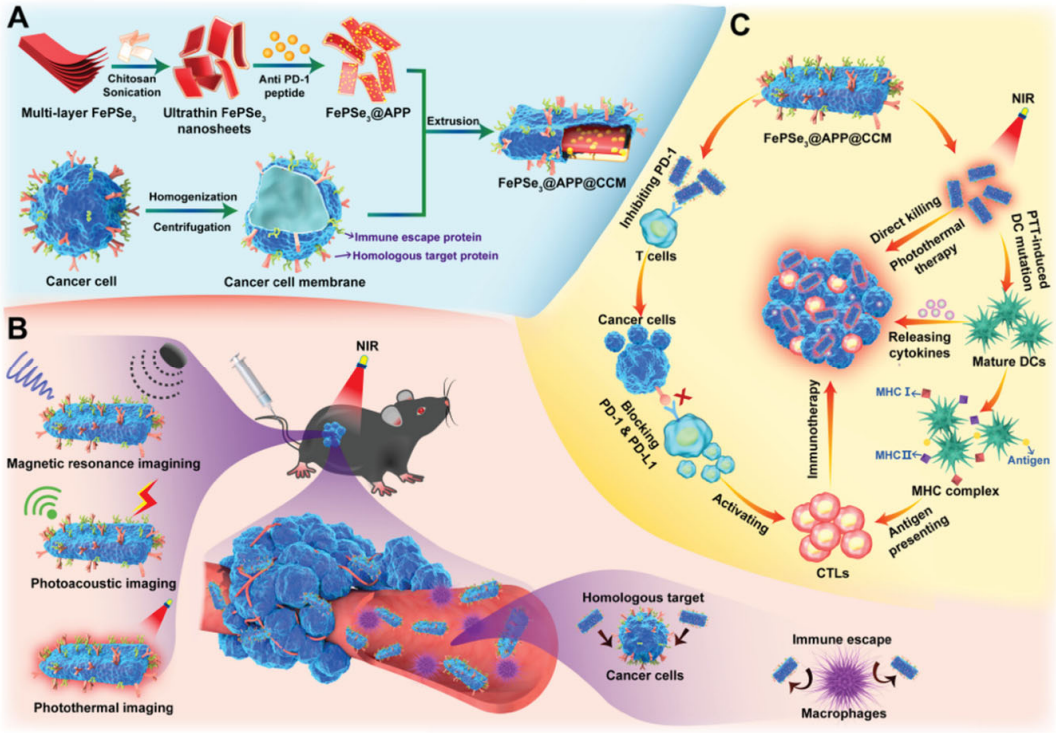

Figure 1.8 Preparation of $FePSe_3$@APP@CCM NSs and their application in tumor therapy [126]. (A) Synthesis route of $FePSe_3$@APP@CCM NSs. (B) Effective multimodal tumor imaging of $FePSe_3$@APP@CCM. (C) Mechanism of $FePSe_3$@APP@CCM for synergistic photothermal

immunotherapy.

In addition, many studies have reported the application of hydrogels in cancer treatment due to their unique porous structure, swelling properties, mechanical properties and biocompatibility [127, 128]. To enhance the structural integrity of hydrogels, a range of nanocomposites-including carbon-based nanomaterials, metals nanoparticles, 2D nanomaterials, and metal oxides nanoparticles have been incorporated as reinforcing "guests" within the hydrogel matrix [129, 130]. Furthermore, hydrogels are designed to intelligently respond to environmental stimuli, undergoing structural changes in response to external factors such as temperature, light, pH value, redox potential, magnetic fields, and ultrasound. These conformational adjustments enable the controlled release of encapsulated drugs or nanomaterials, offering a targeted and efficient approach to treatment. Injectable *in situ* forming hydrogels represent a suitable local drug delivery alternative to postoperative intracavitary implants for the prevention of cancer recurrence and distant metastasis [131] (**Figure 1.9**).

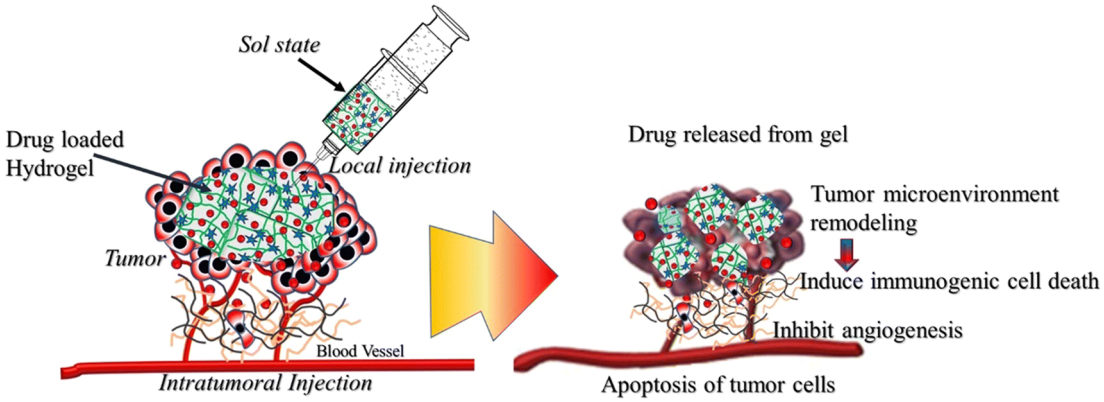

Figure 1.9 Schematic diagram of hydrogel-based tumor treatment [131].

Locally injected hydrogel therapeutics can induce ICD in cancer cells through specific treatment regimens, including chemotherapy, photodynamic therapy, and photothermal therapy (**Figure 1.10**). These treatments generate damage-associated molecular patterns (DAMPs) within cancer cells. Subsequently, TAAs can be phagocytosed by APCs, thereby spontaneously activating innate immune responses against cancer cells. Wang *et al.* have developed an injectable hydrogel that is sensitive to NIR light and capable of provoking an immune response

[132]. This hydrogel is engineered by integrating nanoparticle technology with hydrogel scaffolds that form *in situ*, aiming to directly address tumors that are surgically accessible while also promoting a systemic immune response to target metastatic cancerous lesions. Jia *et al.* designed a simple hydrogel adjuvant featuring uniformly organized nanoscale microstructures by utilizing self-assembling peptides coordinated with manganese ions (Mn^{2+}). The hydrogel demonstrated sustained release of Mn^{2+} *in vivo*, thereby promoting antibody production at levels comparable to those of traditional aluminum-based adjuvants. In summary, these studies present a well-defined hydrogel adjuvant as a proof-of-concept, simplify the design of vaccine adjuvants, and open new avenues for "on-demand" immune modulation strategies. However, these approaches still face limitations, such as insufficient long-term immune response, poor mechanical properties of hydrogels, and inability to release drugs in a controlled manner.

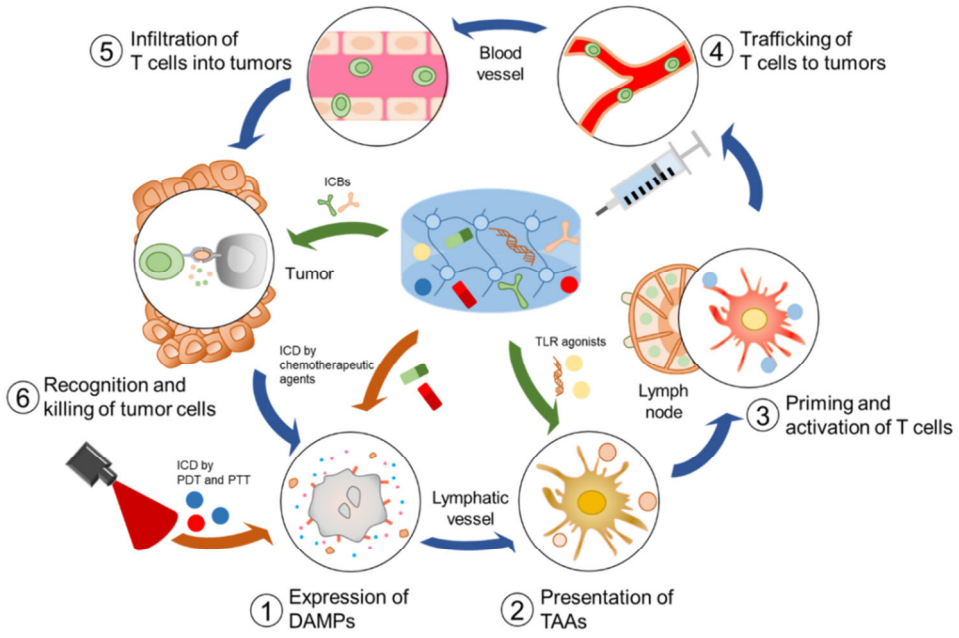

Figure 1.10 Schematic diagram of the injectable hydrogel-based cancer immunity cycle [133].

1.6 Research Gaps and Objectives of the Study

Nanomaterials have demonstrated considerable promise in the realms of cancer diagnosis and treatment, offering innovative approaches through targeted drug delivery, enhanced imaging, and the potential for personalized therapies. This thesis is dedicated to investigating the synthesis and fabrication of various functionalized nanomaterials, along with their potential

applications in the detection of T-cells and the advancement of immunotherapeutic strategies. The structure of this thesis mainly focuses on the following three projects.

Chapter 2 aims to facilitate the non-invasive monitoring of T cell activation and differentiation statuses by exploiting distinct cellular metabolic pathways hypothesized to be associated with different intracellular pH (pH_i) levels. We have designed a novel dual-channel enhancement AIEgen nano platform which enables accurate detection of pH_i of T cells to "read" the T cell status. Critically, we reveal that activated lymphocytes show lower pH_i than the non-activated ones and this decreased pH_i is highly associated with the promoted glycolytic process in differentiating cells. The potential implications of our research are significant, as the ability of our nanoprobe to selectively and precisely "read" pH_i levels in T cells with distinct physiological states holds great promise for advancing our understanding of T cell dynamics and immune responses.

Chapter 3 focuses on the non-invasive detection of the breast cancer mutation gene BRCA1. We developed a novel biosensor based on mGeNS, a 2D nanomaterial that has been rarely explored in the field of biosensing. Our objective was to investigate the relationship between the size of these nanosheets and their photophysical properties. We demonstrated that mGeNS not only possesses a wide absorption wavelength range but also exhibits excellent fluorescence emission at 640 nm, which is distinct from traditional fluorescence quenchers such as graphene and MoS_2. Subsequently, we fabricated an aptamer-based mGeNS platform and investigated its sensing capability for the detection of the BRCA1 gene. Our findings demonstrated that this platform could achieve rapid detection of BRCA1 at picomolar concentrations within 0.5 h based on ratiometric fluorescence sensing. In future work, we will further explore the effect of BRCA1 gene mutation on T-cell activation and function. This work bridges the gap in the application of mGeNS in the field of nucleic acid biosensing, elucidates the impact of BRCA1 gene mutation on T-cells, and lays the foundation for the utilization of mGeNS in biomedical sensing applications.

Chapter 4 delves deeper into the application of mGeNS in photothermal-triggered immunotherapy and addresses two key challenges. Firstly, we solve the shortcomings of the

rapid degradation of mGeNS by encapsulating them into a hydrogel platform. Secondly, this platform addresses the obstacle of insufficient immunogenicity in current immunotherapy by accelerating the ICD efficacy based on the induction of ER stress and mitochondrial dysfunction. This process enhances the immunogenic cycle and anti-tumor immunity by increasing CD4+/CD8+ T cell infiltration, reducing the population of Tregs, and increasing inflammatory cytokine secretion. Notably, the amplified immunogenic cycle achieves an abscopal effect, effectively inhibiting distant untreated tumors. Our work highlights the potential of smart photothermal agents in hydrogel-based "all-in-one" immunotherapy and inspires the application of nanosheet-based programmable therapeutic hydrogel platforms in postoperative cancer treatment and personalized biomedicine.

Chapter 2: An AIEgen-based Dual Emitting Nanoprobe for Precise Intracellular pH Detection and Unveiling of Metabolic Variation in Differentiating Lymphocytes

2.1 Introduction

Stimulating the dormant immune system of a patient can impart durable benefits against cancerous cells [134, 135]. Adoptive T cell immunotherapy has emerged as a promising strategy by employing tumor-specific T cells against tumors [136]. T lymphocytes, particularly CD8+ cytotoxic T cells, play a critical role in the immune response because of their versatile plasticity [137, 138]. Adoptive T cell immunotherapy employs *ex vivo* expansion technology to confer key functions upon T cells, resulting in an enhanced immune response against the tumor for improved therapeutic outcomes [139]. Typically, naïve T cells (T_N; $CD62L^+$, $CD44^-$) can be specifically activated by antigen-presenting cells or nonspecifically activated by Dynabeads™ (presenting CD3/CD28 antibodies) with the presence of essential cytokines (*e.g.*, interleukin-2, IL-2) to differentiate into specific subsets, such as central memory (T_{CM}; $CD62L^+$, $CD44^+$) and effector T cells (T_E; $CD62L^-$, $CD44^+$) that are responsible for eradicating corresponding tumorigenic cells [140]. Specifically activated T cells exhibit the ability to recognize and bind to tumor cells through the interaction between the TCR and tumor antigens presented on the tumor cell surface [141]. Thus, determining the differentiation status of T cells (*e.g.*, differentiating versus undifferentiated) is critical to adoptive T cell immunotherapy [142, 143]. To achieve this, end-point methods such as flow cytometry and ELISA are conventionally employed to detect the expression of differentiation-relevant surface markers (*e.g.*, CD44 and CD62L) and cytokines (*e.g.*, interferon-γ, IFN-γ), respectively [144, 145]. Although these analytical methods are reliable, these techniques require expensive staining reagents or specialized instruments. Besides, they are generally difficult to real-time detect intracellular biomarkers to distinguish the differentiation status of living CD8+ T cells. In addition, a large number of T cell samples and lysis of the T cells may be required for the analysis, leading to the inevitable loss of T cell sources, which are greatly demanded in adoptive T cell immunotherapy. Thus, it is of high

importance to develop a cost-effective and noninvasive platform to probe differentiation states in activated T cells.

The transition of T cells from a quiescent state to a proliferating state requires profound changes in cellular metabolism, especially the increase in glycolysis for more energy (*e.g.*, ATP) to support cell proliferation and effector differentiation [142, 146, 147]. In particular, activated CD8+ T cells exhibit a more robust glycolytic process than naïve T cells by producing more metabolites, including LA [148]. Thus, these byproducts can lead to low pH_i with an acidic environment in lymph nodes [149, 150]. Hence, it is highly possible that pH_i of CD8+ T cells can be associated with the progression of T cell activation, thereby providing a specific indicator to identify the differentiation status of T cells. We hypothesize that the pH_i of activated CD8+ T cells is lower than that of non-activated CD8+ T cells. Therefore, a sensitive pH_i sensor can be an alternative approach to non-invasively probe differentiation states of T cells in real-time via metabolic insights that remain unexplored.

Endogenous and exogenous nuclear magnetic resonance (MR)-active substances have been utilized *in vivo* MR spectroscopy and MR imaging (MRI) to monitor changes in tissue pH [151]. However, MRI is limited in time resolution due to the long imaging time and cannot measure pH at the cellular level. Fluorescence imaging based on pH-sensitive fluorescent probes provides excellent opportunities to facilitate pH determination in cells and tissues due to the advantages of non-invasiveness, high spatiotemporal resolution, strong selectivity, and high sensitivity of fluorescence techniques [152-154]. Current fluorescence sensors often adopt the strategy of ratiometric output, where fluorescent signals at two or more wavelengths of excitation or emission spectrum are measured to detect changes to the local environment, such as ion concentration, pH, viscosity, and polarity [155-157]. Double emitting channel fluorophores containing a reference signal exhibit a more accurate and reliable detection than that achieved by the traditional single-output fluorescent channel [158]. In particular, dual channel enhancement fluorescence probes exhibit simultaneous fluorescence enhancement at both emission channels, providing dual authentication upon analyte stimulation [159].

Despite the wide variety of pH-sensitive fluorescent dyes available, they show several barriers to measuring pH_i, such as poor water solubility, high biotoxicity, and photobleaching [160, 161]. Besides, conventional fluorophores suffer from the ACQ effect at high concentrations, weakening their detection performance [162]. To address these issues, AIEgen has emerged as they exhibit strong emissions in solid-state and aqueous environments, which enhance their competitiveness for biomonitoring [163, 164]. The restriction of intramolecular motion (RIM) mechanism plays a crucial role in the design of AIEgen, encompassing two distinct processes: the restriction of intramolecular rotation (RIR) and the restriction of intramolecular vibration (RIV) [165, 166]. This phenomenon significantly weakens vibronic coupling, greatly reduces the probability of nonradiative transitions, and ultimately enhances fluorescence emission [167, 168]. Besides, AIEgen displays a large Stokes shift and AIE feature, overcoming the limitations imposed by ACQ encountered by most conventional dyes [169-172]. Thus far, it is of great interest to develop an AIE-based pH_i nanoprobe that can sensitively respond to the physiological range of T cells.

Herein, we report a dual-channel AIEgen-based polymeric nanoprobe for sensitive detection of pH_i for dynamic probing the differentiation progress of living activated T cells (**Figure 2.1**). This pH_i-sensitive nanoprobe consists of a pair of AIEgen as the core for pH_i detection and anti-CD8 aptamer (AptCD8)-modified pluronic F127 polymer shell (COOH-F127-COOH) to facilitate cellular uptake for intracellular delivery of the nanoprobes, with the name of AIEgen@F127-AptCD8. In this study, TPE-AMC is used (full chemical name available in **Figure 2.2**) as the pH-sensitive AIE dye and the donor. It possesses a Schiff base structure that is easily protonated in an acidic environment. This protonation enhances intramolecular electron transport to promote the fluorescent emission from weak to strong in the aggregated state. Another AIEgen is used as the other emissive channel in the core, TPE-TCF (full chemical name available in **Figure 2.2**), that is, pH-insensitive and its excitation spectrum (λ_{ex}) overlaps with the emission spectrum (λ_{em}) of TPE-AMC to form a donor-acceptor (D/A) pair (**Figure 2.1**). Furthermore, we chose the amphiphilic triblock copolymer F127 self-assembled micelle as the AIEgen protective shell because of its good endosomal escape property to facilitate

cytosolic pH_i detection (**Figure 2.1B**) [173]. We postulate that the fluorescent intensities of both channels increase with decreased pH due to the AIE effect by the disrupted micelle post-uptake in cells and the low pH-induced strong emissive TPE-AMC that provides more energy to further lighten up TPE-TCF (**Figure 2.1C, D**). The analysis of dual channels underpins the sensitivity toward the small change of pH_i [149]. The outermost AptCD8 layer offers the specificity to target CD8+ T cells and improve the colloidal stability of AIEgen@F127-AptCD8 in complex physiological conditions [174]. In our findings, we confirm that our nanoprobe is highly responsive to a large pH change, ranging from 3.0 to 10.0. In particular, AIEgen@F127-AptCD8 exhibits a linear relationship between the readout and the pH from 6.0 to 7.4, providing a reference for determining extracellular or intracellular pH with high signal stability [175]. Importantly, our nanoplatform successfully probes the distinguished pattern of pH_i in naïve and differentiated CD8+ T cells. Critically, our results reveal that activated lymphocytes show lower pH_i than the non-activated ones and this decreased pH_i is highly associated with the promoted glycolytic process in differentiating cells. Using these nanoprobes, we demonstrate the specific and dynamic detection of pH_i in lymphocytes undergoing activation/differentiation.

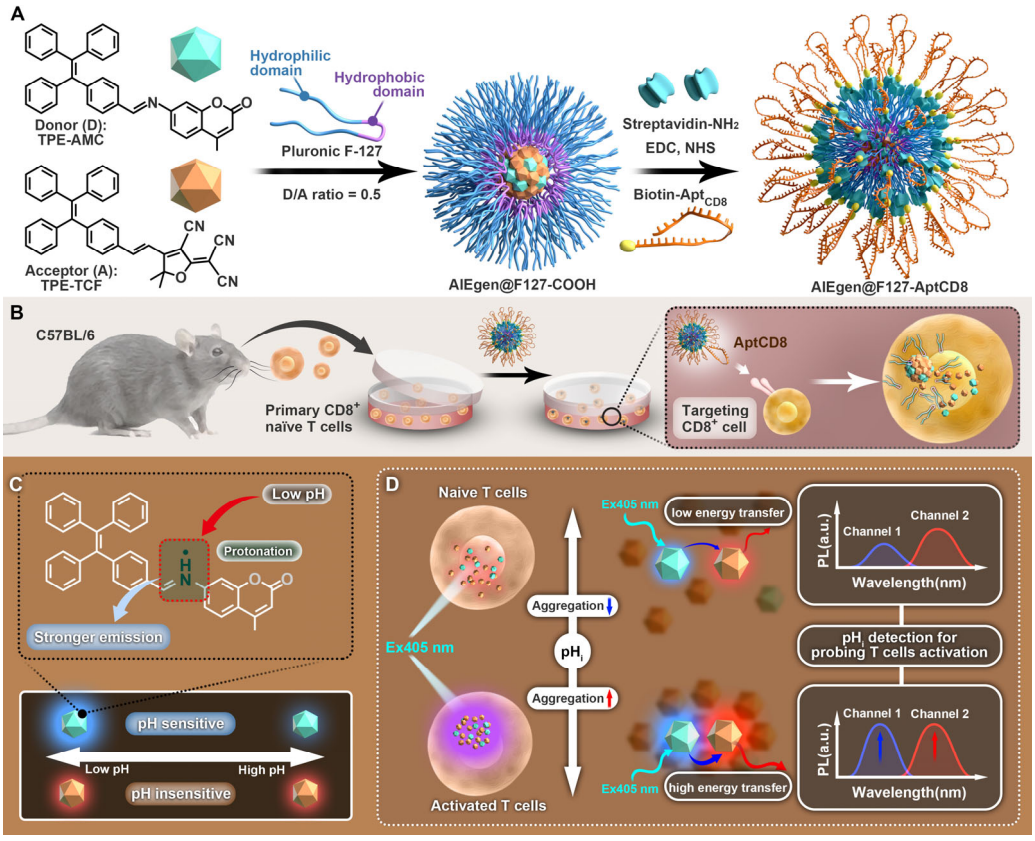

Figure 2.1 Schematic illustration of the CD8+ T cell-selective nanoprobe (AIEgen@F127-AptCD8) for dynamic sensing pH_i to fluorescently distinguish activated CD8+ T cells from naïve CD8+ T cells. (A) Synthetic route of AIEgen@F127-AptCD8 nanoprobe. (B) The extraction of primary CD8+ naïve T cell extraction from C57BL/6 mouse for incubating with AIEgen@F127-AptCD8 to study pH_i change before and after activation. (C) Schematic demonstration of the pH_i sensing mechanism of the AIEgen nanocore. TPE-AMC at various pH conditions and TPE-AMC becomes strongly emissive at low pH due to the -C=N bond protonation. Another AIEgen nanocore, TPE-TCF (acceptor), is a pH-insensitive reference probe and the Förster resonance energy transfer (FRET) acceptor of TPE-AMF (donor). (D) Proposed working mechanism of AIEgen@F127-AptCD8 for pH_i sensing. Activated T cells become more acidic than naïve T cells. The uptake TPE-AMC of AIEgen@F127-AptCD8 in the activated cells exhibits strong emission, leading to a high energy transfer to TPE-TCF that causes a dual fluorescence enhancement of double channels.

2.2 Methodology

2.2.1 Nanoprobe Fabrication

TPE-AMC was synthesized via Schiff base reactions. The synthetic route of TPE-AMC is provided in **Figure 2.2**. A mixture of compound 1 (360 mg, 1 mmol) and compound 2 (350 mg, 2 mmol) was mixed in 30 mL of dry ethanol and refluxed overnight. After cooling to room temperature, the resulting precipitates were collected and purified by silica gel column chromatography using the mixture regents of hexane and ethyl acetate (5:1, v/v) as a yellow solid in 26% yield. The final product was analyzed by ^{1}H and ^{13}C nuclear magnetic resonance (NMR). ^{1}H-NMR (400 MHz, Dmso-*d6*): δ (ppm): 8.574 (s,1H), 7.802-7.783 (dd, *J* = 7.6,1H), 7.738-7.722 (dd, *J* = 6.4,2H), 7.247.012(m, 19H), 6.353(s,1H), 2.443 (s,3H). ^{13}C-NMR (400 MHz, Dmso-*d6*): δ (ppm): 193.07, 163.07, 161.27, 160.50, 156.00, 155.37, 154.40, 153.69, 150.20, 147.76, 143.43, 143.24, 143.00, 142.83, 142.30, 140.44, 140.14, 134.68, 134.19, 131.94, 131.25, 129.60, 129.17, 128.55, 128.52, 128.41, 127.45, 127.42, 126.76, 118.65, 117.92, 113.73, 111.70, 109.37, 108.55, 108.00, 99.04. HRMS (electrospray ionization, ESI) of $C_{37}H_{27}NO_2$ *m/z*: $(M+H)^+$ calculated for 518.2115, found in 518.2119.

TPE-TCF was synthesized via condensation reactions. The synthesis protocols of TPE-TCF are provided in **Figure 2.2**. A mixture of compound 1 (720 mg, 2 mmol), compound 3 (498 mg, 2.5 mmol), and NaOH (42 mg, 1.05 mmol) was mixed in 50 mL of ethanol. The mixture was refluxed and stirred overnight under nitrogen. The resulting precipitates were collected after washing them with cold ethanol three times. The final product was then recrystallized in ethanol. The product was obtained as a red crystal with a 40% yield. The final product was analyzed by ^{1}H-NMR and ^{13}C-NMR. ^{1}H-NMR (400 MHz, Dmso-*d6*): δ (ppm): 7.841-7.800 (dd, *J* = 16.4, 1H), 7.695-7.674 (dd, *J* = 8.4, 2H), 7.182-6.973(m, 18H), 1.760 (s, 6H). ^{13}C-NMR (400 MHz, Dmso-*d6*): δ(ppm):177.65, 175.67, 148.10, 147.33, 143.37, 143.35, 143.12, 142.69, 140.32, 133.08, 132.14, 131.30, 131.26, 131.18, 129.57, 128.59, 128.55, 128.41, 127.60, 127,43, 127.40, 115.72, 113.23, 112.40, 111.40, 99.92,99.71, 54.88, 40.66, 40.56, 40.49, 40.40, 40.32, 40.23, 39.98, 39.89, 39.72, 39.55, 25.60. HRMS (ESI) of $C_{38}H_{27}N_3O$ *m/z*: $(M+Na)^+$ calculated for 564.2046, found in 564.2047.

The synthetic route and structural characterization results (NMR and ESI-MS) of COOH-F127-COOH are shown in Figure 2.2. Maleic anhydride (441 mg, 300 mmol) and F127 (6.0 g, 30 mmol) were added to a mixed solvent comprising 10 mL of toluene and 140 μL of triethylamine (TEA). The mixture was stirred under nitrogen for 1 h. Subsequently, a solution of succinic anhydride (100 mg in 4 mL toluene) was slowly added dropwise to the mixture, which was then stirred for 8 h under nitrogen protection. The resulting raw product was filtered and precipitated by adding cold ether. The precipitates were dried under the vacuum overnight, yielding a white powder. This white powder was dissolved in DI and placed in a dialysis bag (MWCO, 10 kDa) in phosphate-buffered saline (PBS) for 48 h to remove any remaining unreacted raw materials.

The subsequent preparation of AIEgen@F127-COOH involved the addition of TPE-AMC and TPE-TCF to COOH-F127-COOH through solvent evaporation-induced self-assembly. Briefly, a certain weight of TPE-AMC and TPE-TCF were separately dissolved in THF solution to achieve a concentration of 3 μM. The F127-COOH (100 mg) was dissolved in 10 mL of DI water. The stock solution of TPE-AMC (50 μL) and TPE-TCF (100 μL) slowly dropped into

the solution of COOH-F127-COOH (1 mL), respectively. The mixture was then stirred in the dark for 24 h to allow the THF solution to evaporate. After THF was evaporated, the solution was collected by centrifugation and washed three times with PBS buffer. The final concentration of the AIEgen@F127-COOH was adjusted to 1 mg mL^{-1}, and the samples were stored at 4 ˚C until further use.

Subsequently, the anti-CD8 aptamer was conjugated to the surface of the AIEgen@F127-COOH using the EDC/NHS coupling method. First, streptavidin-coated nanoparticles, AIEgen@F127-SA were prepared. N-hydroxysuccinimide (NHS, 92 mg, 100 mmol) and 1-ethyl-3-(3-dimethylaminopropyl) carbodiimide (EDC, 25 mg, 20 mmol) were separately dissolved in 2-(N-morpholino) ethanesulfonic acid) (MES, 0.1 M, pH 5.6) and PBS buffer (pH 7.4). The EDC solution was added to the AIEgen@F127-COOH (1 mg mL^{-1}, 2 mL) solution for 15 min, and then NHS solution was added to the mixture to activate the carboxyl group of COOH-F127-COOH. After 1 h of reaction, 2 mg mL^{-1} streptavidin solution (dissolved in PBS buffer) was added to the mixture and stirred overnight. This allowed the binding of streptavidin onto the surface of AIEgen@F127-COOH. To remove any excess streptavidin, the mixtures of AIEgen@F127-SA were centrifuged (14000 rpm, 20 min) multiple times and then resuspended in PBS.

The bioconjugate AIEgen@F127-AptCD8 was synthesized using the following procedure: the pH of the AIEgen@F127-SA (1 mg mL^{-1}, 1 mL) solution was adjusted from 7.4 to 8.0 with Na_2CO_3. Next, then biotin-ssDNA CD8 aptamer (10 μM) was added to the suspension of AIEgen@F127-SA, and the reaction mixture was shaken at 37 °C for 1 h. To remove free unreacted biotin-ss DNA, the final product was placed in a dialysis bag (MWCO, 5 kDa) against DI water. The solution inside the dialysis bag was subsequently lyophilized for further experiments. The SEM and TEM images of AIEgen@F127-COOH and AIEgen@F127-AptCD8 were performed on Tescan MIRA and JEOL Model JEM-2010, respectively.

2.2.2 Nanoprobe Characterization

UV-Vis absorption and PL spectrum. The absorbance and PL spectrum of TPE-AMC (10

μM), TPE-TCF (10 μM), AIEgen@F127-COOH (100 μg mL^{-1}), AIEgen@F127-SA (100 μg mL^{-1}) and AIEgen@F127-AptCD8 (100 μg mL^{-1}) were measured. The wavelength range from 200 to 600 nm of absorbance spectrums was measured by UV-vis-NIR spectrophotometer (Ultrospec 2100). The PL spectrums were measured by a fluorescent spectrometer (Perkin Elmer LS55) using the best absorbance wavelength.

pH-Dependence Fluorescence Studies of AIEgen@F127-COOH. The different pH buffers were prepared using Na_2HPO_4, citric acid (CA), $NaCO_3$, and $NaHCO_3$ (adjusted pH value from 9.0 to 4.0 by different ratios of the above compounds) and measured using a pH meter. AIEgen@F127-COOH was added to each pH buffer with different pH values, maintaining a concentration of 100 μg mL^{-1}. The mixture solution was then shaken to ensure good dispersion of AIEgen@F127-COOH. The PL spectrum (λ_{ex} = 400 nm) were recorded after 1 h of equilibration time.

2.2.3 Mouse CD8+ T Cell Purification and *In Vitro* Culture

CD8+ naïve T cells were isolated from the spleen of C57BL/6 mice. The spleen was mechanically disrupted using the rear end of a 1 mL syringe plunger and filtered through a 70 μm cell strainer to obtain the lymphocyte population. The isolated lymphocytes were then suspended in 5 mL of RPMI 1640 medium and incubated with 1X red blood cell lysis buffer for 10 min to remove red blood cells. Lymphocytes were collected after centrifugation at 1000 rpm for 10 min. Magnetic cell sorting was employed to isolate CD8+ naïve T cells. A negative fraction of primary T cells was collected using the CD8+ naïve T cell isolation kit (Bio Legend) and according to the protocol provided by the manufacturer. Cells were labeled with nanobeads that remained in the centrifuge tube due to magnet attraction. Cells unlabeled with nanobeads were harvested and subjected to further experiments. The isolated CD8+ naïve T cell was cultured in RPMI 1640 medium containing 10% FBS and 1% P/S. For the activation of CD8+ T cells, the culture medium was further supplemented with 2 mM L-Glutamine, 50 μM 2-mercaptoethanol, and 100 U mL^{-1} recombinant mouse IL-2.

2.2.4 Cytotoxicity Study

The cytotoxicity of AIEgen@F127-COOH and AIEgen@F127-AptCD8 separately against Jurkat cells and CD8+ T cells was evaluated by WST-8 assay, respectively. 4×10^4 Jurkat cells or CD8+ T cells per mL were seeded at 96-well plates and incubated for 24 h. Then, the AIEgen@F127-COOH or AIEgen@F127-AptCD8 was added into the cell culture medium at a final concentration ranging from 0 to 250 μg mL^{-1} and these cells were incubated in the 96-well plates for 20 h at 37 °C. After the specified time interval, the cells were centrifuged and resuspended in the fresh medium, and then incubated in 100 μL fresh medium and 20 μL WST-8 solution (5 mg mL^{-1}) for another 4 h. The experimental setup included a blank group containing only medium, a control group consisting of untreated cells with WST-8 solution, and test groups with cells, NPs, and WST-8 solution. Cell viability was quantified by measuring the absorbance at 450 nm in each well.

2.2.5 *Ex vivo* Activation of CD8+ T cells.

1×10^6 cells per mL naïve CD8+ T cells were initiated in 24-well plates. The addition of Dynabead™ follows the ratio of 3:1 (Dynabead™: T cell). The concentration of cells was adjusted to 5×10^5 cells per ml in 6-well plates and used Cell Counting Kit-8 (CCK-8, Dojindo) assay for cell counting two days later. The activation of CD8+ T cells was performed by following the same method and mouse CD3/CD28 Dynabead™ was used for initiating the activation process of these cells. Then, 100 U mL^{-1} recombinant mouse IL-2 was added to the cell culture medium to further stimulate cell differentiation. To prevent the beads from detaching from the cells, the medium was supplemented with appropriate CD3/CD28 Dynabead™ on Day 5 and 7.

2.2.6 Biomarker Expression Evaluation

The biomarker expression of T_N, T_E, and T_{CM} was evaluated using the following fluorochrome-conjugated anti-mouse monoclonal antibodies (mAbs): APC anti-CD8a, FITC anti-CD62L and PerCP-Cy5.5 anti-CD44 (BD Biosciences). Before incubating the above

antibodies, the cell suspension was preincubated with anti-mouse CD16/CD32 mAb (BD Biosciences) at 4°C for 10 min to perform Fc Block. All staining steps were performed in a buffer of PBS containing 0.5% BSA. Flow cytometry analysis was acquired on BD Accuri C6 Flow Cytometer, and data analyses were conducted using FlowJo software.

Nonactivated T cells and activated T cells of Day 1, 3, 5, and 7 were collected to measure the concentration of LA, ATP, and IFN-γ. LA levels were quantified using an LA content assay kit (Solarbio) on the microplate reader (Varioskan LUX Multimode Microplate Reader). The total LA content of specimens was extracted and evaluated following the protocol which is offered by Solarbio. ATP concentrations were determined using an ATP assay kit (Beyotime) measured on the same microplate reader. For IFN-γ analysis, the supernatant of the cell medium was collected for subsequent ELISA, with absorbance measured using a microplate reader (Labexim Products LEDETECT 96 Microplate Reader).

2.2.7 Endocytosis Pathway-Specific Blocking of Nanoprobe

A total of 1×10^6 cells were seeded in a well plate and incubated for 24 h. After this period, the cells were rinsed twice with PBS and then exposed to 100 μM nystatin and 20 μM chlorpromazine in a complete medium for 6 h. The cells without any intervention served as the controls. After the pretreatment phase, the inhibitors were removed, and the cells were washed twice with PBS. Subsequently, the cells were incubated with 100 μg mL^{-1} of AIEgen@F127-AptCD8 at 37 °C and 5% CO_2 for 1 h.

2.2.8 Cell Imaging and pH_i Response *In Vitro*

The CD8+ T cells were washed with PBS and incubated in a high K+ buffer (30 mM NaCl, 120 mM KCl, 1mM $CaCl_2$, 0.5 mM $MgSO_4$, 1 mM NaH_2PO_4, 5 mM glucose, 20 mM HEPES, 20 mM NaOAc) with various pH values from 6.6 to 7.4. 10 μM nigericin solution was added to calibrate intracellular pH and then treated with nigericin for another 10 min, which could quickly equilibrate intracellular and extracellular pH. Then the 100 μg mL^{-1} AIEgen@F127-AptCD8 was added to the cell medium and incubated for 1 h in the 37 °C incubator.

Nonactivated T cells and activated T cells of Day 1, 3, 5, and 7 were collected to incubate with AIEgen@F127-AptCD8 and probing the T cell status by cell imaging. The selectivity assay of AIEgen@F127-AptCD8 was evaluated against macrophages (RAW 267.4) and MCF-7 cells. To investigate the impact of glycolysis inhibition on pHi fluctuations, both naive and activated CD8 T cells were treated with the glycolysis inhibitor 2-DG. All images were acquired using a Leica TCS SPE confocal spectruml microscope imaging system. An argon laser was excited at 405 nm and the emission data were collected at 410-480 nm and 600-750 nm respectively. For suborganelle dye co-localization staining, Mito-Tracker Green (100 nM), ER-Tracker Green (100 nM), or Lyso-Tracker Green (100 nM) were incubated with activated CD8+ T cells that had been previously incubated with AIEgen@F127-AptCD8 for 1 h. The incubation with the suborganelle dyes was carried out for 30 min. Then cells were imaged using Leica SP8 laser confocal microscopy to visualize the co-localization patterns.

2.2.9 Statistical Analyses

One-way ANOVA with Dunnett's or Tukey's multiple comparison tests was performed to analyze the results using GraphPad Prism software (GraphPad, USA). Results were presented as mean ± SD. Statistical significance was determined at *p< 0.05, **p< 0.01, ***p< 0.001. In addition, the P-value and detailed information for each experiment were provided in each legend.

2.3 Results and Discussion

2.3.1 Design and Characterization of pH_i Nanoprobe

In this study, we synthesized the TPE-AMC (D) and TPE-TCF (A) via coupling the aldehyde group of TPE-CHO to amino-activated or methyl-activated molecules by Schiff base and condensation reactions, respectively (**Figure 2.2A**), according to previous reports [154, 176, 177]. Besides, we modified the surfactant F127 to possess COOH terminal groups (COOH-F127-COOH) to enable subsequent AptCD8 labeling without interfering with its amphiphilic nature (**Figure 2.2A**), by carboxylation reaction [178, 179]. ^{1}H and ^{13}C NMR and ESI mass spectrometry

confirmed the synthesis of TPE-AMC and TPE-TCF. Similarly, ^{1}H-NMR and Fourier-transform infrared spectrum (FTIR) validated the modification of the F127 (**Figure 2.2B, C**). Upon functionalization, a discernible resonance peak appears at δ = 6.6 ppm, ascribed to the presence of maleic anhydride (-CH = CH-) moiety of COOH-F127-COOH, while the signal of -CH_2-OH moiety at δ = 2.6 ppm was absent. Likewise, FTIR spectrum showed that the characteristic peak of the modified F127 at 1785 cm^{-1} was ascribed to the -COOH group, indicating the conversion of the -OH group into -COOH groups in F127 copolymer chain segments. We verified that the emission spectrum of TPE-AMC (blue-color emission) and TPE-TCF (red-color emission) gradually blue shifted and their peak intensities elevated with increased water content in DI water/THF nonsolvent/solvent mixtures (**Figure 2.2D-G**), supporting their AIE characteristics [180, 181]. COOH-F127-COOH is a triblock amphiphilic polymer with one hydrophobic domain and two hydrophilic segments [182]. It is highly biocompatible, and its hydrophobic core is often employed to encapsulate hydrophobic pharmaceuticals. Therefore, COOH-F127-COOH can self-assemble as NPs via encapsulating the hydrophobic molecules such as TPE-AMC and TPE-TCF as the nanocore in an aqueous solution to form AIEgen@F127-COOH. Single encapsulation of TPE-AMC (TPE-AMC@F127-COOH) or TPE-TCF (TPE-TCF@F127-COOH) resulted in emission maxima at 435 and 655 nm, respectively, while AIEgen@F127-COOH showed slightly red-shifted emission peaks at 450 and 660 nm (**Figure 2.2H**). These two peak intensities became half and five times the original ones capped in NPs, respectively, confirming the energy transfer at proximity for a dual emitting response. We further optimized the FRET efficiency by FRET-based binding assay of different D/A ratios for obtaining the best pH_i biosensing performance of AIEgen@F127-COOH. Based on the result, we chose the D/A ratio of 0.5 for the following experiments as the intensity of the acceptor almost reached the maximum (**Figure 2.2I**).

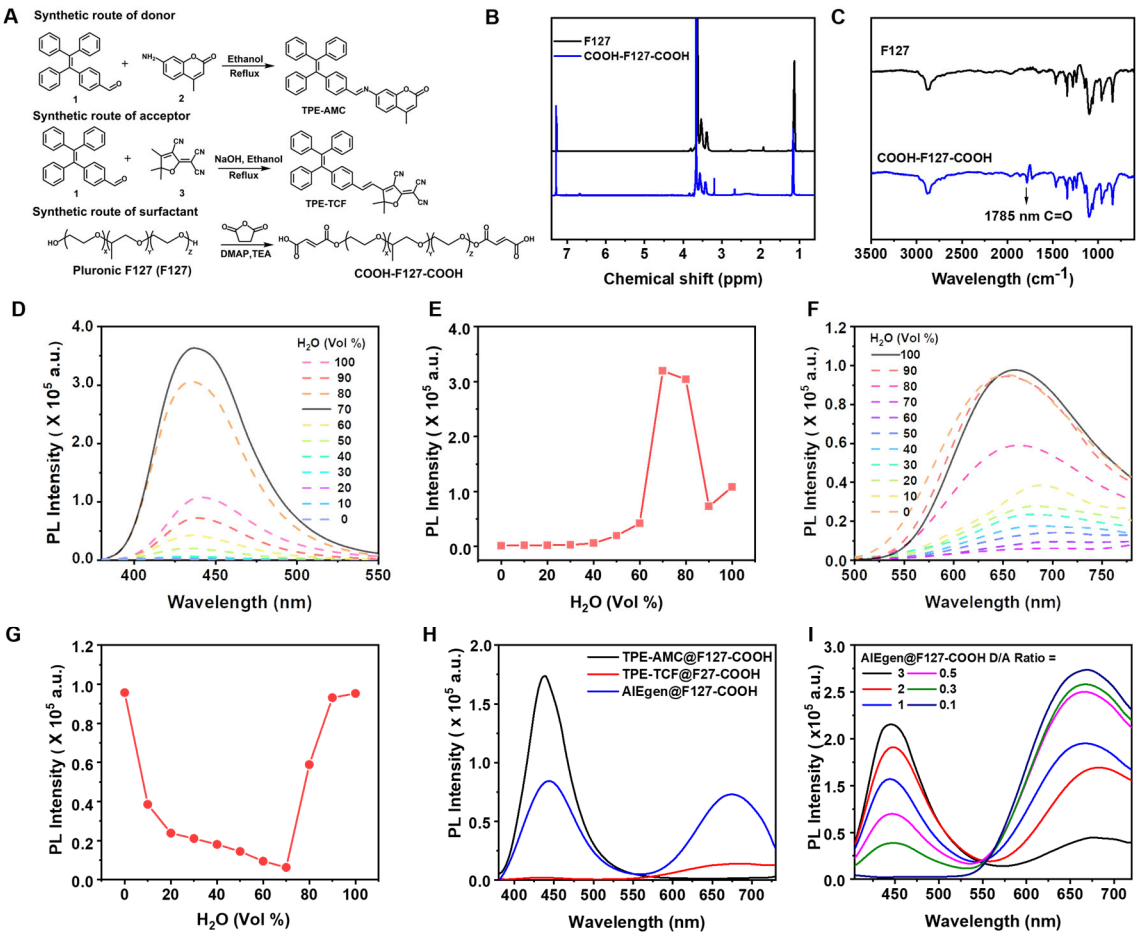

Figure 2.2 Molecule characterization and AIE performance. (A) Synthetic route of TPE-AMC ((E)-4-methyl-7-((4-(1,2,2-triphenylvinyl) benzylidene) amino)-2H-chromen-2-one, Donor), TPE-TCF ((E)-2-(3-cyano-5,5-dimethyl-4-(4-(1,2,2-triphenylvinyl) styryl) furan-2(5H)-ylidene) malononitrile, Acceptor), and COOH-F127-COOH, respectively. (B) ^{1}H-NMR spectrum of F127 and COOH-F127-COOH in $CDCl_3$. (C) FTIR spectrum of F127 and COOH-F127-COOH. (D) Photoluminescence (PL) spectrum of TPE-AMC (10 μM) in THF/DI water solution (pH = 7.4) mixtures with different volume fractions of DI water (f_W). λ_{ex} = 360 nm. (E) Plot emission intensity at 435 nm versus water fraction. (F) PL spectrum of TPE-TCF (10 μM) in THF/DI water solution (pH = 7.4) mixtures with different volume fractions of DI water. λ_{ex} = 450 nm. (G) Plot emission intensity at 655 nm versus water fraction. When f_W is no more than 70 %, the emission of the TPE-TCF in THF/DI water mixtures dramatically weakens and bathochromically shifts to 680 nm. A significant increase in the fluorescence intensities is observed upon the gradual enhancement of f_W from 70 to 100%. The decreases in the fluorescence intensity for both TPE-AMC and TPE-TCF in water content >70% were probably ascribed to the twisted intramolecular charge-transfer (TICT) process, which prescribed the

low emission efficiency of a fluorogenic with a D-A structure in a highly polar solvent [183]. The redshift of the emission spectrum is ascribed to the solvatochromic effect [184]. (H) PL spectrum of TPE-AMC@F127-COOH, TPE-TCF@F127-COOH, and AIEgen@F127-COOH (100 μg mL^{-1}, D/A ratio = 1) in DI water. λ_{ex} = 360 nm. (I) The FRET-based binding assay by PL spectrum of AIEgen@F127-COOH with the various donor: acceptor ratios. λ_{ex} = 400 nm.

Finally, AIEgen@F127-COOH conjugated with AptCD8 reacted with streptavidin through an amine-carboxylic acid conjugation to permit further labeling of biotin-linked AptCD8 to construct AIEgen@F127-AptCD8 [185]. SEM images showed a size increase from 76 ± 5 nm of AIEgen@F127-COOH to 137 ± 9 nm of AIEgen@F127-AptCD8 due to the surface modification with AptCD8 (**Figure 2.3A, B**), consistent with the dynamic light scattering (DLS) characterization for the size and zeta potential changes (**Figure 2.3C, D**). Consistently, the presence of streptavidin-biotin-linked AptCD8 layer was clearly observed on AIEgen@F127-AptCD8 with a core-shell structure in the TEM image (**Figure 2.3F**). In contrast, the TEM image of AIEgen@F127-COOH did not show a core-shell structure (**Figure 2.3E**). This result demonstrated the coating of the AptCD8 layer on the AIEgen@F127-COOH core. Meanwhile, the characteristic absorption peaks of the AIEgens remained the same after surface modification (**Figure 2.3G**). Additionally, the agarose gel electrophoresis image indicated that the conjugation of AptCD8 (single-stranded DNA) onto AIEgen@F127-COOH led to an increase in its molecular weight with less electrophoretic mobility (**Figure 2.3H**). The above results demonstrated the successful synthesis of AIEgen@F127-AptCD8.

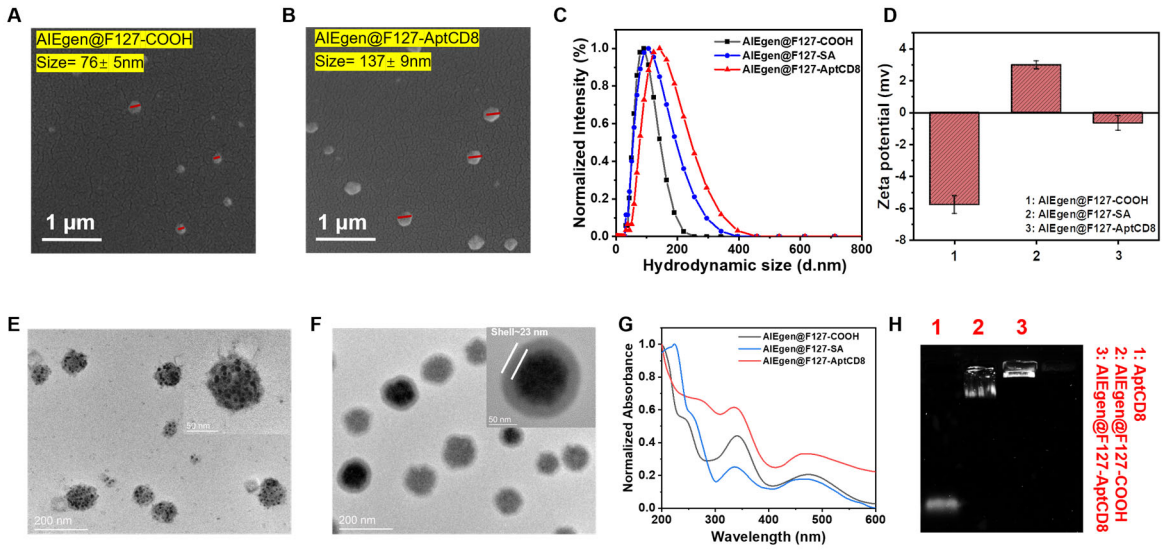

Figure 2.3 The characterization and determination of NPs. Scanning electron microscopy (SEM) images and size distribution analysis of (A) AIEgen@F127-COOH and (B) AIEgen@F127-AptCD8. (C) Dynamic Light Scattering (DLS) analysis of size change during the surface modification. (D) The table of particle sizes and zeta potentials of AIEgen@F127-COOH, AIEgen@F127-SA, and AIEgen@F127-AptCD8. Representative transmission electron microscopy (TEM) images of (E) AIEgen@F127-COOH and (F) AIEgen@F127-AptCD8. The scale bar is 200 nm. The inset image shows a higher magnification area of interest. The scale bar is 50 nm. (G) Normalized ultraviolet-visible (UV-Vis) absorption spectrum of AIEgen@F127-COOH, AIEgen@F127-SA, and AIEgen@F127-AptCD8 in PBS buffer. (H) Agarose gel electrophoresis image for DNA ladder, free CD8 ssDNA aptamer, AIEgen@F127-COOH, and AIEgen@F127-AptCD8 (from left to right).

Thus, the emission of TPE-TCF relies on the energy from TPE-AMC in this interaggregate nanocore as the second verification of the pH change with an overall large stoke shift (from $\lambda_{ex}/\lambda_{em}$ = 400/450 nm to $\lambda_{ex}/\lambda_{em}$ = 400/660 nm, **Figure 2A**). We next assessed the pH response of TPE-AMC and TPE-TCF in buffers of pH values from 10.0 to 3.0 (**Figure 2.4B, C**). We chose the excitation wavelength (λ_{ex}) of ~ 400 nm for TPE-AMC in the following study because it is more biologically friendly than its absorbance peak in 360 nm, which can cause degradation of intracellular components during repeated excitation for cell imaging [186]. Critically, the fluorescent intensity peak of TPE-AMC excited by 400 nm laser increased with decreased pH in a linear relationship, which demonstrated its broad pH sensitivity range and elevated signals

in low pH. In contrast, the TPE-TCF peak intensity excited by 450 nm laser remained similar throughout this pH range, ascertaining TPE-AMC as the only variable energy source (donor) in our system correlated with pH values (**Figure 2.4D**). To evaluate the pH responsiveness of AIEgen@F127-COOH, we narrowed down the pH range between 6.0 and 7.4, and each value varied by one decimal place to emulate the physiological condition [187-189]. Strikingly, both peak intensities of TPE-AMC and TPE-TCF were enhanced with dropped pH values (**Figure 2.4E**). The signal intensities from these two molecules increased by 57.76% and 26.98% at pH 6.0 compared to those at pH 7.4, respectively. Compared to TPE-AMC@F127-COOH, the 450 nm emission intensity (I_{450}) of AIEgen@F127-COOH (containing the donor/acceptor pair) showed ~ 5-fold reduction where the energy was transferred to TPE-TCF from TPE-AMC by FRET in pH 7.4. The I_{450}/I_{660} ratio of AIEgen@F127-COOH showed a sigmoid-like curve from pH 10.0 to 3.0 (**Figure 2.4F**). Our result showed that the detecting system exhibited upper and lower cut-off values to be pH > 4.0 or < 9.0, respectively. The pKa of the AIEgen@F127-COOH was calculated to 5.9488 ± 0.0352 (**Figure 2.4G**). Furthermore, we obtained a linear relationship ($R^2 = 0.9891$) and a positive correlation between TPE-AMC/TPE-TCF (I_{450}/I_{660}) peak value ratios and decreased pH values. This linear range is highly promising as a fluorescent indicator for sensitive pH_i sensing. We also visualized the various fluorescent colors of AIEgen@F127-COOH in an aqueous solution (**Figure 2.4H**), and the colors changed from blue, reddish-purple to red with respect to the pH from low to high value. The chromaticity diagram indicates that the tristimulus values for each specimen are well separated at different pH values (**Figure 2.4 H, I**). These findings demonstrate the exceptional pH response performance of AIEgen@F127-COOH, particularly within the pH range of 6.0-7.4.

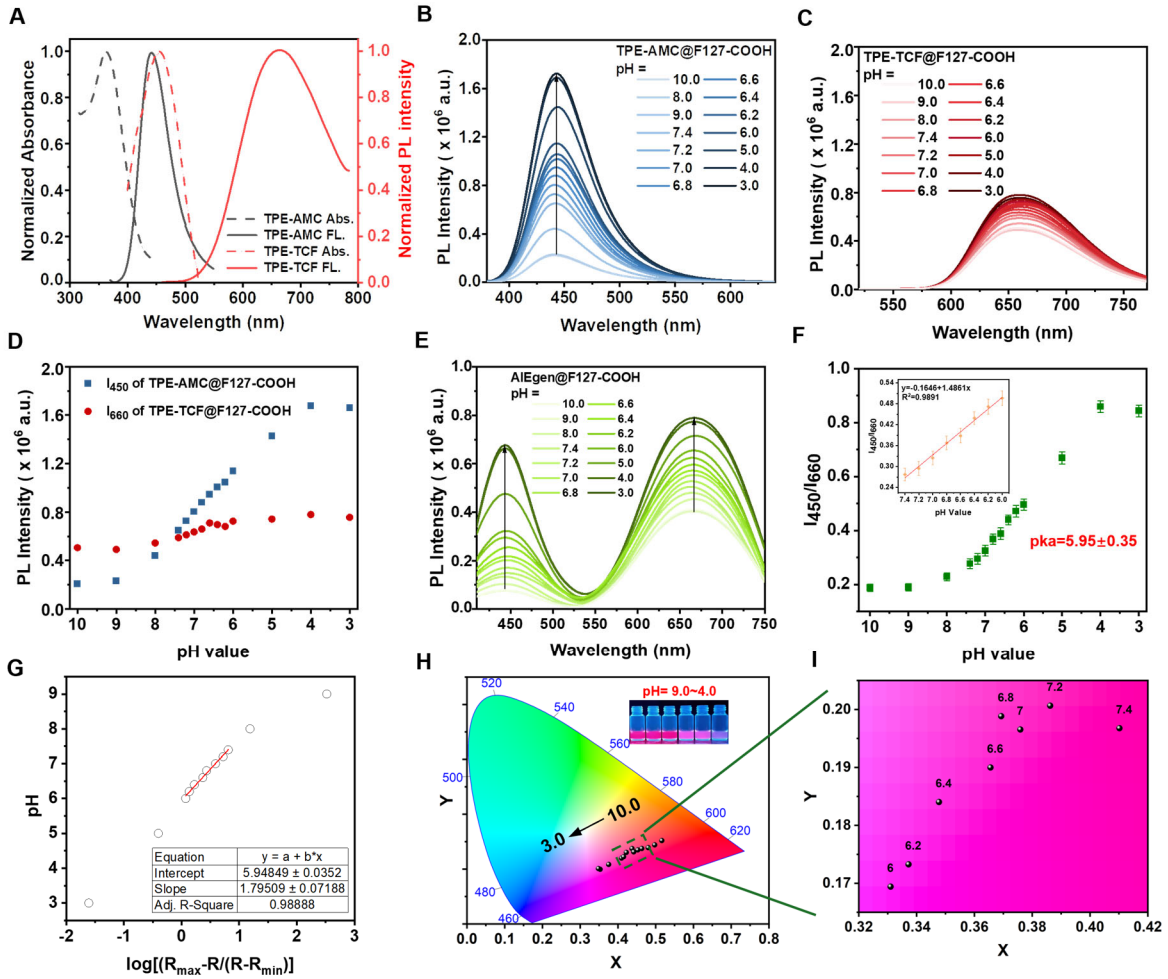

Figure 2.4 Material characterizations of AIEgen@F127-AptCD8. (A) Normalized UV-Vis absorption and PL emission spectrum of TPE-AMC (10 μM, λ_{ex} = 360 nm) and TPE-TCF (10 μM, λ_{ex} = 450 nm) in THF and DI water mixture (9/1, v/v), respectively. Emission spectrum of (B) TPE-AMC@F127-COOH and (C) TPE-TCF@F127-COOH (100 μg mL^{-1}) at different pH (pH 10.0 to 3.0) and 37 °C. (D) Graphical plot of PL intensity versus TPE-AMC (λ_{em} = 450 nm) and TPE-TCF (λ_{em} = 660 nm) at various pH values, respectively. (E) PL emission spectrum of AIEgen@F127-COOH (100 μg mL^{-1}, λ_{ex} = 400 nm) at different pH (from 10.0 to 3.0) and 37 °C. (F) The linear relationship between pH values and the ratio of emission intensity at 450 nm and 660 nm (I_{450}/I_{660}) of AIEgen@F127-COOH (R^2 = 0.9891). Inset: The calibration curve of AIEgen@F127-COOH was plotted in a small range of pH values from 7.4 to 6.0. (G) The plot of pH vs $\log[(R_{max}-R)/(R-R_{min})]$, where R is the ratio of fluorescence intensity of AIEgen@F127-COOH at 450nm and 660 nm upon excitation at 400 nm. The y-intercept is the pKa value (5.9488 ± 0.0352) of AIEgen@ F127-COOH. (H) The CIE1931 chromaticity plot for color coordinates of AIEgen@F127-COOH with pH values

ranging from 10.0 to 3.0. Inset: the photograph of AIEgen@F127-COOH with pH values ranging from 9.0 to 4.0 was taken under a handheld UV lamp at room temperature. (I) Magnified areas of the CIE 1931 diagram with pH values ranging from 7.4 to 6.0.

The optical stability of the nanoprobe is crucial for its biosensing application. We conducted continuous fluorescence intensity measurements of the TPE-AMC@F127-COOH (donor-based probe), TPE-TCF@F127-COOH (acceptor-based probe), and AIEgen@F127-COOH (I_{450}/I_{660} ratio) in the buffers at pH 7.4 and 6.0 over 120 min at 1 min intervals, respectively, (**Figure 2.5A-C**), as well as for a longer period measurement over 7 days (**Figure 2.5D**). Specifically, the fluorescent intensity of TPE-AMC@F127-COOH and I_{450}/I_{660} ratio of AIEgen@F127-COOH showed ~ 1.5 and ~ 2 times enhancement at pH 6.0 compared to pH 7.4 and this enhancement remained stable throughout the measured long period. Furthermore, the specificity of AIEgen@F127-COOH was evaluated in buffers consisting of cations (Na^+, K^+, Ca^{2+}, Mg^{2+}), redox reagents (H_2O_2 and GSH), glucose, or amino acids (Glu, Gly, Cys, Lys), respectively, for signal readout measurement in different conditions (**Figure 2.5E**). The emission spectrum of the TPE-AMC@F127-COOH, TPE-TCF@F127-COOH, and AIEgen@F127-COOH remained largely consistent when the analytes were introduced, indicating that the complex physiological conditions did not interfere with the pH-responsive behavior of nanoprobe. Besides, it should be noted that the NPs size of AIEgen@F127-COOH tended to increase at extreme pH (**Figure 2.5G-I**), probably due to the disruption of the F127 shell and assembly of AIE dyes as larger aggregates [190, 191]. Nevertheless, the absorption spectrum of the AIEgen@F127-COOH remained similar from pH 6.0 to 7.4, which minimized other physical factors to influence pH_i biosensing at the physiological range (**Figure 2.5F**). These results support our postulation of strengthened energy transferred from D to A in low pH, resulting in a dual-channel fluorescent enhancement for increased sensitivity and mutual verification of pH change. Besides, we compared the photobleaching properties of AIEgen@F127-AptCD8 and the commercial pH probe SNARF™-1 after cellular endocytosis of the probes and continuous excitation by confocal laser over 20 min (**Figure S14**). Our results showed that AIEgen@F127-AptCD8 exhibited a lower decrease of ~ 20% over 20 min in

fluorescence intensity, while a ~ 40% decrease of the original signal was observed in SNARF™-1. These findings highlight the excellent photobleaching-resistance properties of AIEgen@F127-COOH.

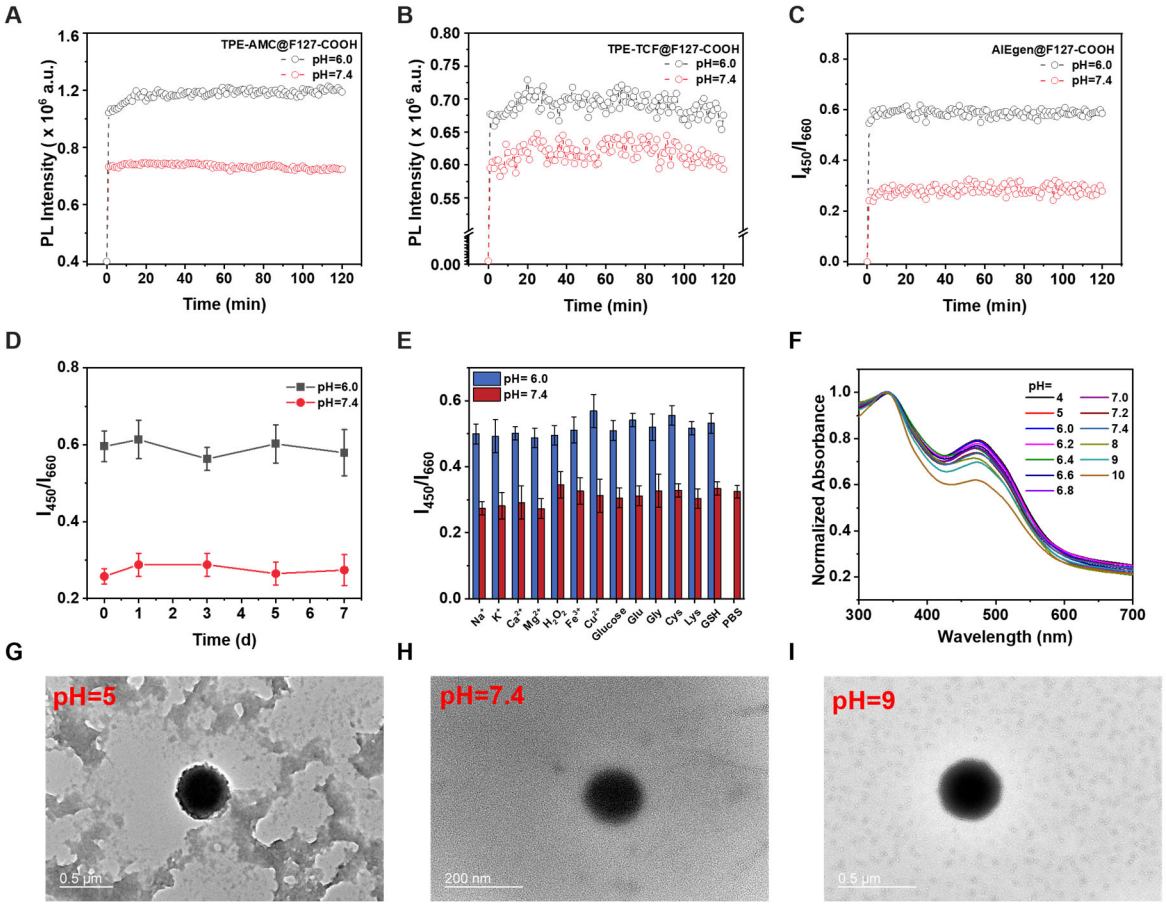

Figure 2.5 Evaluation of selectivity and stability of the donor, acceptor, and NPs. The photochemical stabilities of (A) TPE-AMC@F127-COOH and (B) TPE-TCF@F127-COOH in pH = 6.0 or pH = 7.4 buffer solution monitored at their maximum emission wavelengths at a concentration of 100 μg mL^{-1}, respectively. The laser irradiation was performed every 1 min for 120 min. The ratio of emission intensity at 450 nm and 660 nm (I_{450}/I_{660}) of AIEgen@F127-COOH in pH = 6.0 or pH = 7.4 buffer solution monitored for (C) 120 min or (D) different days at a concentration of 100 μg mL^{-1}, respectively. (E) The selectivity of AIEgen@F127-COOH various metal ions, amino acids, and ROS at pH = 6.0 or pH = 7.4 buffer solution. (F) The absorption spectrum of AIEgen@F127-COOH in different pH buffers. TEM image of AIEgen@F127-COOH at (G) pH 5 (H) pH 7.4 and (I) pH 9.

2.3.2 Calibration of pH_i Nanoprobe for *In Vitro* Study

In this study, we selected mouse primary CD8+ T cells as the T lymphocyte models for assessing the fluctuation of pH_i before and after *ex vivo* activation [192, 193]. To quantify the pH_i of CD8+ T cells corresponding to their states, we loaded the AIEgen@F127-AptCD8 nanoprobe into the cell before the activation by human or mouse T-activator CD3/CD28 Dynabeads™ (**Figure 2.6A**). We first utilized AIEgen@F127-AptCD8 to probe the pH_i of CD8+ T cells, respectively. We then evaluated the cytotoxicity of our nanoprobe. The results showed that the cell viability of both groups was above 80% when the concentrations of the NPs were ≥ 100 μg mL^{-1} (**Figure 2.6B**), which was chosen for the following cell imaging experiments. We calibrated the standard signal of our nanosystem in response to the pH_i of T lymphocytes through varying pH (from 6.0 to 7.4) of the culture medium, according to the previous report [194]. Noticeably, our nanoprobe was able to visualize the pH_i by fluorescent signals within 1 h upon NPs incubation, indicating the rapid entry of NPs into cells. Consistently, our confocal imaging results depicted pH-dependent incremental signals of the dual channels (**Figure 2.6C-E**). On the other hand, the signal obtained by direct excitation of TPE-TCF@F127-AptCD8 showed minimal change in this pH_i range. We quantified the mean fluorescent of the intracellular signals presented by TPE-TCF@F127-AptCD8, TPE-AMC@F127-AptCD8 and AIEgen@F127-AptCD8, respectively to compare the signal differences between single-channel and dual-channel probes produced by FRET effect. TPE-AMC@F127-AptCD8 excited by 405 nm demonstrated a trend of increased intracellular fluorescent signals (**Figure 2.6C, left in single nanoprobe**), consistent with its pH-sensitive behavior within this pH range. Similarly, TPE-TCF in AIEgen@F127-AptCD8 showed pH-sensitive intracellular fluorescent signals due to the high energy transfer in the FRET effect between TPE-AMC (donor) and TPE-TCF (acceptor) of AIEgen@F127-AptCD8 together with the pH sensitivity of TPE-AMC. In contrast, the intracellular fluorescent intensity of TPE-TCF@F127-AptCD8 directly excited by its peak absorption at 488 nm exhibited an insignificant change from pH 7.4 to 6.0 (**Figure 2.6C, right in single nanoprobe**), consistent with its pH-insensitive behavior within this pH range. The ratio intensity of TPE-AMC/TPE-

TCF channels ($I_{TPE\text{-}AMC}/I_{TPE\text{-}TCF}$) maintains a linear relationship ($R^2 = 0.9888$) against the pH_i of T cells (**Figure 2.6F**). We further used flow cytometry to analyse a large population size and observed a higher proportion in gate Q2 at low pH, further confirming the trend of fluorescent imaging results ($R^2 = 0.9503$) produced by our probe along with various pH_i (**Figure 2.6G-I**). Our findings demonstrated that the nanoprobes were efficiently uptaken by cells and the I_{450}/I_{660} channel ratio as well as the signal intensities remained stable over 10 days, suggesting that our nanoprobe can potentially provide long-term tracking of pH_i. Hence, we conclude that our pH_i detection nanosystem demonstrates a high sensitivity and stability toward pH_i detection and is ready to probe pH_i in T lymphocytes.

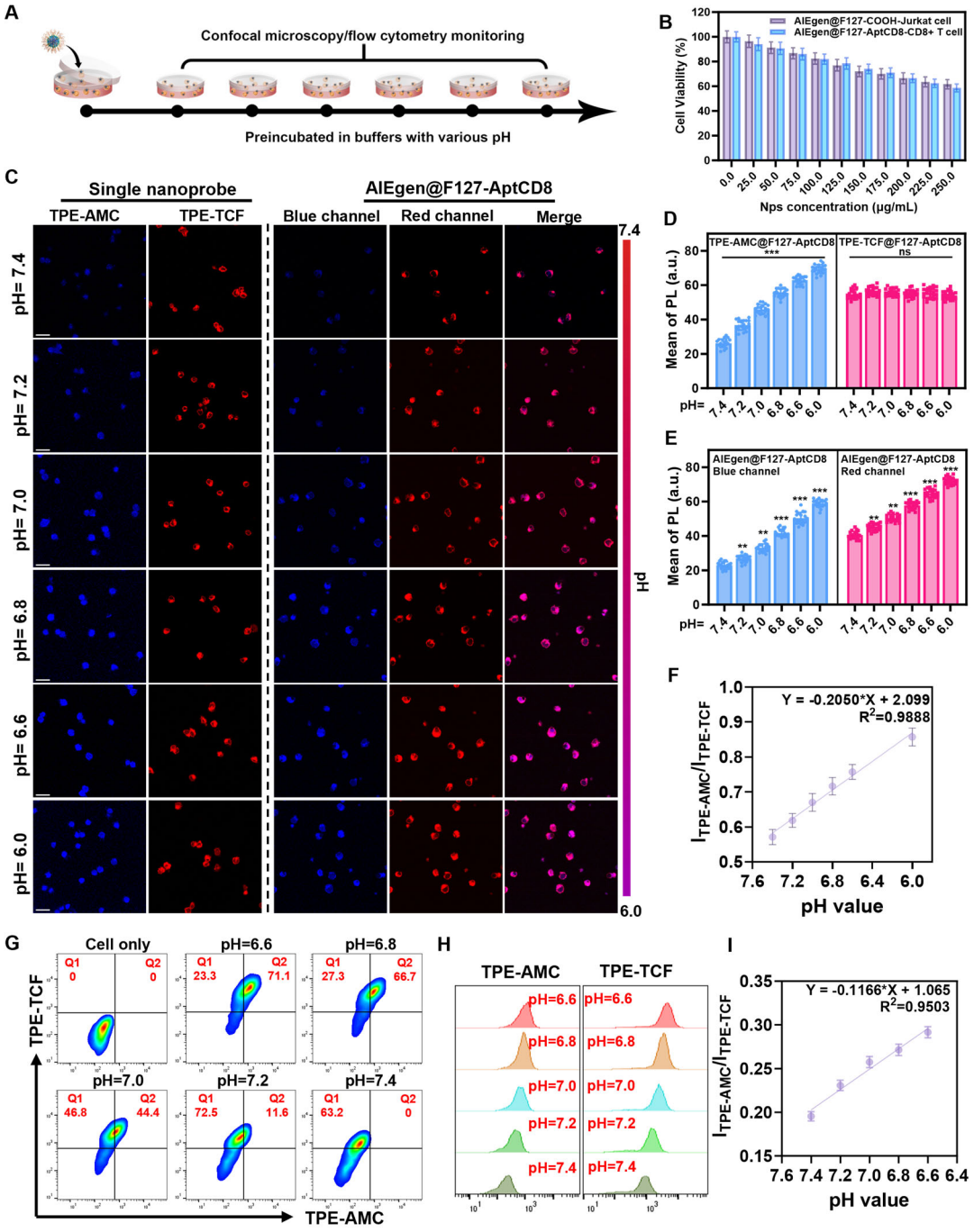

Figure 2.6 Calibration of in pH_i biosensing by AIEgen@F127-AptCD8. (A) Schematic illustration of the *in vitro* experimental design. 10 μM nigericin was used to homogenize the extracellular and intracellular pH. (B) Cell viability assessed by WTS-8 assay after 24 h exposure to increasing AIEgen@F127-COOH and AIEgen@F127-AptCD8 concentrations: 0 (control), 25, 50,75, 100, 125, 150, 175, 200, 225, and 250 μg mL^{-1} in Jurkat cells and CD8+ T cells, respectively. (C) Confocal laser scanning microscopy (CLSM) images of single nanoprobe (TPE-AMC@F127-AptCD8 (100 μg mL^{-1}, $\lambda_{ex}/\lambda_{em}$ = 405/450 nm), TPE-TCF@F127-

AptCD8 (100 μg mL^{-1}, $\lambda_{ex}/\lambda_{em}$ = 488/660 nm) and AIEgen@F127-AptCD8 (100 μg mL^{-1}, blue channel: $\lambda_{ex}/\lambda_{em}$ = 405/450 nm, red channel: $\lambda_{ex}/\lambda_{em}$ = 405/660 nm) in CD8+ T cells at various pH (from 6.0 to 7.4), respectively. The scale bar is 20 μm for all figures. Quantification of PL intensity of the intracellular fluorescent signals from (D) single nanoprobes (TPE-AMC or TPE-TCF) and (E) AIEgen@F127-AptCD8 in CD8+ T cells at pH conditions. All data are represented as mean ± SD (ns: no significance, *p< 0.05, **p< 0.01, ***p< 0.001, n = 20, one-way ANOVA test). Each point (n = 20) represents one cell from N = 3 independent sample. (F) The linear relationship of $I_{TPE\text{-}AMC}/I_{TPE\text{-}TCF}$ against pH_i (R^2 = 0.9888). (G) Dotted plots of AIEgen@F127-AptCD8 fluorescent signals by flow cytometry in the CD8+ T cell under various pH conditions (DAPI channel for TPE-AMC signals; BV605 channel for TPE-TCF signals). (H) Histogram quantification and (I) Linear progression plot of $I_{TPE\text{-}AMC}/I_{TPE\text{-}TCF}$ against pH values (R^2 = 0.9503) for the flow cytometry data.

2.3.3 Real-time Tracking of pH_i in T Lymphocytes

After cellular uptake of the nanoprobe, we activated the T cells by Dynabeads™ over 7 days and monitored the pH_i of the cells on Day 1, 3, 5, and 7 as the continuous assessment. To verify that our nanoprobe mainly detected pH in cytosol instead of the specific organelle, we further analyzed the signals of co-localizations of AIEgen@F127-AptCD8 with (1) mitochondria, (2) ER or (3) lysosome via staining by Mito-Tracker Green, ER-Tracker Green, or Lyso-Tracker Green, respectively, in living activated CD8+ T cells (**Figure 2.7A**). Our nanoprobe did not particularly prefer to accumulate in any of these organelles as Pearson's overlap coefficients (POC) for mitochondria, ER, and lysosome with the nanoprobe were 0.345, 0.308, and 0.313 <<0.5, respectively. Nevertheless, our results showed that these organelles show differential pH_i readings according to the selected colocalized sites of these organelles. The calculated average pH_i of the lysosome (ROI 1), ER (ROI 2), and mitochondria (ROI 3) were 5.45, 7.02, and 7.91, respectively, in ascending order (**Figure 2.7A**). These pH values are consistent with the literature [195-197]. Therefore, CLSM images of single cells showed that the whole cytosol of cells was "enlightened" by fluorescent signals from AIEgen@F127-AptCD8, while sparse signal spots of Lyso, ER, and Mito-Tracker were observed in cells. These results validate our

hypothesis that glycolysis occurs in the cytosol to mainly influence pH_i in our study.[198] We characterized the successful activation of CD8+ T cells by the enhanced cell expansion and cell growth with a larger cell size compared to non-activated cells (**Figure 2.7B, C**), consistent with the previous report [199, 200]. Meanwhile, non-activated CD8+ T cells were unable to survive for over a week (**Figure 2.7D**). A marked increase in IFN-γ productivity was observed after *ex vivo* stimulation of naïve CD8+ T cells, indicating the pro-inflammatory state of the differentiated T cells **(Figure 2.7E)**. Strikingly, all T_N, T_{CM}, and T_E significantly expanded on Day 1 post-activation with the cell number ratio 28.9:19:1 (**Figure 2.7F**). Moreover, the number of CD8+ T_{CM} showed a 139-fold increase, while the number of T_N decreased by ~ 80% 7 days post-activation compared to those on Day 0. Specifically, we identified that T_{CM} and T_E occupied ~ 95% and 2.73% of the population on Day 7 (**Figure 2.7G, H**). This result is accordant with the literature for robust proliferation by T_{CM} upon T cell activation [201, 202]. Hence, we confirmed that CD8+ T_N simultaneously differentiated into T_E and T_{CM} post-activation, ready for the pH_i detection by our probe.

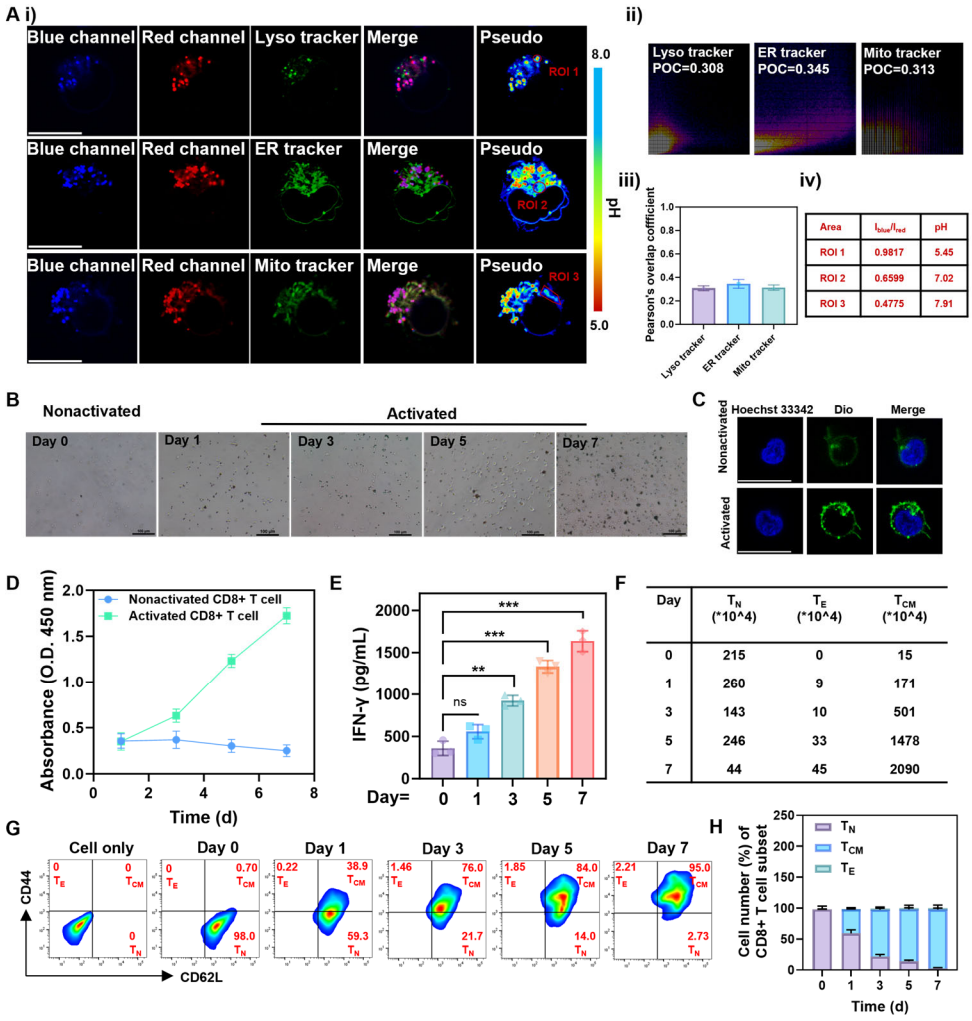

Figure 2.7 *Ex vivo* expansion of CD8+ T cells and organelle colocalization of AIEgen@F127-AptCD8 nanoprobe. (A) (i) Representative CLSM images of colocalization between AIEgen@F127-AptCD8 (blue channel: $\lambda_{ex}/\lambda_{em}$ = 405/450 nm, red channel: $\lambda_{ex}/\lambda_{em}$ = 405/660 nm) and subcellular organelles (green channel: $\lambda_{ex}/\lambda_{em}$ = 488/520 nm) stained with 100 nM Mito-Tracker Green, Lyso-Tracker Green, or ER-Tracker for 30 min in live activated CD8+ T cell, respectively. The scale bar is 10 μm for all figures. The pseudo-color was used to indicate the mapping of pH_i in different cellular compartments. The color strip indicated the pseudo color change observed upon varying the pH. (ii) Statistics of colocalization using Pearson's correlation coefficient. (iii) The table lists the average pH values for the region of interest (ROI) 1-3 regions. (B) Brightfield photos of CD8+ T cells without and with mouse CD3/CD28 Dynabead^{TM} over Day 1, 3, 5, and 7. The scale bar is 100 μm for all figures. (C) Nonactivated and activated CD8+ T (Day 7) cells were stained by nucleus dye Hoechst 33342 and cell membrane dye Dio. The scale bar is 20 μm for all figures. (D) The cell expansion rate of CD8+ T cells before and after activated using CCK-8 assay. (E) IFN-γ expressing of

CD8+ T cells following activation at various time points (Day 0, 1, 3, 5, and 7), n=3. All data are represented as mean ± SD (ns: no significance, *p< 0.05, **p< 0.01, ***p< 0.001, n= 3, one-way ANOVA test). (F) The table shows the statistics of T_N, T_E, and T_{CM} cell subtypes of CD8+ T cells at various time points (Day 0, 1, 3, 5, and 7) following activation. (G) Flow cytometry quantification of the expression profile of surface activation markers (CD44/CD62L) on CD8+ T cells before and after activation. The phenotypes are defined as the following: T_N, $CD44^-CD62L^+$; T_E, $CD44^+CD62L^-$; and T_{CM}, $CD44^+CD62L^+$. (H) The relative proportion of the three T cell subsets on different time points of activation.

To determine the potential entry mechanism of AIEgen@F127-AptCD8 into cells, we pretreated the activated CD8+ T cells with chlorpromazine (inhibitor of clathrin-based endocytosis) or nystatin (inhibitor of caveola-mediated endocytosis) and then incubated the cells with our AIEgen@F127-AptCD8 for 1 h. Strikingly, the cells treated with chlorpromazine showed a 4-fold reduction in fluorescence intensity compared to the untreated group (**Figure 2.8B, C**). However, the nystatin treatment group showed an insignificant effect on the AIEgen@F127-AptCD8 entry compared to the control group. These findings indicate that AIEgen@F127-AptCD8 enters cells via a clathrin-mediated endocytic pathway. Next, our nanoprobe revealed that pH_i gradually decreased post-activation. Our calculated average pH_i of the activated CD8+ T cells on Day 1, Day 3, Day 5, and Day 7 of activation were at 7.11 ± 0.13, 6.84 ± 0.07, 6.63 ± 0.11, and 6.49 ± 0.09, respectively (**Figure 2.8D-E**). Nevertheless, using SNARF^{TM}-1 to probe the pH_i of nonactivated/activated CD8+ T cells showed a similar trend of decreased pH_i to that of our nanoprobe upon T cell activation from Day 0 to Day 7 (**Figure 2.8G**). In addition, we determine the limit of detection (LOD) of our nanoprobe for pH_i determination through different activated CD8+ T cells, ranging from 0 to 12.6×10^4 cells per mL (**Figure 2.8H**). As a result, the calculated LOD is 280 cells per mL, suggesting that the nanoprobe can potentially detect as few as ~ 3 cells in 10 μL of medium.

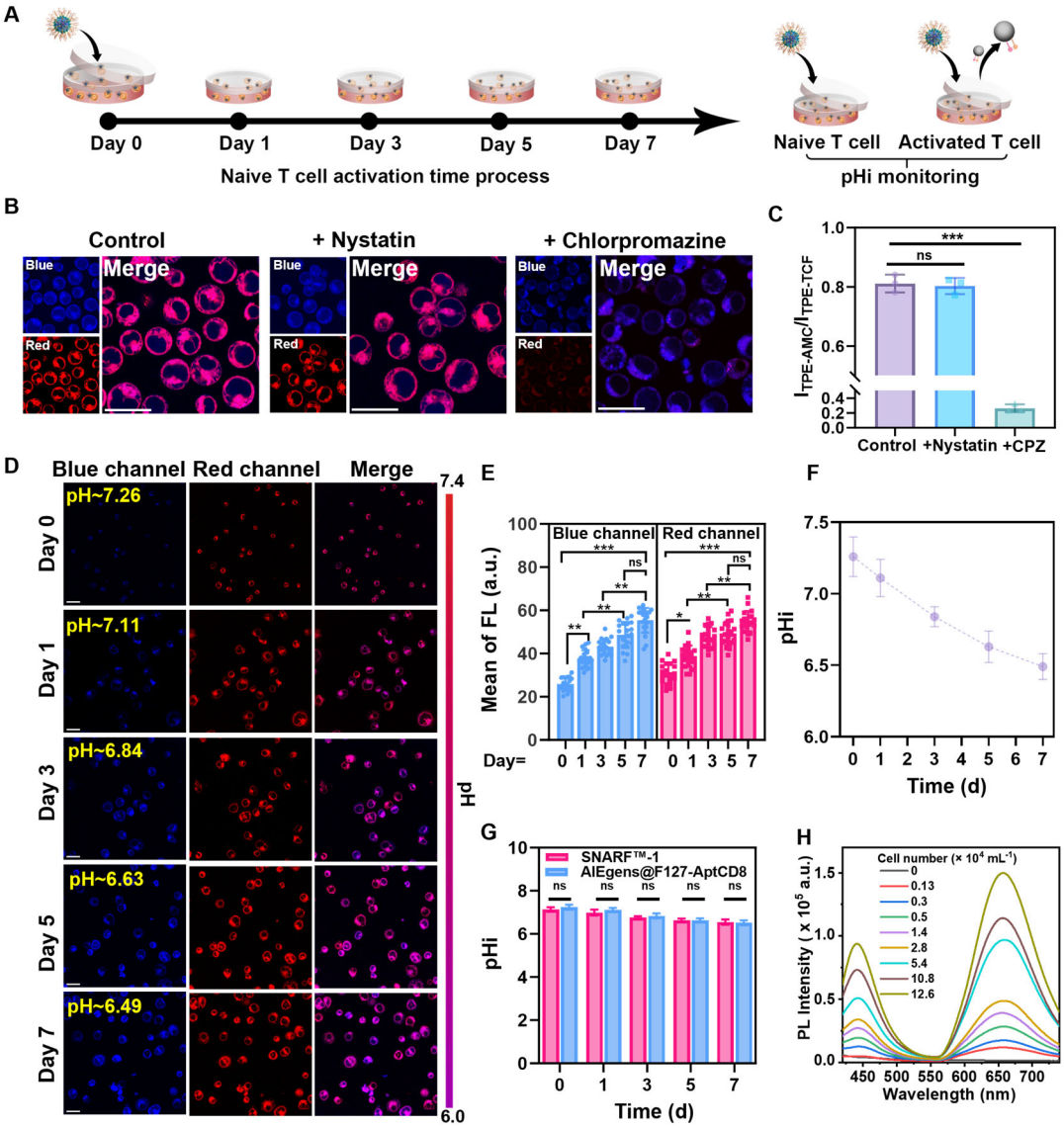

Figure 2.8 Real-time detection of pH_i in CD8+ T cells and entry mechanism of nanoprobe. (A) Schematic illustration of the *in vitro* experimental design. The naïve CD8+ T cells were primed by CD3/CD8 Dynabead™ over different time points. Dynabead™ was removed before pH_i imaging. T cells on Day 0 are nonactivated. (B) Cellular uptake of AIEgen@F127-AptCD8 nanoprobes in the activated CD8+ T cells under various conditions of untreated (positive control), pretreated with nystatin (100 μM) and chlorpromazine (CPZ, 20 μM) for 6 h. The cells were incubated with AIEgen@F127-AptCD8 for 1 h after pre-treatment with endocytosis inhibitors. The cell imaging was performed by confocal microscope (blue, TPE-AMC; red, TPE-TCF. Blue channel: $\lambda_{ex}/\lambda_{em}$ = 405/450 nm, red channel: $\lambda_{ex}/\lambda_{em}$ = 405/660 nm.). The scale bar is 20 μm for all figures. (C) Effects of different treatments on $I_{TPE-AMC}/I_{TPE-TCF}$ ratio following the endocytosis of AIEgen@F127-AptCD8. (D) CLSM images of pH_i in naïve and activated CD8+ T cells probed by

AIEgen@F127-AptCD8 (100 μg mL^{-1}, 1 h incubation) at various time points (from Day 0 to Day 7). Blue channel: $\lambda_{ex}/\lambda_{em}$ = 405/450 nm, red channel: $\lambda_{ex}/\lambda_{em}$ = 405/660 nm. The scale bar is 20 μm for all figures. (E) Quantification of PL intensity of both fluorescent channels for pH_i on different days of activation. Each point (n = 20) represents one cell from N = 3 independent samples. (F) Graphical plot of the measured pH_i against activation time. (G) Comparison of predicted CD8+ T cell pH_i with commercial probes SNARF^{TM}-1 and AIEgen@F127-AptCD8. All data are represented as mean ± SD (ns: no significance, *p< 0.05, **p< 0.01, ***p< 0.001, one-way ANOVA test). (H) PL spectrum of varying numbers of activated CD8+ T cells (from 0 to 12.6 × 10^4 cells per ml) incubated at a concentration of 100 μg mL^{-1} AIEgen@F127-AptCD8 for 1 h.

2.3.4 Metabolic Association Between T Cell State and pH_i

To elucidate the effect of physiological response on pH_i, we evaluated the amount of LA secretion as the major source of vigorous H^+ production and ATP as the major energy source during activation (**Figure 2.9A**). Strikingly, we obtained elevated levels of LA and ATP in T cells. For instance, activated CD8+ T cells on Day 7 secreted 1.5-fold and 4-fold higher levels of LA and ATP than those in nonactivated T cells, respectively. Note that the basal level of ATP in T_N was minimal (0.05 μmol L^{-1}), indicating low activity at the naïve state. Interestingly, the content of produced LA and ATP also showed linearity against the date of activation, consistent with that of the pH_i change. Finally, we assessed the correlation coefficient between LA or ATP concentration and pH_i in both naïve and activated CD8+ T cells (**Figure 2.9B, C,**). Notably, our results indicated that metabolic events in terms of glycolytic products, LA or ATP, were positively proportional to decreased pH_i of T cells (R^2 = 0.9513 and R^2 = 0.9641, respectively, **Figure 2.9D, E**). It is known that activated CD8+ T cells *in vitro* undergo a dramatic increase in aerobic glycolysis. ATP and LA are the major products of glycolysis and LA can contribute to proton production, leading to the decrease of pH_i Thus, the T cell activation-mediated glycolytic process strongly influences pH_i and we established the relationship between this metabolism and pH_i by our nanoprobe. To validate this metabolic/pH_i association, we pre-treated the cells with 2-Deoxy-D-glucose (2-DG), a glycolysis inhibitor, and subsequently incubated the CD8+ T cells with our AIEgen@F127-AptCD8. The results demonstrated that

the $I_{TPE-AMC}/I_{TPE-TCF}$ of the 2-DG treated activated CD8+ T cells significantly decreased (indicating a higher pH_i) compared to those in untreated activated CD8+ T cells, while the signal ratios insignificantly changed between the 2-DG treated and untreated naïve CD8+ T cells (**Figure 2.9F, G**). Thus, this pharmacological inhibition experiment verifies the correlation between glycolysis and pH_i in both activated and nonactivated CD8+ T cells.

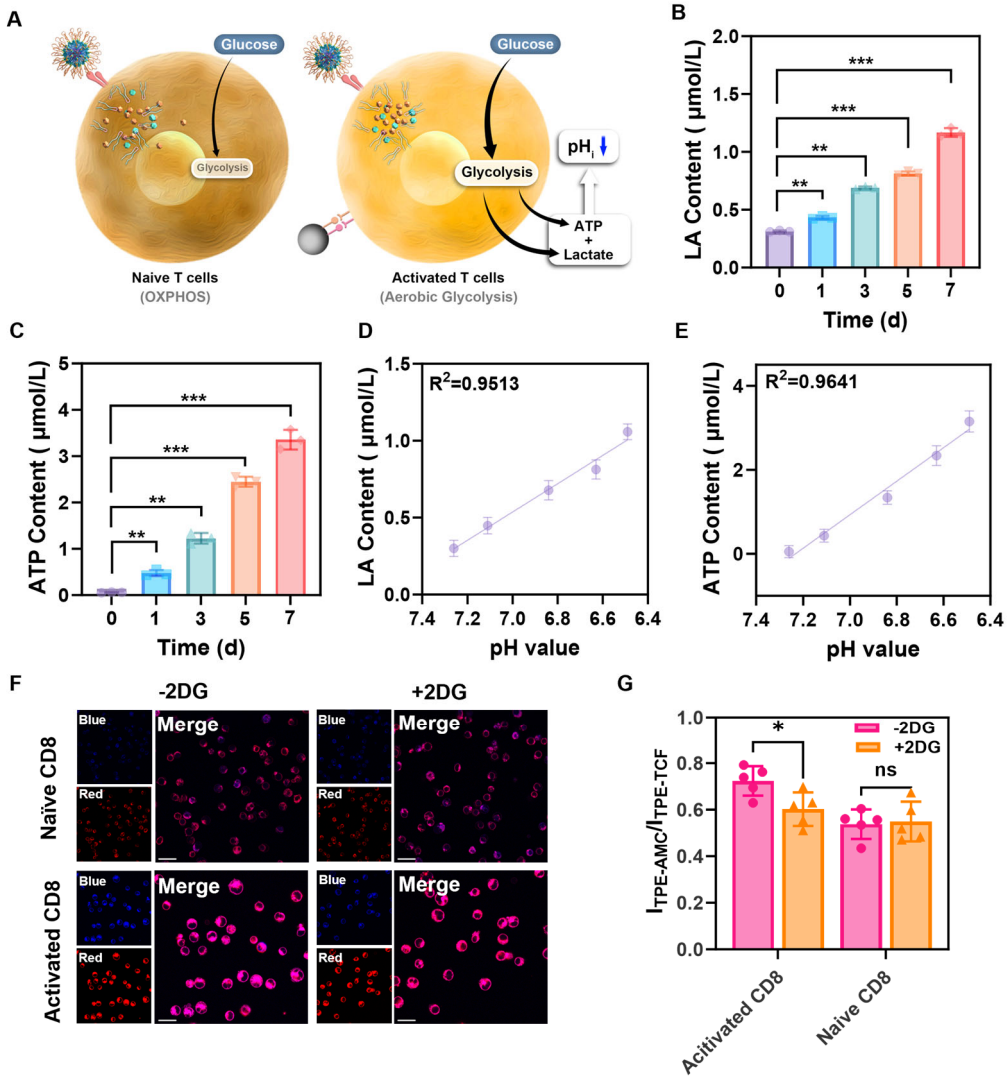

Figure 2.9 Mechanistic investigation of the association between metabolic events and pH_i in different statuses of CD8+ T cells. (A) Schematic illustration of the representative metabolic pathway of glucose consumption in naïve T cells and activated T cells, which mainly undergo OXPHOS, and aerobic glycolysis, respectively. Activated T cells intensively converted glucose into ATP and LA as metabolic products. Quantification of (B) LA content and (C) ATP content of the naïve and activated CD8+ T cell at various time points (Day 0, 1, 3,

5, and 7) following activation. All data are represented as mean ± SD (ns: no significance, *p< 0.05, **p< 0.01, ***p< 0.001, n = 3, one-way ANOVA test). The fitting logarithmic curve of (D) LA content and (E) ATP content against pH_i in CD8+ T cells, respectively. (F) The impact of 2-DG (10 mM) on the pH_i fluctuations was assessed in naïve CD8+ T cells and activated CD8+ T cells. CLSM images were captured after a 6 h treatment of cells with 2-DG, followed by a 1h incubation with nanoprobes. The scale bar is 20 μm for all figures. (G) Ratio $I_{TPE\text{-}AMC}/I_{TPE\text{-}TCF}$ quantification in naïve and activated CD8+ T cells, n = 5.

2.4 Summary

In summary, we specially design and fabricate a nanoprobe based on AIE and dual emitting enhancement that can rapidly, sensitively, and selectively monitor pH_i in different states of CD8+ T cells. The overall large stoke shift (donor: $\lambda_{ex}/\lambda_{em}$ = 405/450 nm; acceptor: $\lambda_{ex}/\lambda_{em}$ = 450/660 nm) of the dual channels suppresses crosstalk between the excitation source and the fluorescent emission for a high signal-to-noise ratio. The pH response property of TPE-AMC in nanocore empowers the effect of AIE that promotes pH sensitivity of the nanoprobe and ascertains dual emitting enhancement through FRET. Critically, this nanoplatform demonstrates a wide response range for dual emitting analysis of D/A signal ratio against pH from 10.0 to 3.0, as well as the small linear range at pH_i from 6.0 to 7.4 that is suitable for *in vitro* diagnosis (LOD is 280 cells per mL). We show that most activated CD8+ T cells shift to T_{CM} (majority) and T_E (minority) from T_N throughout 7 days of activation. By employing this nanoprobe, we reveal that CD8+ T cells become more intracellularly acidic post-activation due to the robust production of LA via glycolysis. Generally, we determine that the pH_i of naïve CD8+ T cells and activated CD8+ T cells 7 days post-stimulation is ~ 7.26 and ~ 6.49, respectively. This work not only provides a powerful AIE/dual emitting imaging agent for distinguishing activated and nonactivated T cells by probing pH_i but also provides insight into the metabolic events to predict immune cell states. The potential application of our nanoprobe *in vivo* model remains limited as the current excitation wavelength for our nanoprobe is low tissue-penetrating. Further investigation is required to optimize the nanoprobe design with a more tissue-penetrating and low-scattering excitation source, such as the near-infrared wavelengths. We foresee that an

advanced structural modulation of the AIE-based D/A pair towards the first/second NIR optical windows is highly promising for dynamic pH_i probing *in vitro* and *in vivo*, offering suppressed imaging background and deep tissue penetration. Our AIEgen-based pH_i nanoprobe has presented a strong association between pH_i and T cell states. Hence, it is possible to apply our probe with other functional assays, such as cytokine profiling or gene expression analysis, to facilitate the elucidation of the relationship between pH_i profile, and intracellular signaling pathway or epigenetics. Overall, this nanoprobe offers valuable insights into the dynamic pH_i changes occurring in different differentiated immune T cells, thereby providing distinctive avenues for characterizing immune cell dynamics.

Chapter 3: A Novel Aptameric Biosensor Based on Germanene Nanosheet for Rapid and Sensitive BRCA1 Mutation Detection

3.1 Introduction

Breast cancer remains one of the most prevalent malignant tumors worldwide [203]. The BRCA1 is recognized as a critical tumor suppressor gene, and mutations in BRCA1 can disrupt DNA repair mechanisms, significantly elevating breast cancer risk [204]. It is known that human BRCA1 and BRCA2 (another breast cancer susceptibility gene) are highly expressed in tumor-infiltrating CD8+ mitotic tissue-resident memory T cells, suggesting a potential role of BRCA1 in promoting antitumor immunity [205]. Consequently, effective detection of BRCA1 mutations is crucial for early diagnosis, prevention, and treatment of the disease. Traditional methodologies for BRCA1 detection, such as single-strand conformation polymorphism analysis, high-performance liquid chromatography, and DNA sequencing, face obstacles related to time consumption, cost, and procedural complexity [206-208]. There is a pressing need for the development of rapid, sensitive, cost-effective, and straightforward methods for BRCA1 detection.

Currently, several advanced technologies are employed to detect BRCA1 genes, including fluorescence sensors [209], surface plasmon resonance [210], electrochemiluminescence [211], and electrochemical sensors [212]. Among these, fluorescence sensors stand out due to their rapid signal response, high sensitivity, and non-invasive nature, making them promising for gene and mutation detection [213, 214]. Various nanomaterials like AuNPs [215], gold nanorods [216], and carbon nanotubes [217] are extensively utilized as effective fluorescence quenchers in FRET sensors, owing to their superior light-quenching capabilities. Compared to other nanomaterials, 2D nanosheets such as graphene, tungsten disulfide, and MoS_2 offer distinct advantages, including extensive surface area, substantial adsorption capacity, excellent biocompatibility, minimal toxicity, and tunable optical properties, making them widely used in biosensors [218, 219]. Due to the π-π stacking interaction, ssDNA can be strongly adsorbed on the nanosheets,

resulting in a large amount of fluorescence quenching of the organic dye-labeled on the ssDNA through FRET between the nanosheet planar structure and the dye molecules [220].

Germanene, a 2D graphene-like nanomaterial, exhibits a large surface area and favorable biocompatibility, however, the potential of germanene nanosheets in fluorescent sensors remains largely underexplored [221], [222]. Covalent functionalization of germanene with methyl or hydroxyl functional groups enables tunable direct band gap (1.8 eV), resulting in red-emitting fluorescence [223]. The majority of current nanosheets employed for nucleic acid detection rely on single-channel methods, as they lack inherent luminescent properties. This limitation presents a unique opportunity to explore the intrinsic fluorescent characteristics of mGeNS and their potential applications in nucleic acid sensing. Thus, we hypothesize that the mGeNS could parallel the properties of other ratiometric-based fluorescent biosensors, offering a distinctive dual emission detection of the BRCA1 gene.

Based on this insight, we synthesized GeT-NSs of varying sizes through ultrasonication for bulk mGe in 1% Triton™ X-100 (TX100) over different durations, followed by an investigation into their photophysical and fluorescence quenching properties concerning fluorescent oligonucleotides. The GeT-NSs exhibit an emission intensity of 640 nm and possess a broad absorption spectrum ranging from 300 to 1000 nm. Subsequently, we explored their ability to detect BRCA1 by attaching the corresponding BRCA1 gene aptamer onto the GeT-NSs surface, termed GeT-NSs@FAM-cDNA probe. Fluorescein amidite (FAM), a popular fluorescein label for molecular beacons, was used to label the ssDNA aptamer. Upon binding with a fluorescent oligonucleotide (FAM-cDNA), the fluorescence is quickly quenched by GeT-NSs through the energy transfer effect, exhibiting a fluorescence "off" state. The addition of target ssDNA, the BRCA1 mutant sequence, triggers a restored fluorescence process resulting in a switch to an "on" state that allows for detection via ratiometric fluorescence emission signals (I_{520}/I_{640} nm). The selectivity and sensitivity of this system were validated using mismatch sequences, demonstrating that GeT-NSs@FAM-cDNA nanoprobes can rapidly detect the BRCA1 mutant gene within about 30 min with high sensitivity at the picomolar level, without the need for

amplification. This development marks a significant advancement in the field of nucleic acid detection and opens new avenues for using mGeNS in biomedical applications.

3.2 Methods

3.2.1 Preparation and Characterization of GeT-NSs

The production of mGeNS is based on the established method of preparing nanosheets through liquid-phase exfoliation. Initially, 30 mg of mGe powder was suspended in 30 mL of N-methyl-2-pyrrolidone (NMP) to form a mGe suspension. This solution was then purged with nitrogen to remove oxygen, preserving the stability of mGeNS and preventing its decomposition. Subsequently, the mixture was subjected to ultrasonication in an ice bath for 6 h using a 500W ultrasonic cell disruptor. Following the ultrasonication, a sample of the mGeNS solution was centrifuged at 3000 rpm for 10 min. The sediment was collected as the bulk mGe, while the supernatant underwent further high-speed centrifugation at 12000 rpm for 15 min to isolate monolayer mGeNS. For further purification, the multilayer mGeNS were redispersed in 1% TX-100 solution (100 μL TX-100 in 10 mL DI water) and ultrasonicated again for 1 to 4 h. The final step involved centrifuging the GeT-NSs solution at 12000 rpm for 15 min to collect the monolayer GeT-NSs. The collected material was washed twice with ethanol and stored at 4 °C. The size, morphology, and micro-structural features of GeT-NSs were further characterized by DLS (Zetasizer pro, Malvern), XRD (X-ray Diffractometer, Rigaku SmartLab), AFM (Scanning Probe Microscope, Bruker MultiMode 8), SEM (Scanning Electron Microscope, TESCAN VEGA3) and TEM (Field Emission Transmission Electron Microscope, JEOL JEM-2100F).

3.2.2 Photophysical Properties Evaluation of GeT-NSs

The photophysical properties of GeT nanosheets of different sizes were obtained by Raman spectroscopy, UV-Vis spectroscopy, and fluorescence spectroscopy. For Raman spectroscopy, data were collected under a 532 nm laser excitation across a scan range of 0-500 nm, with a 1%

laser power setting, an exposure time of 10 sec, and an accumulation of three repeats. The UV-Vis absorption spectrum were recorded from 300 to 1000 nm at a scanning rate of 600 nm min^{-1} and a slit width of 2 nm. The excitation-emission spectrum were generated by varying the excitation wavelength from 340 to 520 nm, with an excitation slit width of 5 nm and an emission slit width of 10 nm, and a step size of 1 nm.

3.2.3 Photostability Evaluation of GeT-NSs

To evaluate the photostability of GeT-NSs, we conducted a series of experiments analyzing the PL intensity of these nanosheets under various conditions. The assays included assessing the PL intensity at different pH levels ranging from 4.0 to 10.0, both before and after exposure to a temperature of 37 °C. Additionally, the stability of GeT-NSs was tested in various solvents, including NMP, isopropyl alcohol (IPA), Tris-HCl buffer, DI water, and PBS.

3.2.4 Preparation of GeT-NSs@FAM-cDNA Nanoprobe

The DNA fragment sequences utilized in this work are detailed in **Table 3.1**. Based on the target sequence of the BRCA1 gene, a ssDNA probe was engineered with a FAM dye attached to its 5' end, referred to as FAM-cDNA. GeT-NSs were suspended in Tris-EDTA (TE) buffer and sonicated for 1 h to ensure a uniform dispersion in the aqueous phase before the adsorption of FAM-cDNA, resulting in the formation of the GeT-NSs@FAM-cDNA nanoprobe.

To evaluate the quenching efficiency (*Qe*) of GeT-NSs towards FAM-cDNA, a consistent concentration of 10 nM FAM-cDNA was mixed with varying concentrations of GeT-NSs dispersion (ranging from 0 to 300 μg/mL) and incubated for 15 min at room temperature. The fluorescence intensity was then measured using a spectrofluorometer. The *Qe* of GeT-NSs was calculated using the formula $Q_e\ (\%) = (F_0 - F_q) / F_0$, where F_0 is the initial fluorescence signal of 10 nM FAM-cDNA, and F_q is the fluorescence intensity after FAM-cDNA has been absorbed onto GeT-NSs at various concentrations. Each experimental condition was replicated three times to ensure reliability.

3.2.5 Detection of BRCA1 Gene

In a typical measurement, 10 nM FAM-cDNA was mixed with the GeT-NSs (0.1 mg ml^{-1}) in 10 mM TE (pH 7.4) containing 100 mM NaCl and 4 mM $MgCl_2$ for 15 min. Afterward, target BRCA1 DNA with different concentrations (from 0 to 30 nM) was added to the mixture and hybridized with FAM-cDNA for 30 min at 37 °C. The fluorescence of the mixture was measured. To evaluate the specificity and selectively of GeT-NSs@FAM-cDNA nanoprobe towards BRCA1 Gene sequence, we selected control groups with one-base mismatched DNA sequence (b1mis-DNA), two-base mismatched DNA sequence (b2mis-DNA), and non-complementary DNA sequence (nc-DNA). These control sequences were incubated with GeT-NSs@FAM-cDNA with the same operation as the target BRCA1 DNA gene. The fluorescence spectrum of all the samples were measured with excitation wavelength at 480 nm and emission wavelength from 500 nm to 800 nm. All the detection experiments were conducted with three independent samples for each group.

Table 1 List of the sequences used in this work

Name	Sequence (5'-3')
Capture probe (FAM-cDNA)	CTT ACC AGA TGG GAC AC
Target DNA (BRCA1)	CTA TGC AGA AAA ATC TTA GAG TGT CCC ATC TGG TAA G
One base mismatch DNA (b1mis-DNA)	CTATGCAGAAAATCTTAGAGTGTCCCATCTG**C**TAAG
Double base mismatch (b2mis-DNA)	CTATGCAGAAAATCTTAGAGTGT**G**CCATCTG**C**TAAG
Noncompelmentray DNA (ncDNA)	TGCGATCTTTTTCACCGAGACGCAAAGACATACGGT
miRNA21	TAG CTT ATC AGA CTG ATG TTG A
miRNA150	TCT CCC AAC CCT TGT ACC AGT G

3.2.6 Agarose gel electrophoresis

GeT-NSs@FAM-cDNA probes, FAM-cDNA, target BRCA1 ssDNA, and probe-target DNA complex (GeT-NSs@FAM-cDNA+BRCA1, GeT-NSs@FAM-cDNA+b1misDNA, GeT-NSs@FAM-cDNA+b2misDNA, GeT-NSs@FAM-cDNA+ncDNA) were analyzed on 5%

agarose gel electrophoresis premixed with 0.1% SYBR®gold dye. Briefly, all the test samples were prepared by mixing the probes, cDNA, and probe-ssDNA complex with BlueJuice gel loading buffer (v/v, 9/1) followed by loading on the gels. DNA ladder (size range: 10 bp ~ 300 bp) in the same buffer was also loaded into the gel to assess the bp number of DNA fragments. Then, the agarose gels were run in 0.5X TBE buffer at a constant voltage (80 V) for 2 h for maximum separation. Finally, the agarose gels were observed under a UV transilluminator, and photographs were taken by a Chemi Doc system (Bio-Rad).

3.3 Results and Discussion

3.3.1 Synthesis and Characterization of GeT-NSs

Liquid-phase sonication is an effective technique for producing few-layered germanene by disrupting weak van der Waals forces [224]. In this study, TX-100, a nonionic surfactant, was utilized to enhance the dispersibility of hydrophobic methyl germanene. Different sizes of GeT-NSs were successfully synthesized according to the probe sonication for liquid-phase exfoliation (**Figure 3.1A**). The morphology and size distribution of GeT-NSs were evaluated by SEM and AFM, respectively. The results revealed that GeT-NSs exhibit morphology with a size range of 100 to 200 nm after 4 h ultrasonic exfoliation (**Figure 3.1B**) and a thickness of approximately 5 nm (**Figure 3.1D**). High-resolution transmission electron microscopy (HRTEM) confirmed the methyl germanene structure, revealing a well-resolved lattice indicative of its single-crystal nature. The measured inter-lattice distance of 0.202 nm corresponds to the (220) crystal planes of methyl germanene (**Figure 3.1E**).

Further XRD investigations of both bulk mGe and GeT-NSs revealed diffraction peaks at 27.3 °, 44.4 °, 64.7 °, and 82.0 °, aligning with the expected (111), (220), (400), and (422) crystal face, consistent with findings from previous studies [225] (**Figure 3.1E**). Raman spectroscopy of bulk mGe and GeT-NSs of varying sizes indicated typical peaks for methyl germanene at around 299 cm^{-1} (**Figure 3.1F**). Notably, a blue shift in the Raman peaks from 301 to 266 cm^{-1} was observed, suggesting that transitioning from multilayer to single-layer nanosheets and a size reduction can influence the vibrational characteristics of these materials.

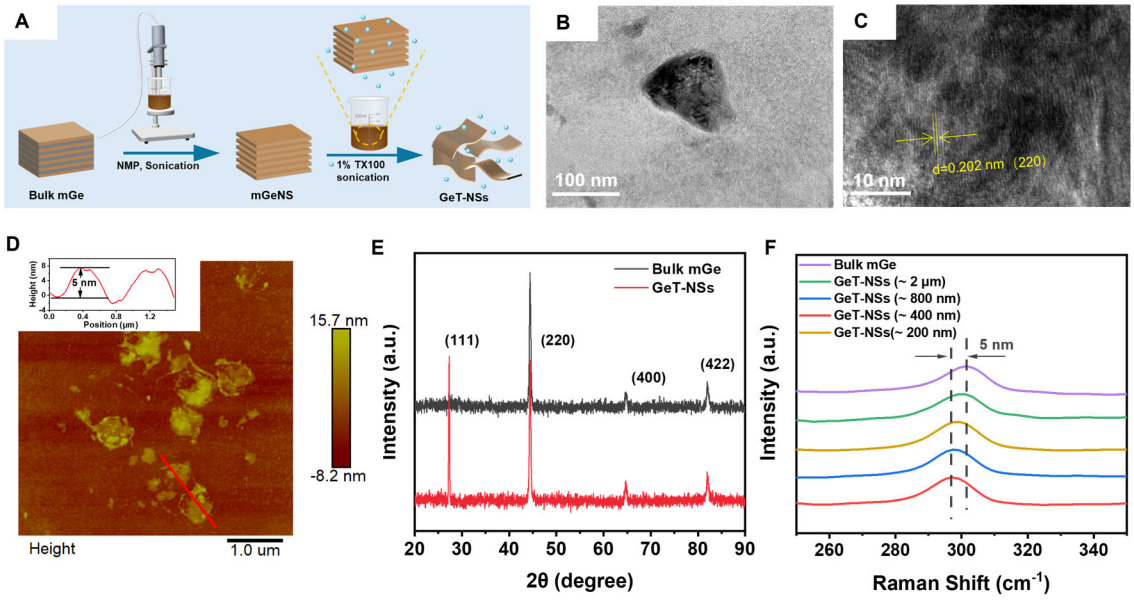

Figure 3.1 Preparation and characterization of GeT-NSs. (A) Schematic of the preparation process of GeT-NSs. (B) The TEM image and (C) FFT-masked HRTEM image of GeT-NSs. The scare bar is 100 nm and 10 nm, respectively. (D) AFM image and height profile of GeT-NSs. (D) XRD pattern of mGe bulk and GeT-NSs. (F) Raman spectrum of mGe bulk and GeT-NSs with different sizes.

In addition, the size variations of GeT-NSs produced under different ultrasonication durations in a 1% TX100 solution were characterized using both SEM and TEM (**Figure 3.2**). The findings indicated that single-layer mGeNS are effectively produced through ultrasonication in NMP. As the ultrasonication time in the 1% TX-100 solution was extended, a notable reduction in the size of GeT-NSs was observed, with dimensions decreasing from 2 μm to 200 nm, which is consistent with DLS data (**Figure 3.3A**). This demonstrates the controllability of the exfoliation process and the influence of sonication duration on the resultant nanosheet dimensions.

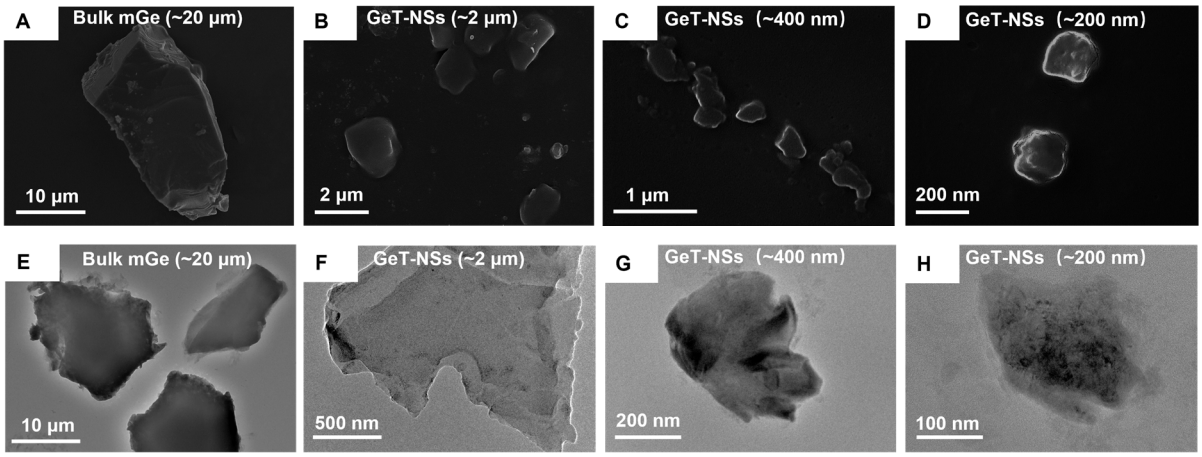

Figure 3.2 Morphological characterization of GeT-NSs. SEM image of (A) Bulk mGe (~ 20 μm), (B) GeT-NSs (~ 2 μm), (C) GeT-NSs (~ 400 nm), and (D) GeT-NSs (~ 200 nm), and the corresponding TEM image of (E) Bulk mGe (~ 20 μm), (F) GeT-NSs (~ 2 μm), (G) GeT-NSs (~ 400 nm) and (H) GeT-NSs (~ 200 nm).

In addition, we evaluated the potential of GeT-NSs produced after different ultrasonic treatment times in 1% TX-100 solution (**Figure 3.3B**). Initially, the potential of mGeNS in ultrapure water was measured to be 15.8 ± 3.65 mv. As the ultrasonic treatment time increased, the potential of GeT-NSs gradually increased to 3.52 ± 0.91 mv. This increase was attributed to the increased contact between the non-ionic surfactant and the nanosheets during the ultrasonic treatment process, increasing from potential [226]. UV-Vis spectroscopy was employed to analyze the optical properties of exfoliated GeT-NSs of varying sizes (**Figure 3.3C**). The absorption spectrum demonstrated a distinct relationship with the size and thickness of the nanosheets. Notably, a gradual reduction in the absorption spectrum was observed as the size of the nanosheets decreased, probably due to the increase in light scattering. The size reduction of GeT-NS induces a variation in the direct band gap, ranging from 2.44 to 2.75 eV, which manifests as a blue shift in the fluorescence emission peak (**Figure 3.3D**). This shift indicates that the optical properties of GeT-NS are sensitive to changes in their physical dimensions, a phenomenon commonly observed in nanoscale materials [227]. The findings underscore the distinctive photoluminescence characteristics exhibited by GeT-NSs, thereby establishing a foundation for their prospective applications as fluorescent sensing platforms.

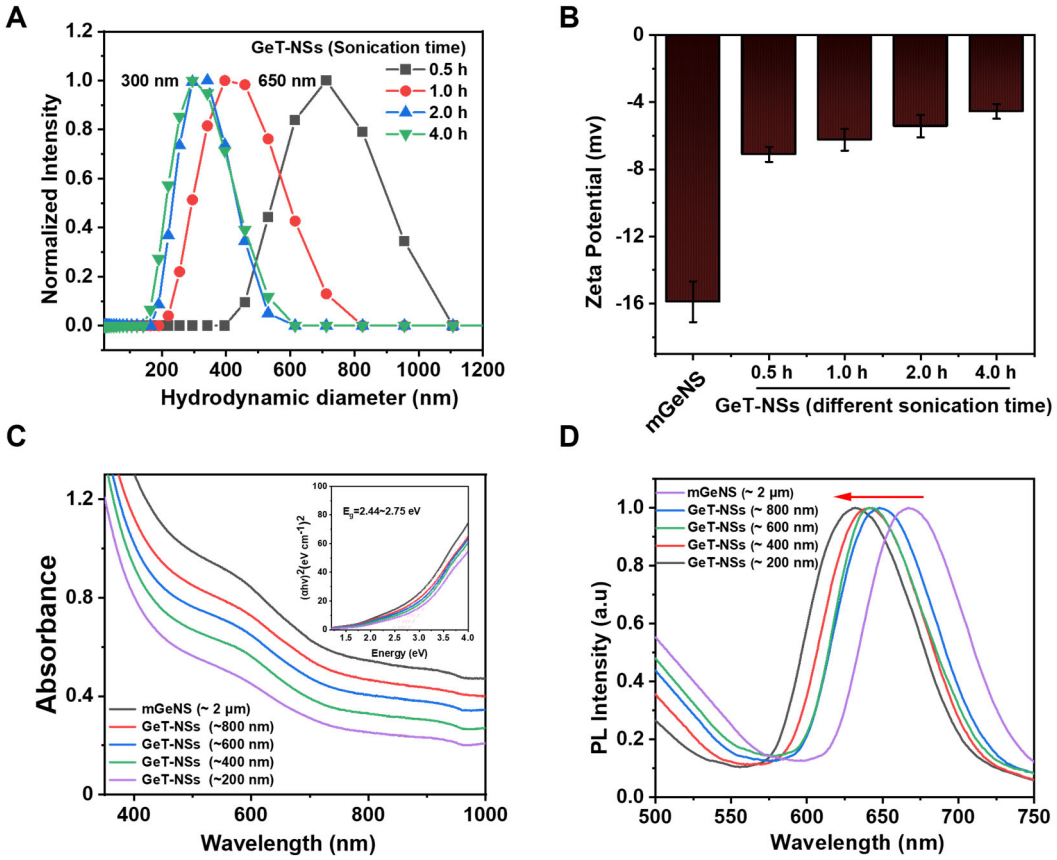

Figure 3.3 Size dependence of photophysical properties of GeT-NSs. (A) DLS and (B) zeta potential analysis of different sonication-prepared GeT-NSs. (C) UV-Vis spectrum and (D) PL spectrum of different sizes of GeT-NSs. λex = 480 nm. The inset shows the optical band gap calculated by the $(\alpha h\nu)^2$ *vs* photo energy (*hν*) of the UV-Vis curve.

We investigated the photophysical properties and photostability of GeT-NSs since photostability is an essential property for fluorescent sensors. Excitation-emission matrix (EEM) spectrum exhibited excitation wavelength-independent fluorescence emission, indicating that the size of GeT-NSs is uniform (**Figure 3.4A**). A proportional relationship was observed between the fluorescence emission intensity and the concentration of GeT-NSs within the range of 0 to 200 μg mL^{-1}, wherein an escalation in the nanosheet concentration led to a corresponding increase in the fluorescence intensity. (**Figure 3.4B**). The stability of GeT-NSs was assessed by monitoring the fluorescence emission spectrum in different solvents (e.g. NMP, IPA, 1% TX100, PBS, DI water, and TE buffer). The results indicated that the stability of GeT-NSs was

maintained stable, with negligible changes in fluorescence emission intensity (**Figure 3.4C**). The fluorescence emission intensity decreased by about 5% after incubation at 37 °C for 1 h compared with room temperature, which is negligible (**Figure 3.4D**). In addition, we also observed the fluorescence intensity of GeT-NSs at different pH values. The fluorescence intensity was slightly red-shifted in acidic conditions and slightly blue-shifted in alkaline conditions (**Figure 3.4E, F**). We suspect that this is due to the degradation or denaturation of GeT-NSs under severe conditions. These results indicate that the synthesized GeT-NSs exhibited sufficient stability in neutral conditions for sensing applications.

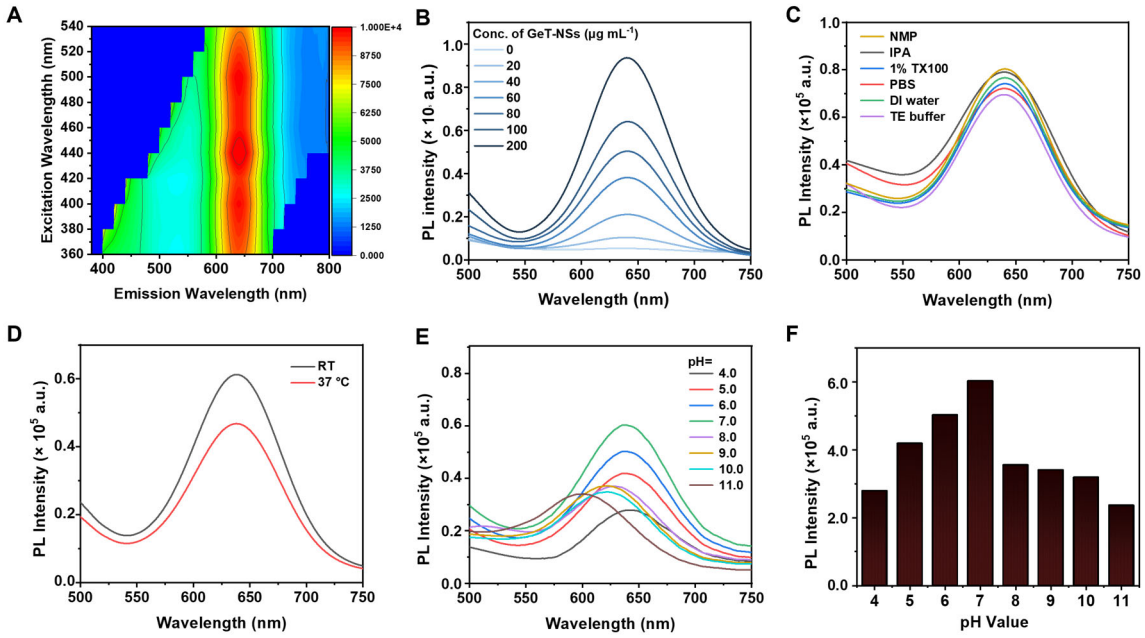

Figure 3.4 Photostability evaluation of GeT-NSs (size ~ 400nm). (A) Excitation emission matrix (EEM) PL spectrum of GeT-NSs upon different excitation wavelengths from 340 nm to 520 nm. (B) PL spectrum of GeT-NSs at different concentrations from 0 to 200 μg mL^{-1} under 480nm excitation. (C) PL spectrum of 100 μg mL^{-1} GeT-NSs in different solvents. (D) PL spectrum of GeT-NSs at room temperature and after incubation at 37 °C for 1h. (E) PL spectrum of GeT-NSs at pH values from 4.0 to 11.0. (F) Fluorescence emission peaks of GeT-NSs at 640nm corresponding to different pH values. λ_{ex} = 480 nm, λ_{em} = 500-750 nm

3.3.2 Preparation and Characterization of GeT-NSs@FAM-cDNA nanoprobe

We prepared the GeT-NSs@FAM-cDNA via the hydrophobic and Van der Waals interactions between the GeT-NSs and FAM-cDNA. We first evaluated the absorption and PL spectrum of GeT-NSs and FAM-cDNA, respectively (**Figure 3.5A**). The absorption spectrum of FAM-cDNA exhibited a peak at 488 nm, while its maximum fluorescence emission was observed at 520 nm. Within the wavelength range of 300-1000 nm, a spectruml overlap was observed between the emission profile of GeT-NSs and their corresponding absorption spectrum. This overlap suggests that upon adsorption of FAM-cDNA onto the surface of GeT-NSs, fluorescence quenching of the FAM moiety would occur due to FRET. GeT-NSs with different sizes exhibited a good FAM-cDNA quenching effect (**Figure 3.5B**). When FAM-cDNA was incubated with the GeT-NSs, the emission peak at 520 nm was significantly quenched, demonstrating the potential of GeT-NSs as an efficient dye quencher. We then incubated 5 nM FAM-sDNA with different concentrations of GeT-NSs (from 0-300 μg mL^{-1}) and found that as the concentration of GeT-NSs increased, the emission peak of FAM-sDNA gradually decreased (**Figure 3.5C**). When the concentration of GeT-NSs was around 100 μg mL^{-1}, the fluorescence intensity dropped to the minimum. We calculated the *Qe* of FAM-sDNA (λ_{em} = 520 nm) in GeT-NSs according to the formula $Q_e\ (\%) = (F_0 - F_q) / F_0$ and obtained a *Qe* of 89.9% (**Figure 3.5D**).

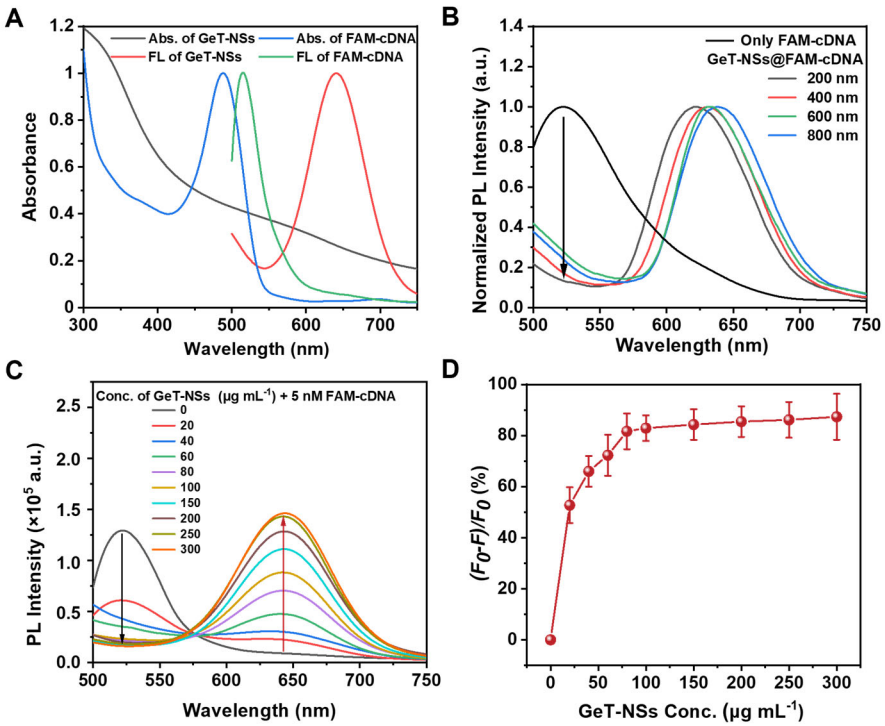

Figure 3.5 The quenching efficiency of GeT-NSs. (A) UV-Vis and PL spectrum of GeT-NSs and FAM-cDNA. (B) PL spectrum of FAM-cDNA after quenched by GeT-NSs at a series of sizes. (C) PL spectrum of FAM-cDNA after quenched by GeT-NSs (~ 400 nm) at a series of concentrations. (D) The plot of *Qe* % versus different concentrations of GeT-NSs nanosheets. F_0: fluorescence intensity of FAM-cDNA. F_q: fluorescence intensity of FAM-cDNA after adding GeT-NSs to form GeT-NSs@ FAM-cDNA. $\lambda_{ex}/\lambda_{em}$ = 480/520nm.

3.3.3 Rapid Detection of BRCA1 Gene

Since GeT-NSs can completely quench the fluorescence of FAM-cDNA, we hypothesized that the complementary BRCA1 Gene DNA fragment could restore the fluorescence of FAM-cDNA (**Figure 3.6A**). First, we observed that FAM-labeled cDNA exhibits strong emission at 520 nm, while GeT-NSs exhibits strong emission at 640 nm (**Figure 3.6B**). After the addition of GeT-NSs, the fluorescence of FAM-labeled cDNA was dramatically quenched to almost a minimum due to the energy transfer from FAM to GeT-NSs. Upon hybridization of the probe with the target BRCA1 DNA sequence, a weakening of the quenching effect occurs, leading to a restoration of the fluorescence intensity associated with the FAM moiety (**Figure 3.6C**). This is due to the shielding of the nucleotide bases by the double helix rigid structure of dsDNA and

the phosphate backbone, which weakens the interaction between the nucleotide bases and the GeT-NSs surface. Furthermore, we noticed a reduction in the fluorescence peak of GeT-NSs, mainly due to the inner filter effect. The results indicate a strong linear relationship (R = 0.976) between the fluorescence intensity ratio of FAM-cDNA to GeT-NSs and the concentration of BRCA1 ssDNA, within the range of 0 to 35 nM (**Figure 3.6D)**. The fluorescence assay also demonstrates a low detection limit (3 times the signal-to-noise ratio) of 56 pM.

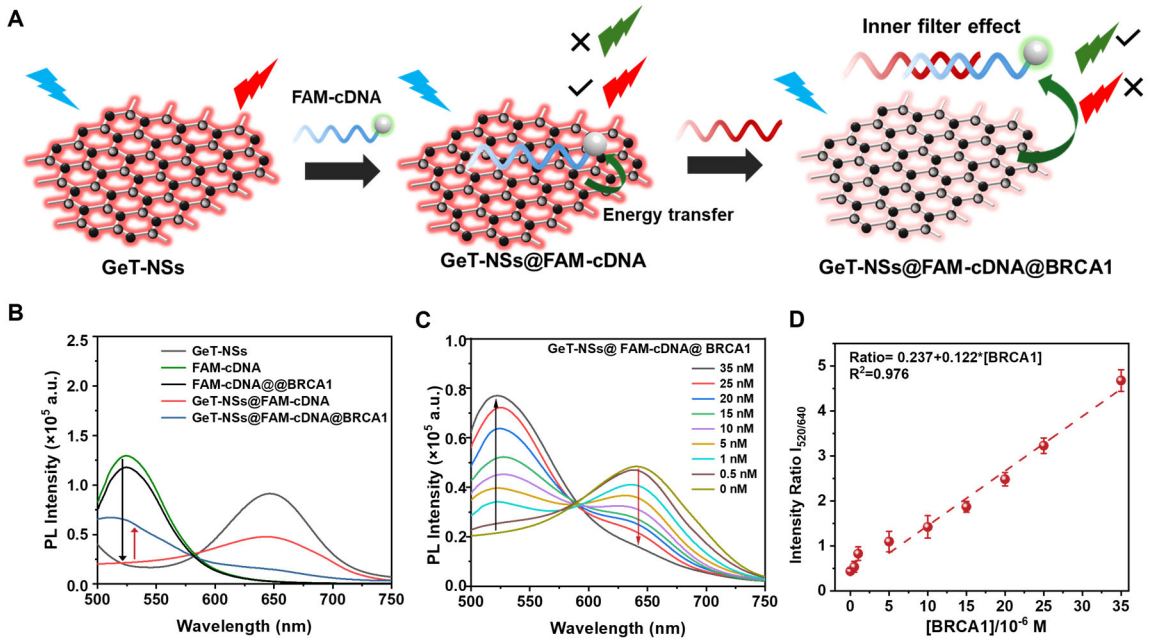

Figure 3.6 GeT nanosheet-based BRCA1 gene detection. (A) Schematic illustration of GeT-NSs based BRCA1 gene detection. (B) PL spectrum of the FAM-cDNA (green line), FAM- cDNA @BRCA1 (black line), GeT-NSs (gray line), GeT-NSs@FAM-cDNA (red line), and FAM-ssDNA@FAM-cDNA@BRCA1 (blue line), respectively. (C) PL spectrum of GeT-NSs@FAM-cDNA probe with different concentrations of BRCR1 (λ_{ex} = 480 nm). (D) Relationship between the ratiometric fluorescence intensity (I_{520}/I_{640}) and BRCA1 gene concentration. Each point corresponds to the fluorescence intensity for the indicated BRCA1 concentration. All error bars are the standard error of the fluorescence intensity from three data points.

The suitability of FAM-cDNA@GeT-NSs for ratiometric fluorescence imaging was evaluated using a commercial *in vivo* imaging station (IVIS) equipped with FAM and GeT-NSs imaging channels. Separate wells containing varying concentrations of FAM-cDNA@GeT-NSs (0-20 nM) were incubated for 30 min with different concentrations of BRCA1 (0-10 nM), and

then multiwell plates were imaged. The detection images revealed that the FAM fluorescence intensity (and the FAM/GeT-NSs ratio) increased with higher BRCA1 concentrations (**Figure 3.7A-C**). Conversely, the GeT fluorescence intensity decreased as BRCA1 concentration rose. A near-linear correlation was observed between the FAM/GeT-NSs ratio and BRCA1 concentration (**Figure 3.7D**). To demonstrate that the recovery of FAM fluorescence was due to DNA hybridization between the FAM-cDNA@GeT-NSs nanoprobe and the target BRCA1, rather than degradation of the FAM-cDNA primer in the probe, agarose gel electrophoresis was conducted before and after the application of the target ssDNA. The results indicated that the probe-BRCA1 complex group (FAM-cDNA@GeT-NSs+BRCA1, FAM-cDNA@GeT-NSs+b1misDNA) exhibited a significant increase in the number of base pairs compared to the individual target FAM-cDNA and BRCA1 DNA (FAM-cDNA approximately 12 bp, BRCA1 DNA approximately 22 bp), suggesting successful hybridization of the FAM-cDNA@GeT-NSs nanoprobe with the target DNA (**Figure 3.7E**). Additionally, we observed the appearance of two bands in FAM-cDNA@GeT-NSs+b1misDNA and FAM-cDNA@GeT-NSs+ncDNA, indicating that target DNA mismatches reduce the DNA hybridization rate. To further study the selectivity of this platform, a comparison of the fluorescence recovery responses of one or two base mismatched BRCA1 ssDNA, ncDNA, miRNA 21, and miRNA 150 was performed (**Figure 3.7F**). The response was significantly enhanced with increasing concentration of the base-matched BRCA1 DNA, while no obvious variation in the response with increasing concentrations of non-complementary DNA, miRNA 21, and miRNA 150 was observed.

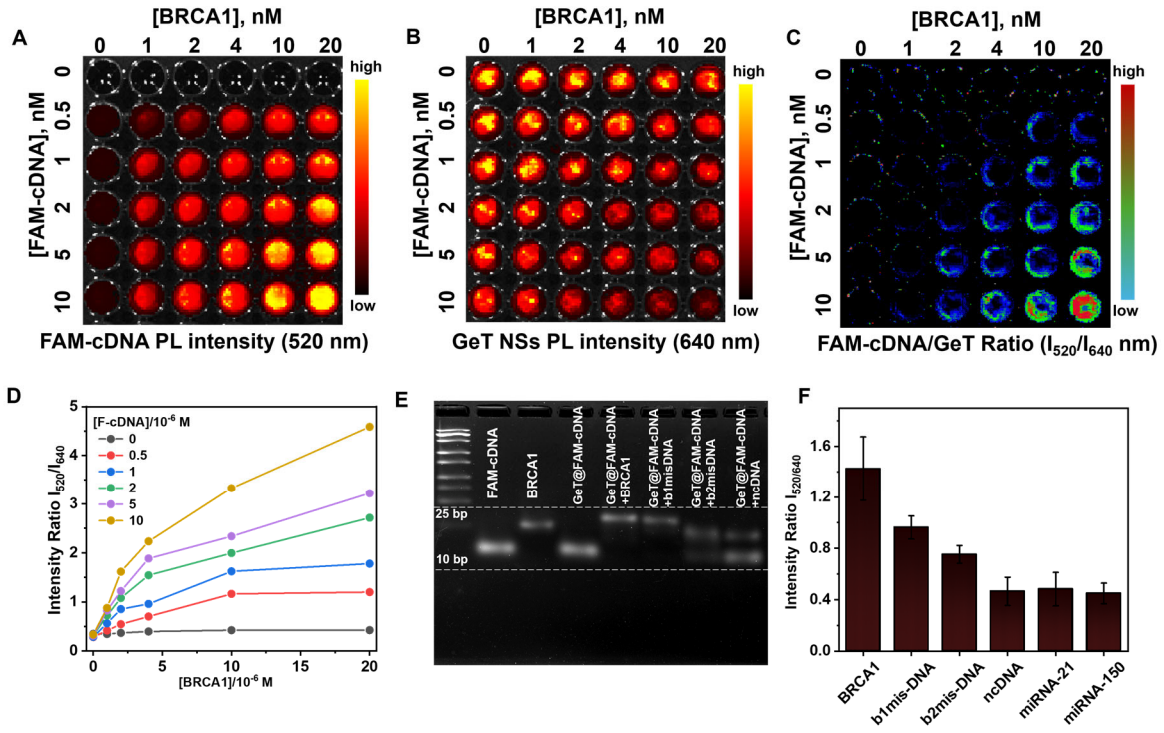

Figure 3.7 Pixel intensity maps of a multiwell plate containing increasing concentrations of BRCA1 (left to right) and FAM-cDNA (top to bottom) in 1X TE buffer (pH 7.4) and room temperature. After a 30 min incubation, the images were acquired using an IVIS with FAM (**A**, λ_{ex}= 480 ± 20 nm, λ_{em}= 520 ± 20 nm) or GeT-NSs (**B**, λ_{ex}= 480 ± 20 nm, λ_{em}= 620 ± 20 nm) channels. (C) Images of FAM-cDNA/GeT ratio for the multi-well plate. (D) A plot of FAM-cDNA /GeT ratio with different FAM-cDNA and BRCA1 concentrations. (E) Electrophoresis images (left to right: FAM-cDNA, BRCA1 ssDNA, GeT@FAM-cDNA, GeT@FAM-cDNA+BRCA1, GeT@FAM-cDNA+b1misDNA, GeT@FAM-cDNA+b2misDNA, and GeT@FAM-cDNA+ncDNA). (F) PL spectrum of FAM-cDNA@GeT-NSs after incubating with target BRCA1 ssDNA, b1misDNA, b2misDNA, ncDNA, miRNA-21, miRNA-150. The experiment was repeated three times, and the results are expressed as mean ± SD.

3.4 Summary

In this study, we have demonstrated a proof-of-concept for a novel biosensing platform exploiting 2D mGeNS. Our findings revealed that GeT-NSs serve as effective quenchers for FAM-cDNA, operating via the energy transfer mechanism and enabling ratiometric sensing. Notably, we applied this advanced material as a sensing platform to quantitatively and

selectively detect the BRCA1 gene DNA sequence based on the inner filter effect. The GeT-NSs@FAM-cDNA nanoprobe exhibited rapid detection of BRCA1 ssDNA without the need for amplification, achieving a lower LOD of 56 pM. Ongoing investigations may include exploring the sensing capabilities of GeT-NSs for BRCA1 miRNA, exploring the relationship between BRCA1 gene expression levels with T cells or breast cancer cells at different differentiation states, and refining the mechanistic understanding of the interaction between GeT-NSs and FAM-cDNA. Overall, this study elucidates the fluorescence quenching mechanism of GeT-NSs, which holds relevance for biosensors and medical applications.

Chapter 4: NIR-Triggered Germanene Nanosheet-Integrated Hydrogel-based Immunomodulator for Efficient Postoperative Cancer Immunotherapy

4.1 Introduction

Photothermal therapy (PTT), which hinges on photothermal reagents (PTAs) to convert light into heat and induce adequate hyperthermia for solid tumor ablation, has garnered significant attention in preclinical and clinical cancer treatment [228-230]. Advancements in NIR light-based PTAs have facilitated minimally invasive irradiation, drug resistance mitigation, and unnoticeable side effects in recent clinical trials, presenting a more favorable profile compared to conventional chemotherapy and radiotherapy [231-233]. Interestingly, recent research demonstrated that PTT could cause irreversible ICD of tumors, a process known as photothermal-triggered immunotherapy, providing a potential antigenic stimulation for the immune system [234, 235]. Leveraging the power of PTT, the DAMPs released from dying tumor cells can serve as "tumor-tailored vaccines" to enhance immunogenicity and trigger the regression of abscopal tumors [236-238]. Despite remarkable progress, successful clinical translation of this strategy is hindered by inadequate induction of ICD and the stress pathways involved in PTT-triggered ICD remain unclear [238-240]. Inadequate ICD induction observed in current PTAs can be attributed to their rapid degradation, resulting in limited tumor accumulation and retention, coupled with low photothermal conversion efficiency (PCE) [241, 242]. Conversely, despite some nanomaterials (e.g., gold nanoparticles) demonstrating stable photothermal performance, their limited biocompatibility and biodegradability impede clinical translation due to potential cytotoxic implications [243]. Therefore, the design and synthesis of new photothermal materials that combine robust photothermal conversion capabilities with favorable degradation kinetics are important to overcome these limitations and ensure the effective induction of ICD.

As one of the emerging 2D nanomaterials, germanene and its derivatives exhibit a larger-specific surface, outstanding biocompatibility, minimal cytotoxicity, and prominent

photothermal effects that have emerged as promising PTAs for tumor ablation [244-246]. While the applications of germanene hydride (GeH) and germanium phosphide (GeP) in PTT have been reported, extensive investigations into their application in PTI remain notably scarce [247-249]. The limited research may be attributed to the accelerated degradation kinetics of Ge-based nanosheets under physiological conditions (typically degrades around 24 ~ 48 h), significantly compromising the photothermal stability [250]. In addition, recent studies have shown that germanene exhibits a direct bandgap (~ 1.8 eV) and exceptional carrier mobility (~ 6×10^5 $cm^2V^{-1}s^{-1}$) after methylation [222, 251]. These properties minimize energy losses during photon absorption and facilitate the efficient generation of electron-hole pairs, giving a superior absorption coefficient and photothermal properties [252-255]. Consequently, we hypothesize that controlling the release kinetics of Ge-based nanosheets can prolong their localized retention and concentration at the lesion site, harnessing their distinctive photothermal conversion capability to achieve complete tumor eradication. Numerous investigations have demonstrated the ability of stimuli-responsive hydrogels to facilitate sustained localized drug release for various therapeutic applications including postoperative cancer management, bone regeneration, and skin repair [256, 257]. Notably, Ca^{2+} ion nano-chelated hydrogels could release Ca^{2+} upon degradation, thereby modulating intracellular Ca^{2+} ion homeostasis and effectively reversing tumor resistance mechanisms [258]. Consequently, the synergistic interplay between the hydrogel matrix and Ge nanosheets may enable precise regulation of Ge nanosheet release kinetics, thereby sustaining consistent PTT efficacy and eliciting a potent ICD response.

To validate the above hypothesis, we develop an **a**ccelerated **i**mmunomodulatory **m**atrix **r**eservoir, termed "AIMR", based on a biocompatible nanosheet integrated biodegrade hydrogel platform, to stimulate the accelerated production of *in situ* tumor vaccine for post-surgical immunotherapy. Briefly, we encapsulate polyvinylpyrrolidone (PVP)-modified and DOX-loaded mGe nanosheets (DOX-mGeNS@PVP) into a Ca^{2+} crosslinked sodium alginate hydrogel (SAgel) to construct the engineered reservoir (AIMR) (**Figure 4.1**). This immunomodulator was implanted into the tumor surgical bed and underwent an accelerated thermal breakage of the crosslinking and controlled release of DOX-mGeNS@PVP and Ca^{2+}

ions under the NIR light irradiation (980 nm). The AIMR immunomodulator solves the obstacles of easy degradation of mGeNS and simultaneously focuses on the two channels in the mitochondrial damage and the ER for tumor therapy. The therapeutic effect is markedly improved with the assistance of the Ca^{2+}-triggered mitochondrial dysfunction with a plenitude of adenosine triphosphate (ATP) released, upregulation of caspase-3, and subsequent cell apoptosis [259], [260]. mGeNS@PVP-induced hyperthermia triggers ER stress, inhibiting protein synthesis mediated by eIF2α phosphorylation, leading to calreticulin (CRT) exposure [261, 262]. We demonstrated that this "AIMR" platform could enrich the tumor-infiltrating of cytotoxic T cells, thereby efficiently eradicating solid tumors and initiating a self-perpetuating long-term "immune cycle". Besides, a strong “abscopal effect” in distant untreated tumors was observed. Taken together, we resolved the previous impasse of insufficient antigen presentation and ICD induction during PTT progress caused by the rapid degradation of germanene-based 2D nanomaterials. In addition, we integrated Ca^{2+}-triggered mitochondrial dysfunction and rapid release of DOX-mGeNS@PVP for ER stress and DNA cleavage, employing a multi-pronged approach to maximize ICD efficiency. Overall, our reported “AIMR” system sheds some light on the employment of hydrogel-based reservoirs and paves the way for mGeNS-like smart PTAs in biomedical research and personalized biomedicine.

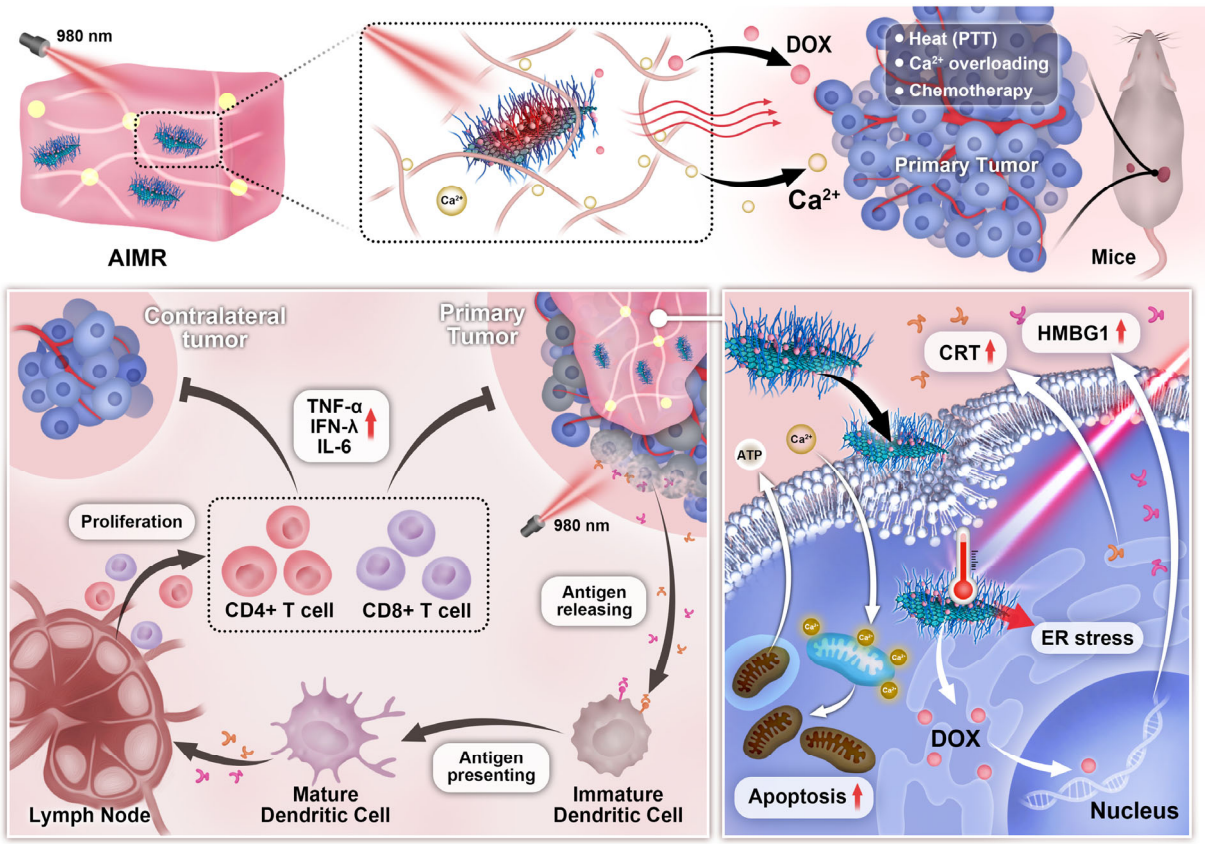

Figure 4.1 Schematic illustration depicting the light-controlled release Ca^{2+} and DOX-mGeNS@PVP of AIMR for preventing cancer postoperative recurrence and metastases.

4.2 Methods

4.2.1 Preparation and Characterizations of DOX-mGeNS@PVP

Synthesis of mGeNS. The mGe bulk powder (30 mg) was finely ground and subsequently added to an NMP solution (30 mL). The mGe bulk solution was subjected to probe sonication for 10 h in an ice bath to achieve exfoliation. After exfoliation, the solution was centrifuged at 3000 rpm for 20 min to separate the supernatant. The supernatant solution was carefully transferred to a new tube and centrifuged again at 4500 rpm for 10 min to collect the sediment (mGeNS) and stored at 4 °C for use.

Synthesis of mGeNS@PVP. Briefly, the PVP (10 mg, MW, 4000-6000) was dispersed in ethanol (1 mL), while mGeNS (1 mg) was dispersed in IPA (0.8 mL). Subsequently, 200 μL of a 10 mg mL^{-1} PVP solution was added to the mGeNS solution. The resulting mixture was

sonicated in an ice bath for 30 min and then stirred for 6 h at room temperature. Excess PVP was removed by centrifugation at 12000 rpm for 30 min. The obtained mGeNS@PVP solid was stored at 4 °C for further use.

Preparation of DOX-mGeNS@PVP. The DOX was loaded onto mGeNS@PVP under weakly alkaline conditions in ethanol. Briefly, mGeNS@PVP (1 mg) was mixed with doxorubicin hydrochloride (DOX·HCl, 2 mg) in ethanol (2 mL). Subsequently, 8 μL of NaOH aqueous solution (20 mg mL^{-1}) was added. The mixture was stirred in the dark overnight to obtain DOX-mGeNS@PVP. The products were centrifuged at 9000 rpm for 5 min and washed with DI water several times to remove any unloaded drugs. The loading efficiency (LE%) of DOX was determined using a previously established method. The LE% of DOX-mGeNS@PVP was calculated using Equation (1), as described below:

$$LE\% = Weigh\ of\ dox\ in\ the \frac{nanosheets(mg)}{innital\ solution\ (mg)} \times 100\% \quad (1)$$

4.2.2 Preparation and Characterizations of AIMR

1 mg DOX-mGeNS@PVP solution was dispersed in 1 mL PBS (pH 5.5 or 7.4) and placed in a dialysis bag (MWCO, 1k) and incubated at room temperature and 37 °C at 500 rpm with shaking. The solution was irradiated with a 980 nm laser with 1.0 W cm^{-2} for 10 min at each sampling time, respectively, and then replaced 0.2 mL of the drug-releasing PBS buffer with fresh 0.2 mL of PBS. The amount of DOX released from DOX-mGeNS@PVP at each sampling interval was quantified by comparison with a calibration curve of fluorescence intensity versus DOX concentration in PBS solution. Calculate the cumulative release drug percentage of each sampling point according to Equation (2):

$$Cumelative\ drug\ relase\ (\%) = \frac{Weight\ of\ drug\ released\ (mg)}{Weight\ of\ drug\ in\ the\ nanosheet\ (mg)} \times 100\%\ (2)$$

4.2.3 *In Vitro* Drug Release Analysis

DOX-mGeNS@PVP (1 mg) was dispersed in 1 mL PBS (pH 5.5 or 7.4) and placed in a dialysis bag (MWCO, 1k) and incubated at room temperature and 37 °C at 500 rpm with shaking. The solution was irradiated with a 980 nm laser at a power density of 1.0 W cm^{-2} for

10 min, respectively, and then replaced the drug-releasing PBS buffer (200 μL) with fresh PBS (200 μL). The amount of DOX released from DOX-mGeNS@PVP at each sampling interval was quantified by comparison with a calibration curve of fluorescence intensity versus DOX concentration in PBS solution. Calculate the cumulative release drug percentage of each sampling point according to Equation (2):

$$Cumelative\ drug\ relase\ (\%) = \frac{Weight\ of\ drug\ released\ (mg)}{Weight\ of\ drug\ in\ the\ nanosheet\ (mg)} \times 100\% \quad (2)$$

4.2.4 *In Vitro* Photothermal Effect

For measurement of the photothermal performance, mGeNS@PVP suspended in DI water with different concentrations (0, 50, 100, 150, and 200 μg mL^{-1}) were irradiated by an NIR laser (980 nm, 1.0 W cm^{-2}, 10 min). In addition, mGeNS@PVP (100 μg mL^{-1}) was exposed to a NIR laser with various power densities (0.5, 1.0, 1.5, and 2.0 W cm^{-2}, 980 nm, 10 min). The temperature was recorded by infrared thermal imager (FLIR C5) every 1 min. Furthermore, the photothermal stability of mGeNS@PVP at a concentration of 100 μg mL^{-1} was also measured. The mGeNS@PVP was irradiated by a 980 nm laser (1.0 W cm^{-2}) until the temperature reached the maximum, and then the temperature of the solution gradually decreased to room temperature. The cycle of heating and cooling was repeated three times. The photothermal conversion efficiency (η) of mGeNS@PVP was calculated based on the above temperature changes and according to the previous method [263, 264]. Detailed calculations were given as following Equation (4):

$$\eta = \frac{hS(T_{max} - T_{surr}) - Q_{Dis}}{I\left(1 - 10^{-A980}\right)} \quad (3)$$

Where h is the heat transfer coefficient, S is the surface area of the container. The maximum steady temperature (T_{max}) of the solution of the mGeNS@PVP was 55.4 °C and the environmental temperature (T_{Surr}) was 24.9 °C. Q_{Dis} represents the heat dissipated from light absorbed by the quartz sample cell itself, and it was measured independently to be 31.4 mW. The laser power I is 1.0 W, and A_{980} (0.507) is the absorbance of the nanosheets at the wavelength of 980 nm.

In Equation (4), hS is unknown for calculation. Therefore, we herein introduce sample system time constant (τ_s) and a dimensionless driving force temperature θ.

$$\tau_S = \frac{\Sigma_i m_i C_{p,i}}{hS} \quad (4)$$

$$\theta = \frac{T - T_{surr}}{T_{max} - T_{surr}} \quad (5)$$

where m_i is mass and $C_{p,i}$ is specific heat capacity

According to energy conservation law, Equation (6) could be changed to

$$\frac{d\theta}{dt} = \frac{1}{\tau_s}\left[\frac{Q_{laser}}{hS(T_{max} - T_{surr})} - \theta\right] \quad (6)$$

when the light source is shut off, the Q_{laser} is 0 at the cooling stage of the aqueous dispersion, therefore, Equation (8) can be expressed as

$$dt = -\tau_s \frac{d\theta}{\theta} \quad (7)$$

and integrating, giving the expression of Equation 8,

$$t = -\tau_s ln\theta \quad (8)$$

The constant of heat transfer from the system was determined to be τ_s =246 s of 980 nm according to the linear time data from the cooling period time. In addition, the m_i was 0.2 g, and the $C_{p,i}$ was 4.2 J g^{-1} K^{-1}. hS is deduced to be 5.25 mW K^{-1}. Finally, the η was calculated to be 60.6% according to Equation (3).

4.2.5 *In Vitro* Cytotoxicity Test

The murine melanoma cell line (B16F10) was originally from ATCC and cultured in complete RPMI 1640 (supplemented with 10% fetal bovine serum, 1% penicillin, and 1% streptomycin). The cells were seeded on 96 well plates (1×10^4 cells/well) and incubated in a humidified incubator at 37 °C with 5% CO_2. The cells were treated with mGeNS@PVP, mGePVP@SAgel, and AIMR with or without laser irradiation. The cell viability of B16F10 cells was evaluated through a CCK-8 kit (Dojindo, Japan) after treatment for 24 h.

Meanwhile, we investigated the live/dead cell viability of six hydrogel treatment groups (G1: Ctrl+L, G2: SAgel, G3: DOX@SAgel, G4: AIMR, G5: mGePVP@SAgel +L, G6: AIMR +L). In brief, the B16F10 cells (5×10^6 cells/well) were seeded on a confocal dish and co-stained with

10 μg mL^{-1} calcein-AM and PI (Thermofisher, USA) for 10 min after various treatments. The cell imaging was observed and captured by a confocal microscope (Leica TCS SPE). The cell apoptosis assay was determined by flow cytometry according to the protocol of the cell apoptosis kit (Beyotime Biotechnology, China). JC-1 mitochondrial membrane potential detection kit (Beyotime Biotechnology, China) was used to investigate the morphology and mitochondrial membrane potential. Fluo-2 AM (Abcam, UK) was used to measure the intracellular calcium concentration.

4.2.6 *In Vitro* BMDCs Maturation and Differentiation

A Trans well plate (Corning, USA) coculture system was constructed to explore the activation and maturation of bone marrow-derived dendritic cells BMDCs. The immature BMDCs were collected from mouse bone marrow and cultured in RPMI 1640 complete medium supplemented with 20 ng mL^{-1} GM-CSF (PeproTech, USA). The B16F10 cells and the DCs were cultured in the upper layer and the lower layer, respectively. This coculture system received six treatments, including Ctrl+L, SAgel, DOX@SAgel, AIMR, mGePVP@SAgel +L, and AIMR+L, respectively. After various treatments for 24 h, BMDCs in all groups were collected. And stained with antibodies of PE anti-mouse CD11c (1:200, Biolegend, #117307), APC anti-mouse CD86 (1:200, Biolegend, # 159215), and FITC anti-mouse CD80 (1:200, Biolegend, #104705), and then matured DCs were analyzed by flow cytometry (BD Accuri C6 Flow Cytometer). Meanwhile, the culture medium in the trans well system was also collected for the measurement of proinflammatory cytokines IFN-γ, TNF-α, and IL-6 with cytokine ELISA assay (Biolegend, USA).

4.2.7 Hemolysis Assay

The blood of mice was centrifuged (4000 rpm, 4 °C, 5 min) and resuspended in PBS to collect sediment (red blood cells, RBCs, 8%). The RBCs (100 μL) were distributed to six tubes and mixed with PBS (900 μL, negative control), double-distilled water (ddH_2O, 900 μL, positive control), and different concentrations of DOX-mGeNS@PVP in PBS respectively. After 6 h

incubation at 37 °C, 100 μL supernatant was taken out carefully to detect the absorbance at 540 nm via a UV-Vis spectrophotometer. The formula for hemolysis rate calculating was shown as following Equation (9):

$$Hemolysis\ (\%) = \frac{A_{sample} - A_{negative}}{A_{positive} - A_{negative}} \times 100\% \quad (9)$$

4.2.8 Characterization of Immunologic Cell Death

The B16F10 Cells were cultivated in confocal chambers, followed by the incubation of PBS, Ctrl+L, SAgel, DOX@SAgel, mGePVP@SAgel, mGePVP@SAgel +L, and AIMR+L for 24 h at 37 °C. Followed by washing with 1 M PBS, the cells were either kept in the dark or exposed to 980 nm light (1.0 W cm^{-2}) for 10 min. After 12 h of irradiation, the cells were fixed with 4% paraformaldehyde in ice for 20 min and then incubated with an anti-rabbit CRT antibody (1:100, Invitrogen, #PA3-900) or anti-rabbit HMBG1 antibody (1:100, Invitrogen, #PA1-16926) for 4 °C overnight. Then, the cells were further incubated with Donkey Anti-Rabbit IgG H&L (FITC) (1:1000, Invitrogen, #A16024) or Donkey Anti-Rabbit IgG H&L Alexa fluor 647 (1:1000, Invitrogen, #A31573) for another 90 min at room temperature, and cell nuclei were stained by DAPI. The cells were imaged under a confocal microscope to detect the CRT exposure and HMBG1 release. The CRT exposure and HMBG1 release were further detected by flow cytometry. To detect extracellular ATP, culture supernatants were collected and centrifuged at 12000 g at 4 °C for 10 min. The level of secreted ATP was quantified using an ATP bioluminescent assay kit (Beyotime, China) according to the instructions of the product.

4.2.9 Western Blot

Following completion of the different treatments for each setting, total protein was extracted by lysing cells with 0.5 ml of cell lysis buffer containing 1% protease inhibitor for 30 min on ice. The concentration of proteins in each group was then measured with the BCA assay kit and adjusted to 10 μg μl^{-1}. Then, proteins were heated with SDS-PAGE denaturing buffer at 95°C for 10 min. For the western blotting, the deformed protein was separated on 12% SDS-PAGE gel and then transferred to 0.45 μm nitrocellulose membranes. The membranes were blocked

with 1% BSA buffer for 1 h at room temperature before incubating with primary antibodies at 4 ℃ overnight. The dilution of primary antibodies (e.g., cytochrome c, cleaved-Caspase 3, ATF4, Phospho-eIF2α, and CHOP) was 1:1000, except 1:5000 of β-actin. Next, the membrane was incubated with horseradish peroxidase-conjugated secondary antibodies for 2 h at room temperature, then visualized using enhanced chemiluminescence reagents.

4.2.10 *In Vivo* Synergistic Therapy Evaluation

Female wide-type C57BL/6 mice (6-8 weeks old) were purchased from the Centralized Animals Facilities of the Hong Kong Polytechnic University. All animal procedures were carried out under the guidelines approved by the Hong Kong Polytechnic University Animal Study Committee and the Hong Kong Code of Practice for the care and use of animals for experimental purposes (approval number: 23-24/923-BME-R-PPR). A female C57BL/6 mouse (n=5 mice per group) tumor model was established by subcutaneous injection of 200 μL 5×10^6 B16F10-Luc cells. At about 9 d, when the tumor volume of the mouse reached 100 mm^3, 80% of the tumor in the mouse was removed under anesthesia. At the same time, SAgel (50 μg mL^{-1} $CaCl_2$, 100 μL SA solution), DOX@SAgel (8 mg kg^{-1} DOX, 50 μg mL^{-1} $CaCl_2$, 100 μL SA solution), AIMR (8 mg kg^{-1} DOX-mGeNS@PVP , 50 μg mL^{-1} $CaCl_2$, 100 μL SA solution), mGePVP@SAgel +L (8 mg kg^{-1} mGeNS@PVP, 50 μg mL^{-1} $CaCl_2$, 100 μL SA solution, 980 nm laser, 1.0 W cm^{-2}), and AIMR+L (8 mg kg^{-1} DOX-mGeNS@PVP, 50 μg mL^{-1} $CaCl_2$, 100 μL SA solution, 980 nm laser, 1.0 W cm^{-2}), were patched into the tumor surgical bed, and the mouse wound was sutured with 5-0 absorbable suture. The only surgery group was the control group. Photothermal therapy of the NIR group was performed on Day 1, 3, and 7 after surgery with 1.0 W cm^{-2} 980 nm laser for 5 min, irradiated for another 5 min after 2 h. The body weight and tumor volume were measured at two-day intervals and calculated by the following Equation (10):

$$tumor\ volume = \frac{(length \times width^2)}{2} \quad (10)$$

Tumor growth was monitored by *in vivo* imaging (perkin-elmer IVIS) after treatment. After 25 d of treatment, the mice were sacrificed, and the blood, tumor tissues, spleens, lymph nodes,

and main organs were collected. The paraffin sections of organs were prepared for H&E staining to evaluate the histocompatibility. The paraffin sections of tumors were prepared for H&E staining (H&E Staining Kit, Abcam, #ab245880) and TUNEL staining (One-step TUNEL In Situ Apoptosis Kit, Elabscience, #E-CK-A320) to evaluate the apoptosis. For cytokine detection (TNF-α, IL-6, and IFN-γ), serum samples in all groups were collected from mice on Day 7, 10, and 13 after various treatments and analyzed with ELISA kits (BioLegend). The lymphocytes in spleens were determined by flow cytometry PE-antimouse-CD4 (1:100, Elabscience, E-AB-F1013E), FITC-antimouse-CD8a (1:100, Elabscience, E-AB-F1104C), Percp cy5.5-antimouse-CD3 (1:100, Elabscience, E-AB-F1013UJ), CD62-antimouse-PE (1:100, Elabscience, E-AB-F1011D), anti CD44-antimouse-APC (1:100, Elabscience, E-AB-F1100UE). For analyzing DCs in lymph nodes, cells were stained by PE anti-mouse CD11c (1:200, Biolegend, #117307), APC anti-mouse CD86 (1:200, Biolegend, # 159215), and FITC anti-mouse CD80 (1:200, Biolegend, #104705). The DCs mature assay was processed by flow cytometry, and the data were analyzed by FlowJo software.

4.2.11 *In Vivo* Tumor Rechallenge Study

The bilateral B16F10 tumor model was established to evaluate the abscopal effect, wherein B16F10 cells (1×10^6 per mouse) were inoculated in the left flank of the C57BL/6 mice subcutaneously to establish primary tumors for different therapy treatments. Five days later, B16F10 cells (5×10^5 per mouse) were inoculated in the right flank of the mice subcutaneously to establish the distant tumor without any treatment for imitating cancer metastasis. Subsequently, the mice with bilateral B16F10 tumor were randomized into 6 groups (n=5 mice per group) as follows: Surgery, SAgel (50 μg mL^{-1} $CaCl_2$, 100 μL SA solution), DOX@SAgel (8 mg kg^{-1} DOX, 50 μg mL^{-1} $CaCl_2$, 100 μL SA solution), AIMR (8 mg kg^{-1} DOX-mGeNS@PVP , 50 μg mL^{-1} $CaCl_2$, 100 μL SA solution), mGePVP@SAgel +L (8 mg kg^{-1} mGeNS@PVP, 50 μg mL^{-1} $CaCl_2$, 100 μL SA solution, 980 nm laser, 1.0 W cm^{-2}), and AIMR+L (8 mg kg^{-1} DOX-mGeNS@PVP, 50 μg mL^{-1} $CaCl_2$, 100 μL SA solution, 980 nm laser, 1.0 W cm^{-2}), respectively. On Day 1, 3, and 7, only the primary tumor was exposed to 980 nm

irradiation (1.0 W cm^{-2}, 5 min) twice time (interval: 2 h) at 24 h post each intravenous administration of different hydrogel formulations. Then, the volumes of primary tumors and distant tumors were monitored.

4.2.12 Statistical Analysis

All the animal studies were performed after randomization. Quantitative data were collected at least three times. All the data were analyzed by Origin 2021 and GraphPad Prism 9.0. All the values were reported as mean ± SD. The differences among the groups were compared with a one-way ANOVA analysis. ns: no significance, *p< 0.05, **p< 0.01, ***p< 0.001, n= 3.

4.3 Results and Discussion

4.3.1 Characterization, and Photothermal Properties of mGeNS@PVP

This study employed mGeNS as the photothermal agent due to their superior thermal stability and antioxidant properties in aqueous solutions compared to GeH [222]. We started with synthesizing mGeNS via a liquid-phase exfoliation of bulk mGe into mGeNS, followed by surface modification with polyvinylpyrrolidone (PVP, MW= 4000-6000) through hydrophobic interactions to enhance their (mGeNS@PVP) aqueous dispersibility and colloidal stability (**Figure 4.2A**). Scanning electron microscopy (SEM) analysis revealed that bulk Ge exhibited well-stacked and laminated microstructure, while mGeNS and mGeNS@PVP showed sheet-like morphology with ~ 300 nm and ~ 400 nm, respectively (**Figure 4.2B-D**). Consistently, their hydrodynamic diameters were 310 ± 9.5 nm and 423 ± 12.9 nm, respectively (**Figure 4.2E**). Atomic force microscope (AFM) analysis demonstrated that the thickness of mGeNS and mGeNS@PVP were ~ 3.2 nm and ~ 7.5 nm (**Figure 4.2F, G**).

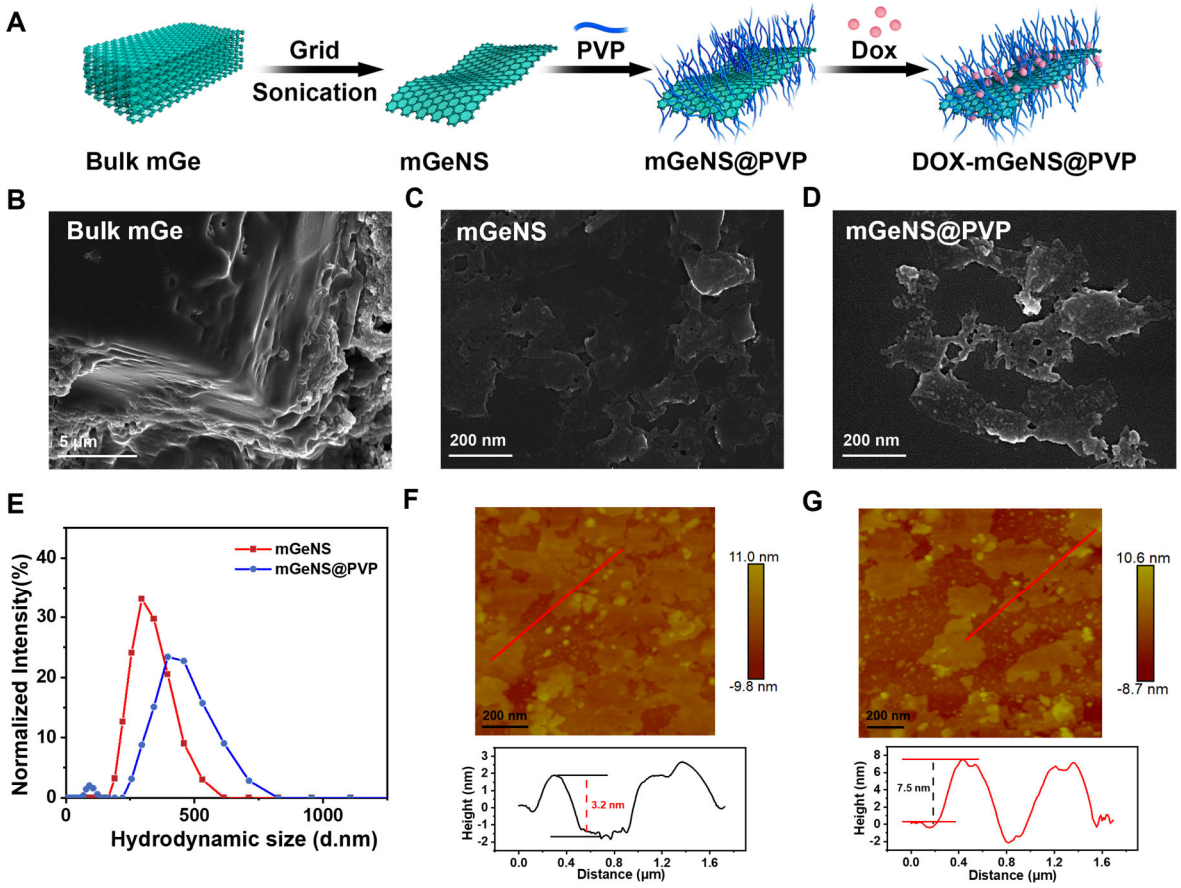

Figure 4.2 Characterization of the mGeNS and mGeNS@PVP. (A) Preparation routes of mGe-based nanosheet as drug carrier. SEM images of (B) Bulk mGe, (C) mGeNS, and (D) mGeNS@PVP. (E) DLS spectrum of mGeNS and mGeNS@PVP. AFM image and the height profiles of (F) mGeNS and (G) mGeNS@PVP .

Although XRD peaks of mGeNS showed features of germanene (**Figure 4.3A**), its Raman characteristic peaks slightly redshifted with ~ 4 nm (**Figure 4.3B**), indicating the scaling down from bulk mGe to mGeNS [265]. Moreover, FTIR spectrum indicated the new peak at 1648 cm^{-1} responsible for C=O stretching vibration indicating the successful PVP modification [265] (**Figure 4.3C**). X-ray photoelectron spectroscopy (XPS) confirmed the surface element composition and reference binding energy of Ge3d ($3d_{5/2}$, 30.76 eV and $3d_{3/2}$, 31.47 eV) in mGeNS and mGeNS@PVP (**Figure 4.3D, E**). Note that mGeNS showed strong intensity at 32.16 eV (GeO) and 33.53 eV for (GeO_2), which were much weaker in mGeNS@PVP. This data reveals that PVP coating reduces this oxidation-mediated influence of mGeNS [266].

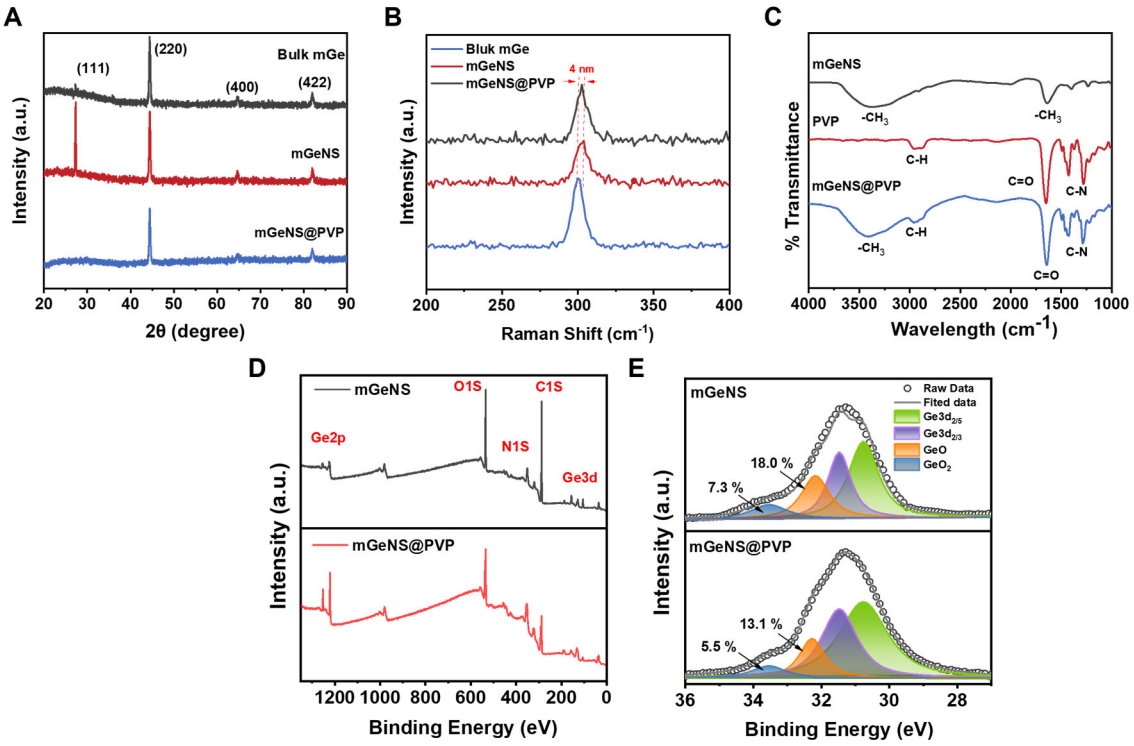

Figure 4.3 Characterization of the mGeNS, and mGeNS@PVP. XRD spectrum (A), Raman spectrum (B) and FTIR spectrum (C) of Bulk mGe, mGeNS, and mGeNS@PVP. Wide-scan (D) and high-resolution XPS spectrum (E) of mGeNS and mGeNS@PVP ($Ge3d_{2/5}$, $Ge3d_{2/3}$, GeO, and GeO_2).

Next, we assessed the photothermal response of mGeNS. First, it showed enhanced NIR region absorbance that elevated with increased concentrations (**Figure 4.4A**). By Beer-Lambert law, the calculated extinction coefficient (ε) of mGeNS at 980 nm was 7.52 $Lg^{-1}cm^{-1}$, which is much higher than that of some typical PTAs, such as graphene oxide nanosheets (GO, 3.6 L g^{-1} cm^{-1}) [267], gold nanorods (3.9 L g^{-1} cm^{-1}) [268] (**Figure 4.4B**). Hence, mGeNS@PVP demonstrated concentration-dependent photothermal conversion, ranging from 0 to 200 μg mL^{-1} under 980 nm NIR irradiation (**Figure 4.4C, D**). Strikingly, only 100 μg·mL^{-1} of mGeNS@PVP illustrated a remarkable temperature increase (25.1 to 55.8°C, ΔT = 30.7 °C) after 1.0 W·cm^{-2} 980 nm laser irradiation within 10 min but little temperature fluctuation of water (ΔT = 7.6 °C). Also, the photothermal response of mGeNS@PVP was laser power density dependent, testing from 0.5 to 2.0 W cm^{-2} that showed a higher temperature rise with increased

power density (**Figure 4.4E**). Notably, the mGeNS@PVP demonstrated a stable photothermal capability over 3 cycles of NIR laser on (10 min) and off (cooled down to room temperature) (**Figure 4.4F**). Based on the total energy balance of this system, the calculated PCE of mGeNS@PVP is 60.6% (**Figure 4.4G, H**), which is 14.7% higher than GeNS only [248], highlighting the importance of PVP protection. In short, these results confirm the successful fabrication of Ge-based nanosheets with efficient PCE.

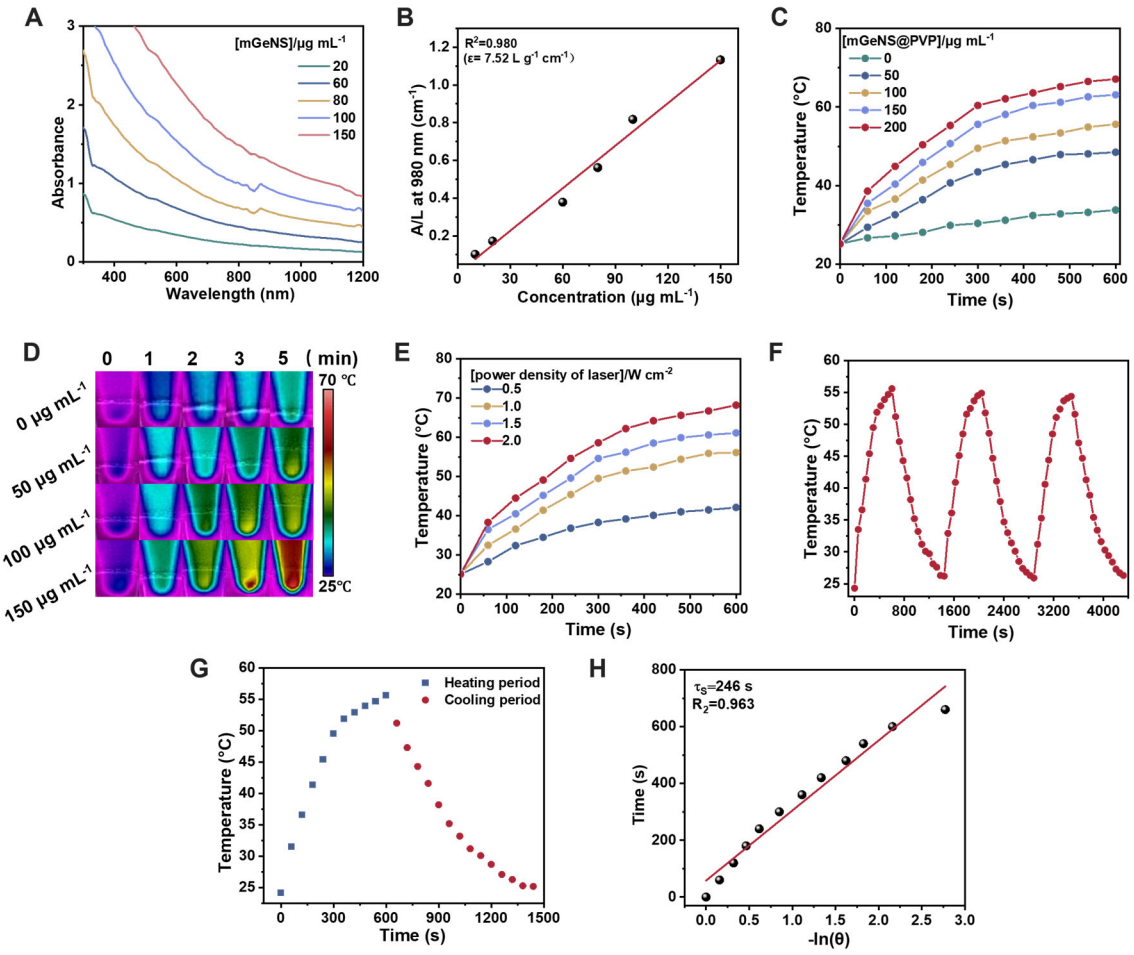

Figure 4.4 Photothermal properties of mGeNS. (A) UV-vis-NIR spectrum of mGeNS dispersions with different concentrations. (B) Fitting curve of extinction coefficient of mGeNS at 980 nm, the extinction coefficient was calculated from the slope of the concentration vs absorbance according to the equation of A = εbc, where A is the absorbance, ε is the molar extinction coefficient, b is the path length of the cuvette. (C) Temperature variation of different concentrations of mGeNS@PVP under the 980 nm laser irradiation at 1.0 W cm^{-2}. (D) Corresponding infrared thermal images for different concentrations of mGeNS@PVP at different

periods (0, 1, 2, 3, and 5 min). (E) Photothermal heating curves of 100 μg mL^{-1} mGeNS@PVP upon the radiation of different power densities (0.5, 1.0, 1.5, and 2.0 W cm^{-2}) of 980 nm laser. (F) Temperature variation of 100 μg mL^{-1} mGeNS@PVP under the irradiation at 1.0 W cm^{-2} for 3 on/off cycles (10 min irradiation for each cycle). (G) Photothermal curves of mGeNS@PVP during irradiation for 10 min and cooling to room temperature. (H) The linear time constant was calculated from the cooling period.

Before hydrogel encapsulation, DOX was adsorbed onto mGeNS@PVP (DOX-mGeNS@PVP) through hydrophobic interaction for *in situ* NIR-triggered chemotherapy. The emergence of an absorption peak at ~ 500 nm in DOX-mGeNS@PVP indicates the characteristic peak of DOX [269, 270] (**Figure 4.5A**). After DOX loading, its zeta potential increased from -3.25 mV to 7.10 mV (**Figure 4.5B**), indicating strong electrostatic interaction between DOX and mGeNS@PVP. Meanwhile, the hydrodynamic size of DOX-mGeNS@PVP was similar to that of mGeNS@PVP (**Figure 4.5C**). Importantly, the highest drug loading efficiency of DOX was 107 wt% (**Figure 4.5D**), demonstrating that mGeNS provided a large surface area for drug adsorption [270]. DOX release from DOX-mGeNS@PVP was minimal (only ~ 20%) over 30 h at pH 7.4 and 37 ºC, indicating that this stable adsorption reduced non-specific drug release. We showed that the boosting of DOX release was highly dependent on different pH values and/or temperatures (**Figure 4.5E, F)**. For instance, pH 5.5 and a 10-min NIR laser excitation (reached the temperature at 55.7 ºC) facilitated the drug release with 39.4 ± 2.3% and 78.6 ± 3.1% over 30 h. These findings prove the possibility of photo-triggered chemotherapy by the Ge-based nanocomplexes.

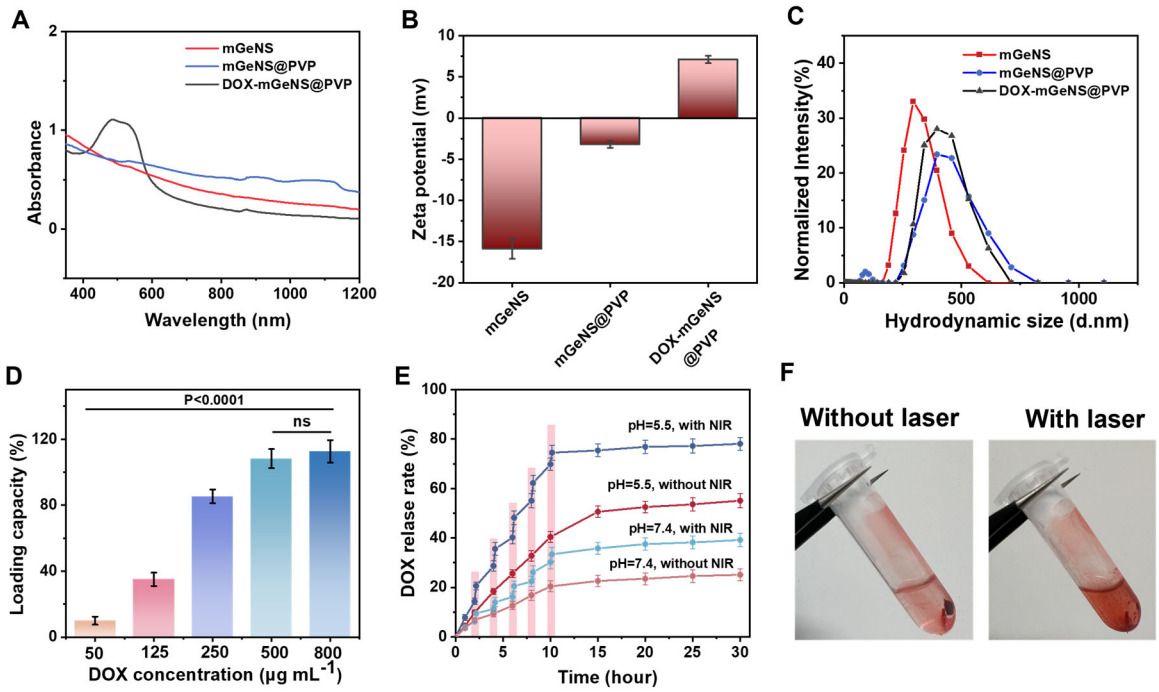

Figure 4.5 Characterization and drug loading performance of DOX-mGeNS@PVP. (A) UV-Vis-NIR spectrum, (B) Zeta potential, and (C) DLS spectrum of mGeNS, and mGeNS@PVP and DOX-mGeNS@PVP, respectively. (D) DOX loading capacity of DOX-mGeNS@PVP when the DOX concentration was 50, 125, 250, 500, and 800 μg mL $^{-1}$, respectively. (E) DOX release from DOX-mGeNS@PVP at pH 5.5 or 7.4 buffer and 37 °C with or without 980 nm laser irradiation (1 W cm^{-2}). (F) photo of DOX-mGeNS@PVP with and without 980 nm laser.

The comparison of PCE, biodegradability, and cytotoxicity with other 2D nanosheets is shown in **Table 2**. These results demonstrated that the nanosheet in this work exhibits excellent PCE, biodegradability, and low biotoxicity, suggesting their potential as an outstanding photothermal agent.

Table 2 The PCE of different photothermal nanosheets. The three moods represent excellent, medium, and low biodegradability or toxicity.

Materials	Power of excitation light source	Biodegradability	PCE	Ref.
$MoTe_2$	808 nm laser (0.6 W cm^{-2})	😀	33.8%	[271]
CFMS-PVP NSs	808 nm (1.0 W cm^{-2})	☹	89.0%	[272, 273]
AsP NSs	1064 nm (1.0 W cm^{-2})	☹	37.6%	[170, 274]
$MoSe_2$ NSs	808 nm (2.5 W cm^{-2})	☹	57.9%	[275]
NbS_2-PVP NSs	808 nm (0.33 W cm^{-2}) 1064 nm (1.0 W cm^{-2})	☹	59.2%(808nm) 69.1%(1064nm)	[265, 276]
BP NSs	808 (1.0 W cm^{-2})	😀	32.5%	[277]
MoS_2 NSs	808 (1.0 W cm^{-2})	☹	24.4%	[278, 279]
Ta_2NiS_5-P NSs	808 (1.0 W cm^{-2})	😐	35.0%	[280], [281]
NYF@BP NSs	980 (0.7 W cm^{-2})	😐	30.8%	[282], [282]
GeP NSs	808 nm (1.0 W cm^{-2})	😀	68.6%	[283]
This work	980 nm (1.0 W cm^{-2})	😀	60.7%	

4.3.2 Characterization of AIMR Immunomodulator

To improve the prolonged residence time of DOX-mGeNS@PVP in the tumor microenvironment for extending the therapeutic duration, we encapsulated the nanosheet in the SAgel, forming AIMR. SEM analysis and Elemental mapping results revealed that mGeNS was entrapped within the Ca^{2+} crosslinked SAgel network (**Figure 4.6A, B**). In particular, mGeNS alone spontaneously degraded and its solution turned from brown color to half translucent in aqueous solution after 48 h of incubation, further confirmed by decreased absorbance of the

UV-vis spectrum (**Figure 4.6C**). In contrast, the as-prepared AIMR prevented the degradation of mGeNS@PVP with a stable absorption intensity over an extended period (>10 d) with intact nanosheet structures (**Figure 4.6D**), indicating the importance of hydrogel protection from degradation of DOX-mGeNS@PVP in the aqueous phase. Next, the rheological characterization of AIMR revealed storage modulus (G') relative to the loss modulus (G") curves intersected at a shear strain of 0.31% higher than those in SAgel only, indicating that the nanocomposites *in situ* reinforced its mechanical properties (**Figure 4.6E)**. Similarly, the gel-to-sol transition temperature also increased from 42.8 °C to 43.9 °C after the addition of DOX-mGeNS@PVP (**Figure 4.6F**). These rheological features demonstrate the successful fabrication of this mGeNS/SAgel integrated platform. In addition, both DOX-mGeNS@PVP and its SAgel-encapsulated form (with or without DOX loading) exhibited very similar photothermal responses, suggesting little influence of PCE after hydrogel encapsulation (**Figure 4.6G, H)**. We also investigated the drug-released behavior of AIMR in PBS buffer (**Figure 4.6I)**. With the prolongation of the incubation time and upon NIR irradiation, a cumulative release of DOX from AIMR reaches approximately 60 wt% over 10 days, accompanied by a 62% reduction in weight. Such a photothermal responsive degradation profile of SAgel guarantees the photo-controlled drug release from AIMR in TME.

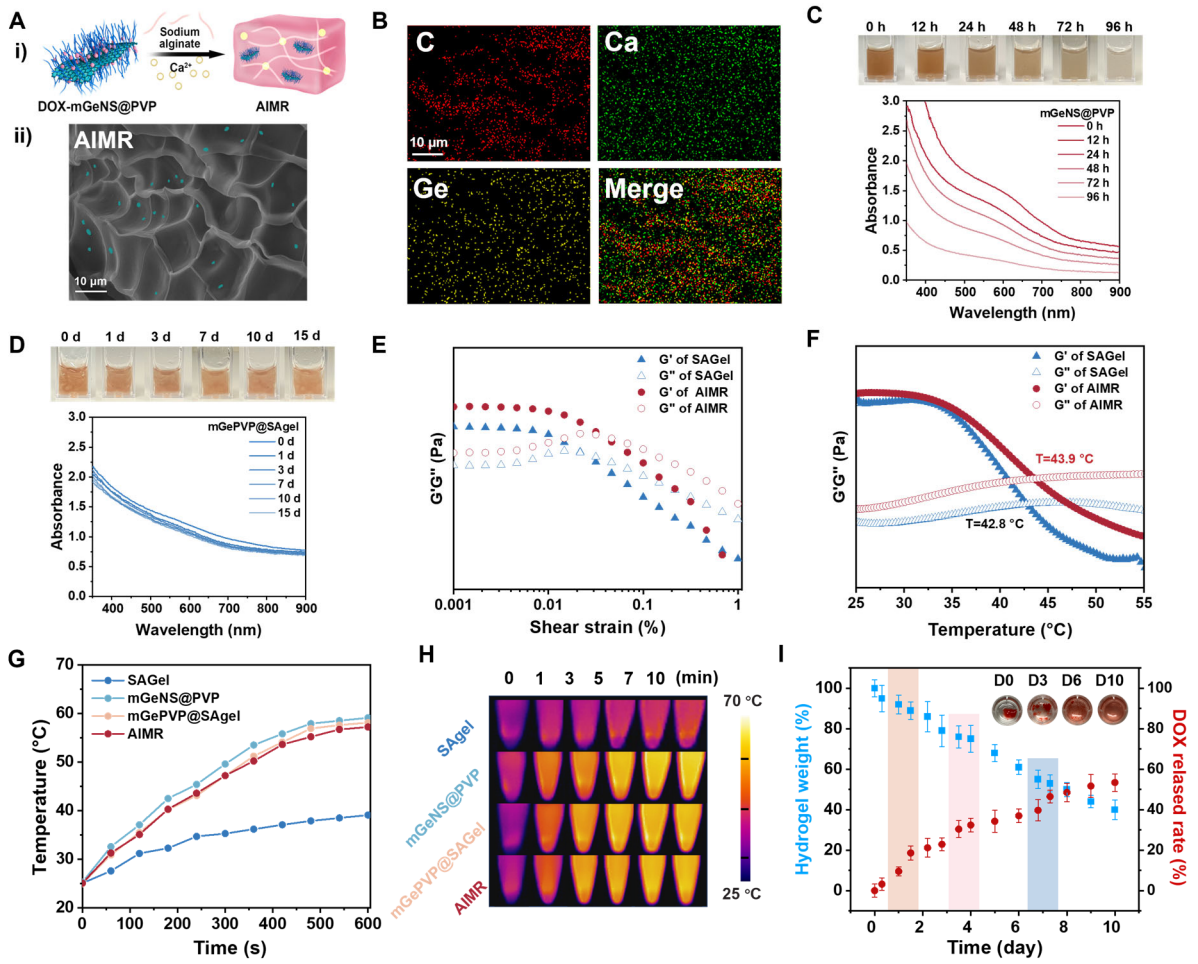

Figure 4.6 Characterization and PTT performance of the AIMR. (A) Preparation routes (i) and SEM image (ii) of AIMR. (B) Elemental mapping analysis of AIMR. The scale bar is 10 μm for all figures. UV-vis spectrum of (C) mGeNS@PVP and (D) mGePVP@SAgel in DI water at different time intervals. Inset: bright field photos of corresponding samples in cuvettes at different times. Variation of storage modulus (G') and loss modulus (G") versus (E) shear strain (%) at 25 °C and (F) temperature (25 to 55 °C, 1 rad/s, the heating rate is 1.5 °C min^{-1}) of the SAGel and AIMR. Photothermal heating curves (G) and corresponding infrared thermal images (H) for different periods (0, 1, 3, 5, 7, and 10 min) of SAgel, mGeNS@PVP, mGePVP@SAgel, and AIMR upon the NIR radiation (1.0 W cm^{-2}, 980 nm). (I) Hydrogel weight and DOX release rate of mGePVP@SAgel under the 980 nm laser irradiation (1 W cm^{-2}). The highlighted area indicates the period of laser irradiation.

4.3.3 *In Vitro* Tumor Elimination Effect of AIMR

We evaluated the *in vitro* cytotoxicity of mGeNS@PVP without DOX loading and NIR in B16F10 tumor cell lines. Notably, more than 90% of cells survived up to 200 μg mL^{-1} after 24 h of incubation, confirming good biocompatibility of mGeNS@PVP (**Figure 4.7A**). We also showed that incubating AIMR with RBCs with different concentrations of encapsulated DOX-mGeNS@PVP did not induce significant hemolysis, such as <7.8% hemolysis ratio at 500 μg mL^{-1} of the DOX-mGeNS@PVP (**Figure 4.7B**), indicating good hemocompatibility of our hydrogel platform. The hydrogel was injected into a monolayer of B16F10 cells cultured on a petri dish. As expected, Raman mapping of the *in vitro* result showed that a little intensity Raman peak of mGeNS or/and DOX at 298 cm^{-1} and 1340-1720 cm^{-1}, respectively, within single cells after 4 h of incubation (**Figure 4.7C, D)**, showing that most nanosheets were entrapped in the SAgel at the physiological condition. In contrast, a 10-min NIR irradiation induced robust cellular Raman signals of mGeNS or/and DOX in the mGeNS@PVP and DOX-mGeNS@PVP groups by a 36-fold increase, respectively (**Figure 4.7E**). Together, these results manifest that mGeNS@PVP is highly biocompatible and can be efficiently uptake for intracellular delivery of DOX once released from AIMR post-NIR stimulation.

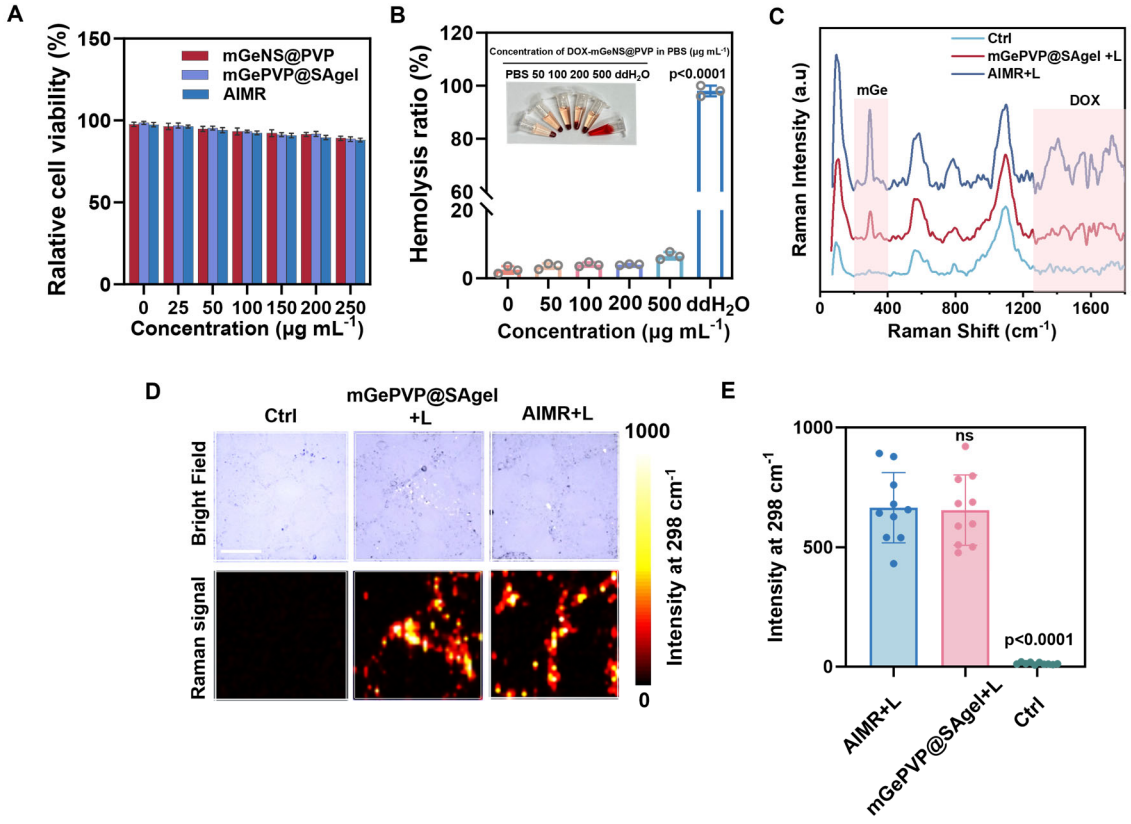

Figure 4.7 *In vitro* evaluation of cytotoxicity and cell uptake. (A) CCK-8 assay of B16F10 cell viability after treatment with different concentrations of mGeNS@PVP, mGePVP@SAgel, and AIMR for 24 h, respectively. (B) Hemolysis ratio of RBCs after 6 h incubation with DOX-mGeNS@PVP at different concentrations (from 0 to 500 μg mL-1). The inset shows the photograph of RBCs exposed to ddH2O and DOX-mGeNS@PVP with different concentrations followed by centrifugation. Raman spectrums (C) and corresponding Raman intensity maps (D) were collected from B16F10 cells after their incubation with PBS, mGeNS@PVP (100 μg mL-1) and DOX-mGeNS@PVP (100 μg mL-1) for 4 h, respectively. The scale bar is 50 μm for all figures. (E) Corresponding scattering dot diagrams for the Germanene-peak intensity. ns: no significance, data are presented as the mean with SD (n = 3 independent samples). Statistical differences were analyzed by a one-way ANOVA with Tukey's multiple comparisons test.

Next, we assess the effect of NIR-triggered synergistic cancer treatment of AIMR through live/dead cell assay. After NIR irradiation at 1.0 W cm^{-2} for 10 min, the cell viability was reduced by ~ 64% and 92% in mGePVP@SAgel+L or AIMR+L groups, respectively (**Figure 4.8A)**. The results demonstrated that only green fluorescence could be observed when SAgel,

DOX@SAgel, or AIMR without irradiation were used to incubate the B16F10 cells (**Figure 4.8B)**. These results were further evidenced by the Annexin V-FITC/PI flow cytometry results, revealing a 3-fold increase in late apoptosis in SAgel compared to the control group (**Figure 4.8C)**. In contrast, a small number of B16F10 cell deaths were observed in both the DOX@SAgel and AIMR groups. The mGePVP@SAgel plus laser group caused a moderate number of B16F10 cell deaths, while the AIMR plus laser group caused the majority of cell deaths. Similarly, the percentage of apoptotic cells (including early and late apoptotic cells) induced by AIMR reached 76.9% upon NIR irradiation, showing a remarkable synergistic therapeutic efficacy (**Figure 4.8D**).

We elevated the ICD induction capability of AIMR by the generation of DAMPs, including CRT, ATP, and high mobility group box 1 (HMGB1). CRT serves as a distinctive biomarker of ICD, functioning as an 'eat me' signal when exposed on the membrane surface of tumor cells, thereby facilitating DC maturation and T-cell activation [284]. We discovered that incubating mGePVP@SAgel with AIMR for 4 h, followed by irradiation with a 980 nm NIR laser for 10 min, could most effectively enhance the surface exposure of CRT (**Figure 4.8E**). Similarly, the HMGB1 is a crucial ICD biomarker, primarily localized within the cell nucleus under normal physiological conditions [285], [286]. The AIMR plus NIR treatment exhibited a significant HMGB1 release from the nucleus compared to other control groups (**Figure 4.8F**). This result was consistent with the assessment of DOX release upon NIR irradiation, confirming that PTT promotes an increased internalization of DOX into the cell nucleus, leading to DNA repair and cell damage (**Figure 4.8H**) [287]. Compared with free DOX, the maximum intensity of DOX-mGeNS@PVP and AIMR upon NIR irradiation in cells increased by 39.6 and 35.8 times respectively, indicating that the PTT promotes DOX penetration (**Figure 4.8I)**. In addition, we observed that extracellular ATP levels of B16F10 cells in DOX-mGeNS@PVP and AIMR upon NIR irradiation group significantly increased, up to 6.25-fold and 20.2-fold, respectively, compared to the control group (**Figure 4.8G**). Our results strongly indicated that NIR-activated AIMR programmable enhances the release of DAMPs from B16F10 tumor cells, which could provide potential *in situ* "cancer vaccine" activation for antitumor immune response.

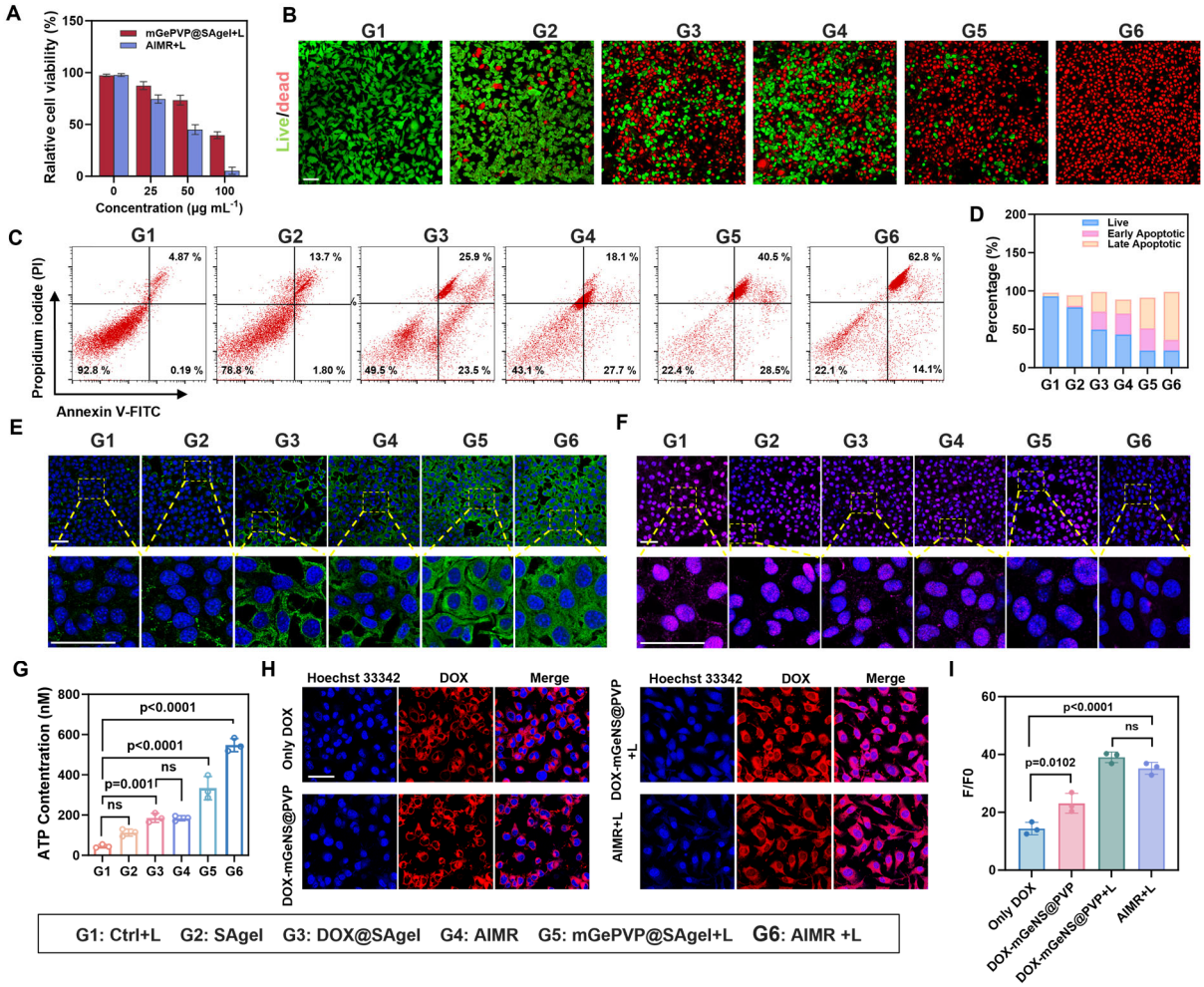

Figure 4.8 *In vitro* cell uptake, cytotoxicity, and DAMPs release evaluation. (A) Cell viability of B16F10 cells was evaluated 24 h after treatment with mGePVP@SAgel or AIMR followed by 980 nm laser irradiation (1 W cm^{-2}, 10 min). (B) CLSM images of B16F10 cells stained with calcein AM (AM= acetoxymethyl, green, living cells) and PI (podium iodide, red, dead cells) after different treatments with or without laser irradiation (980 nm, 1 W cm^{2}, 10 min). The scale bar is 50 μm for all figures. (C) Apoptosis was measured by flow cytometry through Annexin V-FITC and PI staining of B16F10 cells received different treatments. Early apoptotic cells (Annexin-V+ and PI-) are shown in the lower right quadrant, and late apoptotic cells (Annexin-V+ and PI+) are shown in the upper right quadrant. (D) Statistics analysis of cell apoptosis is shown in **C**. (E-F) CLSM images of B16F10 cells incubated with the specific CRT protein fluorescent probe (E, green) and HMBG1 protein fluorescent probe (F, purple) and DAPI (blue) upon the treatments with or without laser irradiation. The scale bar is 20 μm for all figures. (G) Quantification of extracellular ATP in B16F10 cells upon the treatments with or without laser irradiation. (H) B16F10 cells were treated with free DOX,

DOX-mGeNS@PVP, DOX-mGeNS@PVP plus Laser, and AIMR plus Laser, receptively, and then the CLSM images were observed. Cell nuclei were stained with Hoechst 33342 (blue). The scale bar is 50 μm for all figures. (I) The ratio intensity of other groups (F) and ctrl group (F0) was analyzed by flow cytometry. ns: no significance, data are presented as the mean with SD (n=3 independent samples). Statistical differences were analyzed by a one-way ANOVA with Tukey's multiple comparisons test.

4.3.4 *In Vitro* Immune-Activating Efficacy of AIMR

To further evaluate AIMR-induced immunogenicity of the tumor cells, we investigated ICD-induced bone marrow-derived dendritic cells (BMDCs) maturation *in vitro* using flow cytometry (**Figure 4.9A**). DCs play crucial roles in initiating adaptive immune responses [288]. We found that the frequency of mature DCs ($CD11c^+CD80^+CD86^+$) in AIMR plus laser (59.1%), was more efficient than SAgel (21.1%) and DOX@SAgel treatment (35.0%), further indicating the increased DCs-mediated immune activation (**Figure 4.9B, C**). To further corroborate the immunogenic potential of our platform, we investigated the secretion of key immune factors (interleukin 6 (IL-6), interferon-γ (IFN-γ), and tumor necrosis factor α (TNF-α)) through ELISA assay. IFN-γ and TNF-α are known to promote DC maturation, while IL-6 is a pleiotropic cytokine involved in immune responses, inflammation, and hematopoiesis [289], [290]. In our observation, B16F10 cells treated with AIMR under 980 nm laser irradiation exhibited upregulated expression of all these cytokines, providing strong support for the modulation of the immune system (**Figure 4.9D-F**).

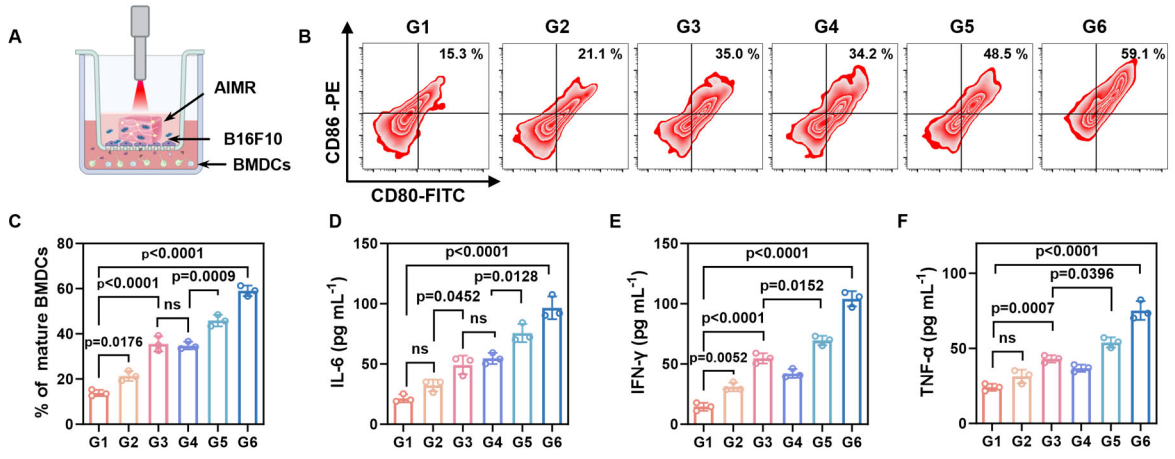

Figure 4.9 (A) Schematic illustration of Transwell model for BMDCs maturation. (B) BMDCs maturation

induced by various formulations, as evaluated by flow cytometry after costaining with CD80/CD86. (C) Quantification of the percentage of mature BMDCs after different treatments. (D-F) Statistical chart of IL-6, IFN-γ, and TNF-α cytokine levels in coculture supernatant secreted by BMDCs after different treatments for 48 h. The treatment groups are G1 (ctrl plus laser), G2 (SAgel), G3 (DOX@SAgel), G4 (AIMR), G5 (mGePVP@SAgel plus laser), and G6 (AIMR plus laser) for the above experiment. ns: no significance, data are presented as the mean with SD (n = 3 independent samples). The data were analyzed by one-way ANOVA with Tukey's multiple comparisons post-test.

We further evaluated the underlying therapeutic mechanism of AIMR to enhance ICD (**Figure 4.10A**). CLSM and SEM results revealed a significant morphological alteration of the ER, transitioning from a network structure to a swollen morphology (**Figure 4.10B, C**), indicative of heat stress-induced disruption of the normal protein folding process [291]. This ER damage is the primary contributing factor to the upregulation of the ER molecular chaperone CRT [292]. Upon extending the NIR irradiation duration to 10 min, the cells exhibited late-stage apoptosis and numerous intracellular vacuoles appeared. Our results showed that the expression of ER stress markers (phosphor-eukaryotic initiation factor-2α (p-eif2α), activating transcription factor 4 (ATF4) and C/EBP homologous protein (CHOP)) was remarkably up-regulated after photothermal treatment (mGePVP@SAgel plus laser, and AIMR plus laser) compared to only chemotherapeutic treatment (DOX@SAgel) (**Figure 4.10D, E**), confirming the involvement of the p-eIF2α/ATF4/CHOP pathway in hyperthermia-induced ER stress.

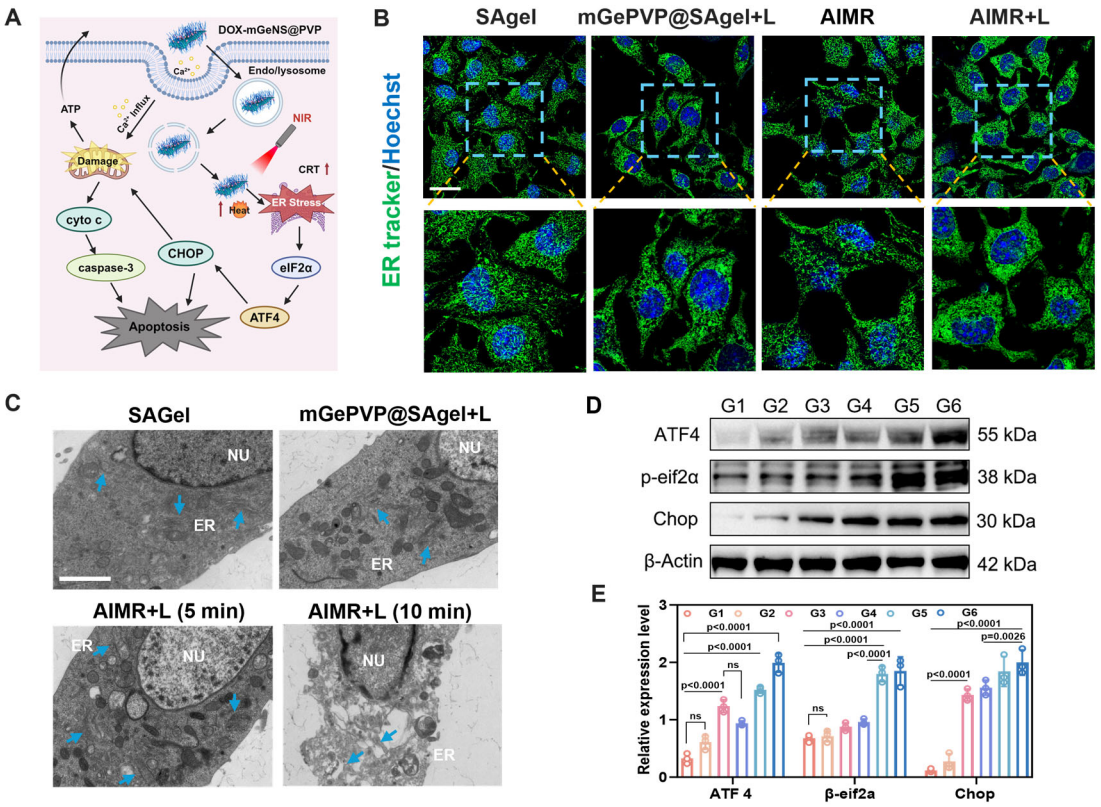

Figure 4.10 Mechanism evaluation of the immune-activating response. (A) scheme illustrating the pathway of ER stress and mitochondrial calcification induce by DOX-mGeNS@PVP *in vitro*. (B) CLSM images of B16F10 cells treated with ER tracker green dye (green) and Hoechst 33324 (blue) after different treatments. The scale bar is 50 μm for all figures. (C) TEM images of B16F10 cells to show the ER stress elicited by SAgel, mGePVP@SAgel plus laser, AIMR, and AIMR plus laser with 980 nm laser irradiation. The scale bar is 1 μm for all figures. Western blot assay (D) and relative expression level quantification (E) of ATF4, p-efi2α, and CHOP expression levels in B16F10 cells respectively after treated withG1 (ctrl plus laser), G2 (SAgel), G3 (DOX@SAgel), G4 (AIMR), G5 (mGePVP@SAgel plus laser), and G6 (AIMR plus laser) (980 nm, 1 W cm ^{2}, 10 min). ns: no significance, data are presented as the mean with SD (n = 3 independent samples). The data were analyzed by one-way ANOVA with Tukey's multiple comparisons post-test.

We analyzed intracellular Ca^{2+} influx cytoplasm from AIMR upon NIR irradiation by Ca^{2+} indicator (Fura-2 AM). Significant Fura-2 AM fluorescence in the cytoplasm was observed in the AIMR plus laser group compared to the control group (**Figure 4.11A, C**). Furthermore, we used the JC-1 probe to measure the mitochondrial membrane potential (MMP) to evaluate the level of Ca^{2+} overload. The SAgel group exhibited weak green fluorescence (JC-1 monomer)

and strong red fluorescence (JC-1 aggregate), indicative of a normal MMP. However, in the AIMR plus laser group, the red fluorescence gradually darkened, while the green fluorescence intensified drastically, resulting in significant suppression of the red-to-green fluorescence intensity ratio (**Figure 4.11B, D)**.

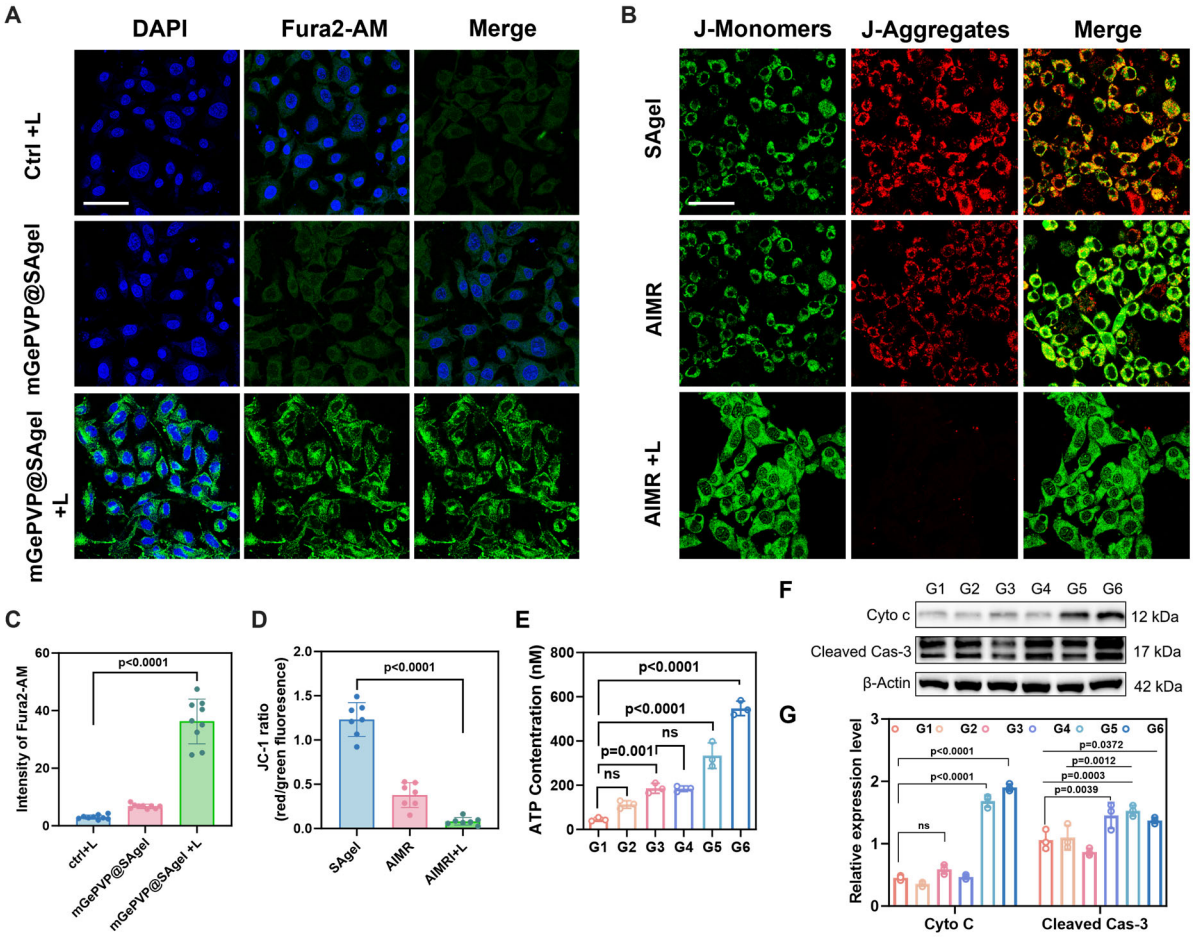

Figure 4.11 Mitochondrial dysfunction through mGePVP@SAgel or AIMR-induced calcium overloading. (A) mGePVP@SAgel induces an increase of intracellular Ca^{2+} in B16F10 cells under laser irradiation. Cell nuclei were stained with DAPI (blue), and the cells were stained with Fura2-AM dye (green). The scale bar is 50 μm for all figures. (B) Mitochondrial membrane potential of B16F10 cells after AIMR treatments detected by the JC-1 (5,5′,6,6′-tetrachloro-1,1′,3,3′-tetraethylbenzimidazolcarbocyanine iodide) assay. The blue and red channel represents J-monomer and J-aggregate, respectively. The scale bar is 50 μm for all figures. (C) Quantification of intracellular Fura2-AM intensity upon different treatments. (D) The JC-1 ratio (J-aggregate fluorescence/J-monomer fluorescence) was calculated according to CLSM. (E) Quantification of the extracellular ATP expression after treatment with various formulations. (F) Western blot assay and (G)

relative expression level quantification of cyto c in the cytoplasm, and cleaved caspase 3 expression levels of B16F10 cells respectively after being treated with G1 (ctrl plus laser), G2 (SAgel), G3 (DOX@SAgel), G4 (AIMR), G5 (mGePVP@SAgel plus laser), and G6 (AIMR plus laser) (980 nm, 1 W cm^2, 10 min). ns: no significance, data are presented as the mean with SD (n=3 independent samples). The data were analyzed by one-way ANOVA with Tukey's multiple comparisons post-test.

Furthermore, the combination of AIMR and laser irradiation induced mitochondrial dysfunction and accelerated cell apoptosis [293], concomitantly accelerating the release of intracellular ATP (**Figure 4.8E**). In addition, ER damage and exogenous Ca^{2+} influx can trigger mitochondrial dysfunction signaling, triggering the release of cytochrome c (cyto c) from mitochondria and upregulating cleaved caspase-3 expression [294]. Western blot analysis revealed a significant induction of cyto c and activation of caspase 3 after the AIMR plus laser treatment compared with other groups, indicating mitochondrial apoptotic (**Figure 4.11F, G**). The above confocal results reflected that our platform could promote Ca^{2+}internalization and DOX penetration upon hyperthermia, exerting potent cytotoxicity toward tumor cells.

4.2.5 *In Vivo* Antitumor Effects and Immune Response of the AIMR

In clinical trials, surgical resection of the primary tumor remains the mainstay treatment approach, however, owing to the advanced tumor progression, complete removal may be impeded, thereby increasing the propensity for recurrence. To suppress the recurrence after surgery, the implantation of therapeutic hydrogels at the resection site has emerged as an effective adjuvant strategy. Therefore, we next sought to determine antitumor therapeutic effects *in vivo* of this strategy using the highly malignant B16F10-Luc melanoma tumor model (**Figure 4.12A**). When the tumor volume reached 100 mm^3 on Day 9, 80% of the tumor tissue was removed to construct a surgery model, and the hydrogel formulations (SAgel, DOX@SAgel, mGePVP@SAgel, and AIMR) were patched into the surgical bed (six groups, n = 5). The entire therapeutic process lasted for 25 days, with NIR irradiation performed on Day 1, 3, and 7 after surgery and hydrogel injection, respectively. Before evaluating the therapeutic efficiency of AIMR, we first evaluated the residence time of DOX on the tumor surgical bed

injected with free DOX, and AIMR with or without laser irradiation, respectively. Compared with the rapid clearance of intravenously injected free DOX from the tumor within 3 days, the fluorescence signal of AIMR could still be observed for more than 10 days, suggesting relatively long tumor retention. Interestingly, upon NIR irradiation, the DOX fluorescence of AIMR gradually decreased from Day 7 onwards, indicating that photothermal-triggered promoted drug release (**Figure 4.12B, D**). In addition, the tumor temperature change in mGePVP@SAgel and AIMR plus laser groups was remarkably increased from 32.6 to 59.8 °C in 5 min (**Figure 4.12C, E**), while the SAgel group showed no significant temperature increase (< 5°C). Importantly, no treatment-associated weight loss was observed in mice, confirming their non-toxicity and good biosafety (**Figure 4.12H**). Furthermore, the bioluminescent signals of tumors in mice receiving the AIMR plus laser group remained extremely weak, demonstrating the effective antitumor properties of our platform (**Figure 4.12F, G**).

In comparison, the tumors in the surgery and SAgel treatment groups exhibited rapid growth, reaching approximately 13.61 and 12.28 times their initial volume, respectively, after 25 days (**Figure 4.12I, J)**. The DOX@SAgel and AIMR without NIR treatment groups exhibited partial tumor inhibition, attributable to the chemotherapeutic effect elicited by the leakage of DOX in the acidic tumor microenvironment. Notably, the AIMR plus laser group showed the best therapeutic outcome, with complete tumor ablation on Day 7 and an 80% survival rate over 60 days (**Figure 4.12K**). These results demonstrate that our AIMR platform can significantly suppress tumor growth *in vivo*.

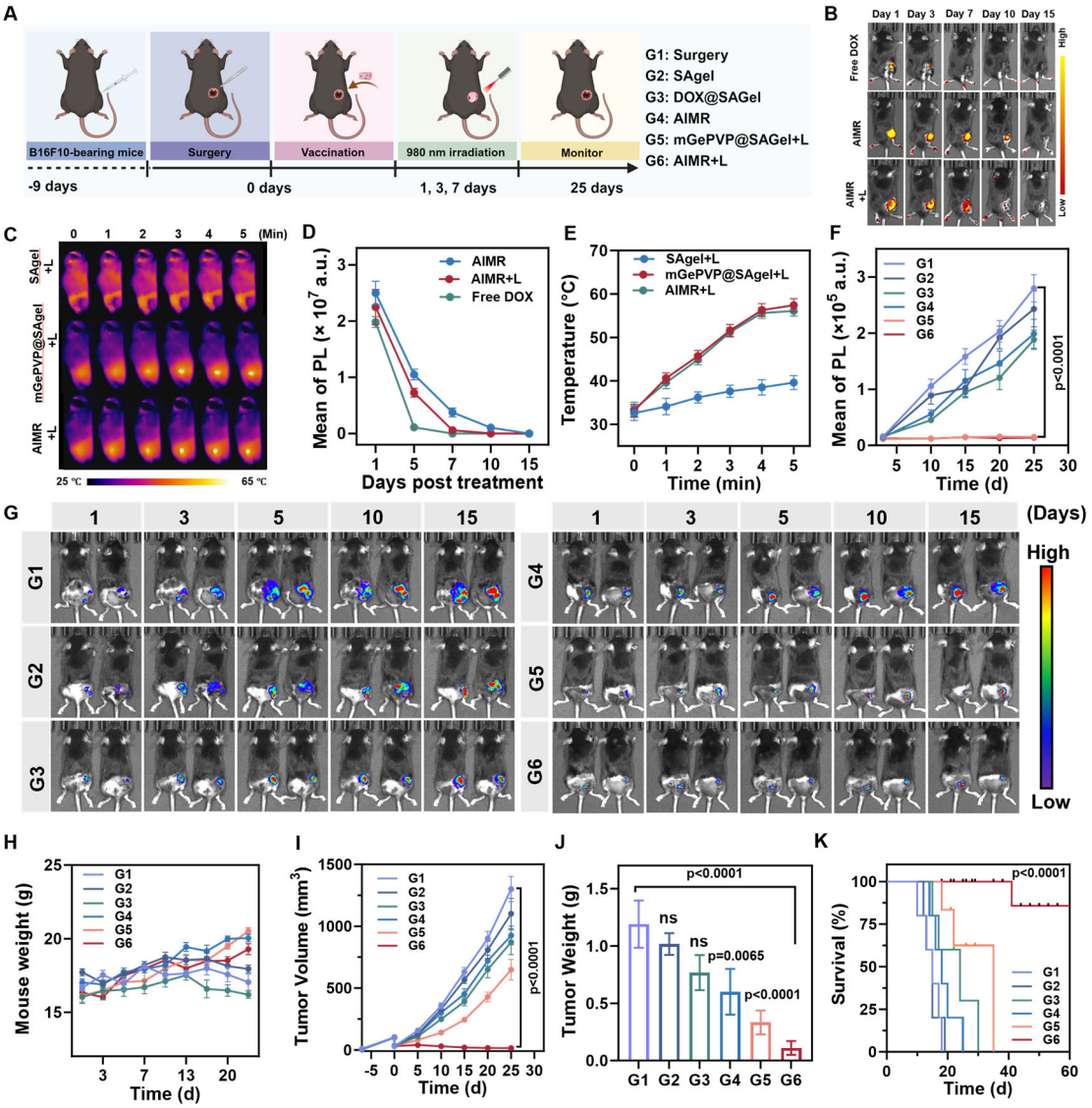

Figure 4.12 Antitumor efficacy of AIMR on B16F10 tumor-bearing mice model. (A) Experiment outline showing the treatment steps and procedures for evaluating therapeutic outcomes in B16F10 or B16F10-Luc tumor-bearing mice. N = 5 mice per group. (B) The DOX release behavior was measured by IVIS imaging of B16F10 tumor-bearing mice after the intravenous injection of free DOX or postoperative implantation of AIMR with or without NIR irradiation at various injection periods. (C) The Temperature change in tumor under laser irradiation recorded by an infrared thermal camera. (D) Relative mean of PL intensity of DOX and (E) the temperature change after different treatments. (F) *In vivo* bioluminescence intensity and (G) IVIS images to track the growth of subcutaneous injected B16F10-Luc cancer cells in different treatment groups of mice after surgery (980 nm, 1.0 W cm^{-2}, 5 min). (H) The mouse weight, (I) tumor volume, (J) tumor weight, and (K) survival rate after different treatments. The treatment groups are G1 (Surgery), G2 (SAgel), G3

(DOX@SAgel), G4 (AIMR), G5 (mGePVP@SAgel plus laser), and G6 (AIMR plus laser) for the above experiment. N = 5 mice per group. Data are represented as mean ± SD. The data were analyzed by one-way ANOVA with Tukey's multiple comparisons post-test.

Representative images (n = 5) depicting tumor sites in mice were captured to illustrate tumor recurrence (**Figure 4.13**). Mice receiving only surgical intervention or SAgel treatment displayed continued tumor growth post-treatment. In contrast, the cohort that underwent surgery coupled with AIMR administration demonstrated a significant tumor recurrence suppression during the 30-day observation period.

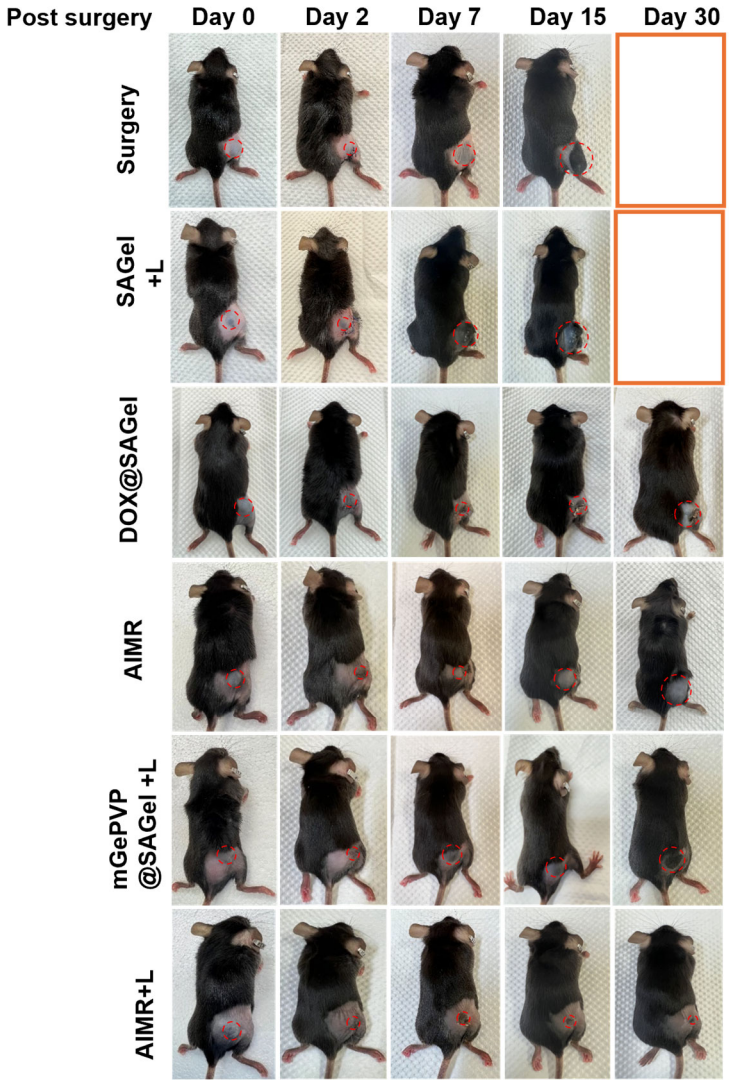

Figure 4.13 Representative mice photos of the tumor site were recorded at different time points upon the different treatments.

To understand the underlying mechanism of the superior anti-tumor efficacy, we examined multiple pro-inflammatory cytokines including IL-6, IFN-γ, and TNF-α in the mouse serum following various treatments. Mice treated with AIMR produce the highest levels of IL-6 (3.8-fold increase), IFN-γ (7.3-fold increase), and TNF-α (5.2-fold increase) at Day 10 upon NIR irradiation, in contrast to only surgery group (**Figure 4.14A-C**). Notably, the secretion levels of all three cytokines (IFN-γ, IL-6, and TNF-α) exhibited a decline after Day 13, indicating the absence of excess cytokines that could cause systemic inflammation. The percentage of matured DCs ($CD11c^+CD80^+CD86^+$) in inguinal lymph nodes significantly increased from ~ 17.3% to 44.9% after treatment with mGePVP@SAgel, while the DCs maturation percentage from mice treated with DOX@SAgel or mGePVP@SAgel only increased to ~ 27.6% and ~ 35.1%, respectively (**Figure 4.14D, E**). Together, these data illustrated that AIMR can effectively attenuate the immunosuppression in the TME and elicit a potent antitumor immune response.

CD8+ cytotoxic T lymphocytes ($CD3^+CD4^-CD8^+$) could directly induce apoptosis in targeted cancer cells [38, 295]. Helper T cells ($CD3^+CD4^+CD8^-$) play important roles in the regulation of adaptive immunities [296]. We analyzed the percentage of activated CD8+ and CD4+ T cells in the spleen of mice on Day 20 after different treatments. The CD8+ T cells within the spleen were upregulated in the AIMR plus laser group with a percentage of 60.5%, rising than that in the surgery, SAgel, and DOX@SAgel at 13.8%, 18.6%, and 31.0%, respectively (**Figure 4.14F**). Moreover, the ratio of CD8+/CD4+ T cells was significantly increased in the mGePVP@SAgel and AIMR plus laser groups, which were 3.3-fold and 2.1-fold higher than that in the only surgery group, respectively (**Figure 4.14G**). In addition to memory T cell activation inducing immunological memory is very important for exerting long-term protection against tumor recurrence [60]. The effector memory T (T_{EM}, $CD8^+CD44^+CD62L^-$cells) cells produced in the spleen can fight against the secondary pathogen infection and inhibit tumor recurrence and metastasis [297]. Importantly, a significant increase (~ 50.9%) in the percentage of T_{EM} was detected in spleens of AIMR with 980 nm laser irradiation-treated group compared with other groups (**Figure 4.14H, I**). Furthermore, the regulatory T cells (Tregs, $CD4^+CD25^+FOXP3^+$cells) within tumor tissues could suppress effective anti-tumor immune response [298]. Thus, we

collected the tumor-infiltrating cells to analyze the proportion of Tregs after co-staining with CD25 and FOXP3 (**Figure 4.14J, K**). Under NIR radiation, both mGePVP@SAgel and AIMR significantly reduced Tregs by 2.4 and 3.5 times, respectively, compared to the surgery group alone, indicating significant immunosuppression. These results suggest that the local delivery and light treatment of AIMR significantly relieves immune suppression and generates memory immunity.

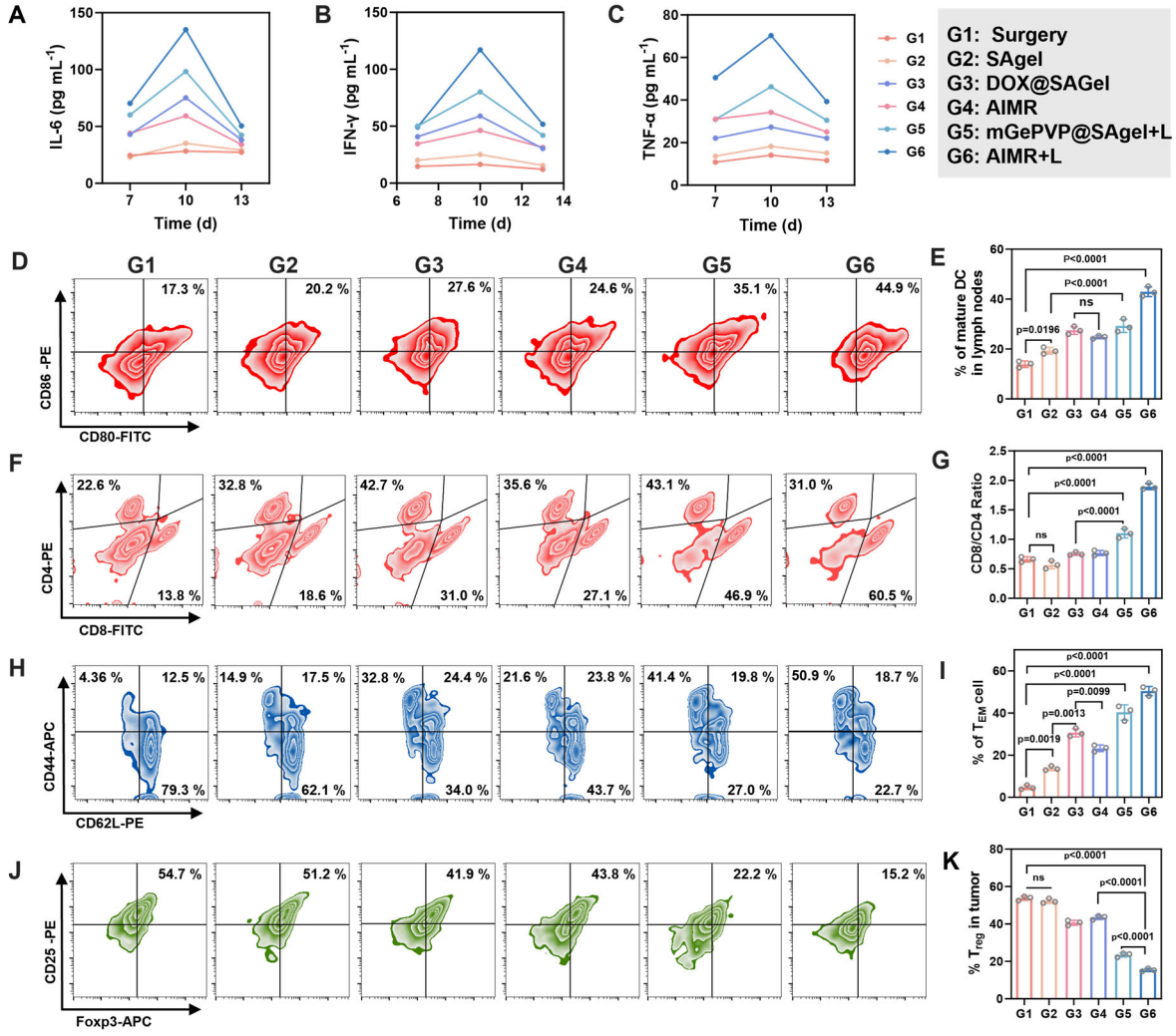

Figure 4.14 Immune-activating efficacy of hydrogel vaccine *in vivo*. Cytokine secretion of (A) IL-6, (B) IFN-λ, and (C) TNF-α in serum (pg mL^{-1}) from mice on Day 7, 10, and 13 after different treatment (n=3). (D) Representative flow cytometry plots and (E) quantification of mature DCs (gated on CD11c+ DCs) in tumor-draining lymph nodes from mice after different treatments (n = 3). (F) Representative flow cytometry plots of CD8+ T cells and CD4+ T cells in spleen CD3+ lymphocytes from mice after different treatment.

(G) The ratio of CD4+ T cells and CD8+ T cells in spleen CD3+ lymphocytes from mice after different treatment (n=3). (H) Representative flow cytometry plots of naïve, central memory, and effector memory T cells (gated on CD8+ T cells) in spleen from mice after different treatments. (I) Quantification of T_{EM} cell (gated on $CD8^{+}CD44^{+}CD62^{-}$ T cells) in spleen from mice after different treatment (n = 3). (J) Representative flow cytometry plots and (K) Quantification of Tregs cells (gated on $CD4^{+}CD25^{+}FOXP3^{+}$ T cells) in tumor-infiltrating cells after different treatments (n = 3). G1: Surgery, G2: SAgel, G3: DOX@SAgel, G4: AIMR, G5: mGePVP@SAgel with laser irradiation, G6: AIMR with laser irradiation. Data are represented as mean ± SD. The data were analyzed by one-way ANOVA with Tukey's multiple comparisons post-test.

At the end of treatment, all mice were sacrificed, the main organs sections were subject to Hematoxylin & Eosin (H&E) staining, and tumor tissue sections were performed for H&E and terminal deoxynucleotidyl transferase dUTP nick end labeling (TUNEL) assay. No abnormal cells were observed from the H&E-stained tissue sections of the main organ (heart, liver, kidney, spleen, and lung), demonstrating the biosafety and low toxicity of our "AIMR" immunomodulator (**Figure 4.15**).

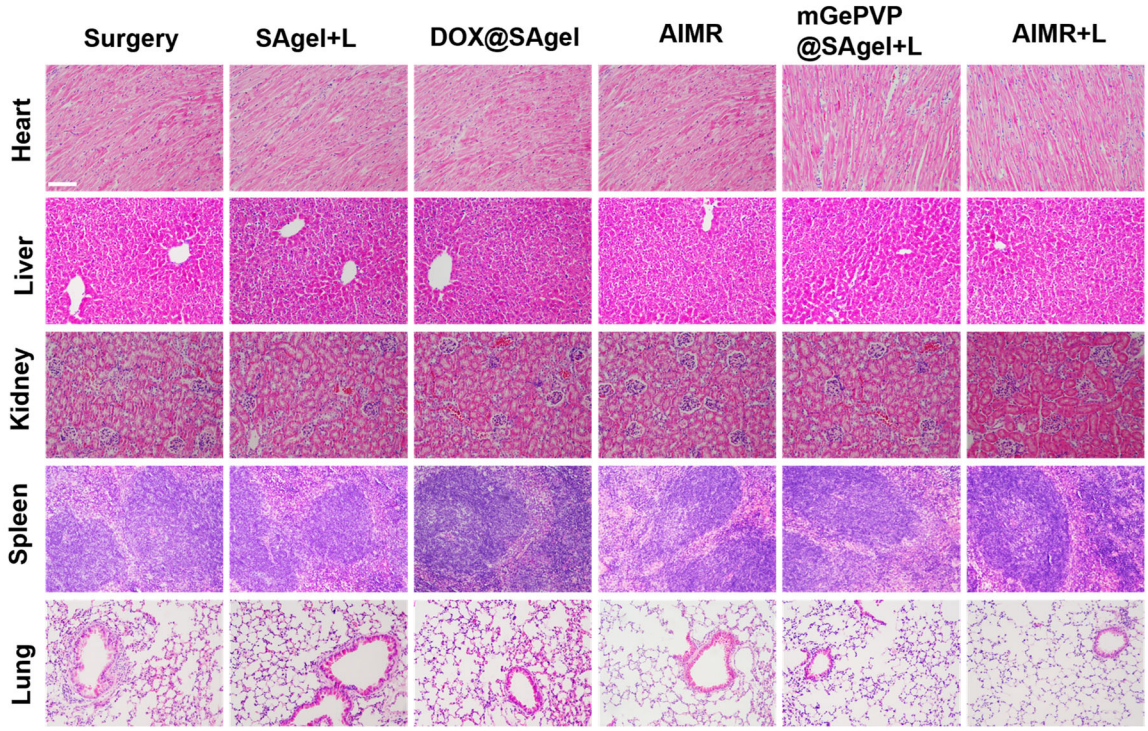

Figure 4.15 H&E staining images of different tissue sections of C57BL/6 mice after different treatments. The scale bar is 100 μm for all figures.

H&E analysis of tumor sections from the AIMR treatment group revealed a marked loss of tumor cell integrity, with the nuclei of most cells appearing shrunken or indistinct. In contrast, the surgery group exhibited visible and well-defined nuclei in tumor cells, indicative of their viable state (**Figure 4.16)**. A significant number of TUNEL-positive cells were detected in tumors formed by AIMR with the laser group, indicating the excellent therapeutic effect of combination therapy. These observations suggest that the AIMR formulation effectively compromised tumor cell viability and induced nuclear condensation, a hallmark of cell death processes.

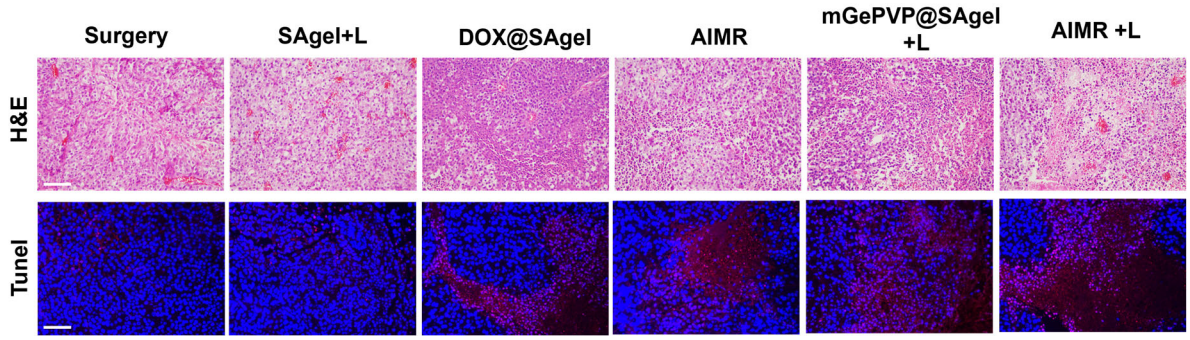

Figure 4.16 H&E staining images and Tunnel staining of tumor sections of C57BL/6 mice after different treatments. The nuclei and their fragments are blue-violet, and the cytoplasm is pink red in H&E staining. The blue channel represents the nuclei, and the red channel represents the apoptotic cell. The scale bar is 100 μm for all figures.

4.3.6 Abscopal Effect and Immunological Memory Induced by AIMR

We further evaluated the immunological memory induced by AIMR under 980 nm laser irradiation in a malignant bilateral B16F10 orthotopic tumor model (left, primary tumor; right, contralateral tumor). To establish a bilateral tumor model, tumor cells were initially inoculated into the right flank of each mouse to induce the primary tumor, followed by a subsequent subcutaneous inoculation of tumor cells into the left flank after 5 days to stimulate the development of a distant tumor (**Figure 4.17A**). Once the inoculated primary tumor reached 100 mm^3, 80% of the primary tumor was surgically resected and administered hydrogel formulation orthotopically. After the therapeutic interventions, the growth kinetics of both

primary and contralateral tumors were monitored over 25 days. As expected, the primary tumors in mice treated with AIMR and photo-irradiation exhibited near-complete ablation, and the growth of contralateral tumors was effectively suppressed (**Figure 4.17B, C)**. However, neither DOX@SAgel nor mGePVP@SAgel plus laser achieved a considerable inhibitory efficiency on primary and contralateral tumors. Moreover, the AIMR plus laser group demonstrated the safety of the therapeutic process and significantly prolonged the survival of tumor-bearing mice with a survival rate exceeding 75% over 60 days (**Figure 4.17D**). The effective inhibition of both primary and distant tumors suggests that AIMR could serve as a platform for combining photothermal therapy and immunotherapy to achieve effective cancer treatment.

Concurrently, AIMR significantly facilitated DCs maturation in the distant tumor-draining lymph nodes (**Figure 4.17E, F**) and promoted activated CD4+ and CD8+ T cell infiltration into the distal tumors (**Figure 4.17G, H**). The percentage of mature DCs in the distant tumor-draining lymph nodes of the AIMR plus laser group was 13.3-fold, 4.8-fold, and 1.5-fold higher than the surgery, SAgel, and mGePVP@SAgel plus laser, respectively. Furthermore, the percentages of help CD4+ T cell and CD8+ T cells within the distal tumors of the AIMR plus laser group were 1.8-fold and 3.4-fold higher, respectively, compared to the surgery-only group, suggesting a potent anti-tumor immune response elicited by AIMR. Subsequently, we assessed whether bilateral tumor-bearing mice treated with the AIMR plus laser group regimen developed immunological memory by quantifying the expression levels of effector memory T cells within the spleens of these animals. Encouragingly, the flow cytometry analysis indicated that the percentage of CD8+ T_{EM} cells ($CD44^{+}CD62L^{-}$) in the spleen of the AIMR plus laser group (46.0%) was higher than that of the surgery group (19.0%) (**Figure 4.17I, J**). H&E and TUNEL staining of the distal tumors further revealed extensive necrotic regions and tumor cell apoptosis in the AIMR plus laser group. These findings demonstrated that AIMR potently induced ICD, thereby prolonging a robust anti-tumor immune response. In addition, no noticeable weight loss was found for mice after all these treatments (**Figure 4.18**).

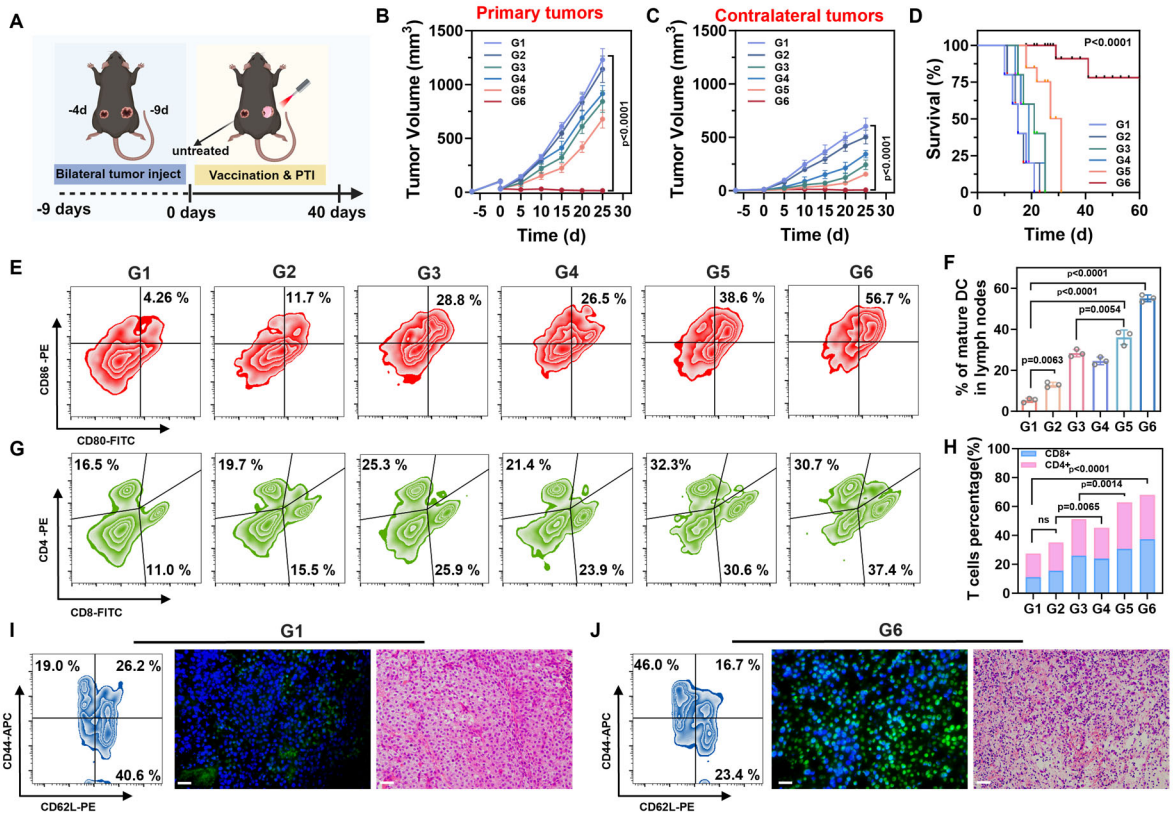

Figure 4.17 Long-term immunological memory assessment of AIMR in a B16F10 orthotopic bilateral tumor model. (A) Schematic illustration of the procedure for tumor rechallenges experiment and immune response analysis by various treatments in bilateral B16F10 tumor-bearing mice model. The primary tumor was removed by surgery and treated with *in situ* injection of G1 (Surgery), G2 (SAgel); G3 (DOX@SAgel), G4 (AIMR), G5 (mGePVP@SAgel plus laser), G6 (AIMR plus laser), respectively. n=5 mice per group. (B) Primary tumor growth curves, (C) contralateral tumor growth curves, and (D) Kaplan-Meier survival plot of B16F10 orthotopic tumor-bearing mice after various treatments (n = 5 mice per group). (E) Representative flow cytometry plots and (F) quantification of mature DCs (gated on $CD11c^+$ DCs) in contralateral tumor-draining lymph nodes from mice after different treatments. (G) Representative flow cytometry plots and (H) quantification of CD4+ T cell and CD8+ T cell in contralateral tumor-infiltrating cells from mice after different treatments (n = 5 mice per group). Representative flow cytometry data of CD8+ T_{EM} cells ($CD44^+CD62L^-$) in the spleen, H&E, and TUNEL staining of contralateral tumors in bilateral B16B10 tumor-bearing mice from (I) SAgel group and (J) AIMR plus laser group on day 20 (n = 5 mice per group). The scale bar is 50 μm for all figures. Data are represented as mean ± SD. The data were analyzed by one-way ANOVA with Tukey's multiple comparisons post-test.

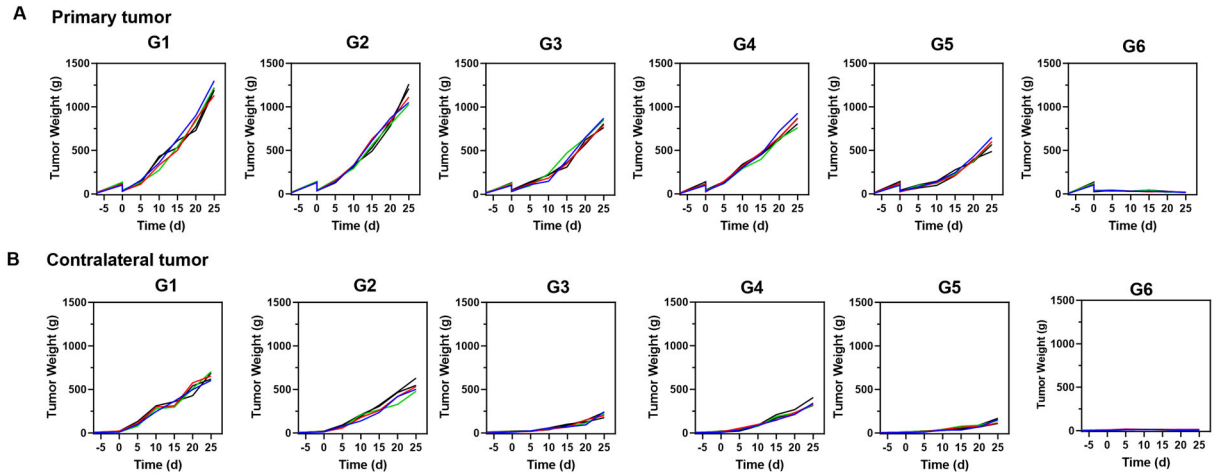

Figure 4.18 Individual tumor growth curves of (A) primary tumor and (B) contralateral tumors in mice post different treatments as indicated (n = 5 mice per group).

4.4 Summary

This study demonstrates an accelerated immunomodulatory matrix reservoir (AIMR), a sodium alginate hydrogel platform incorporating DOX-loaded methyl germanene nanosheets for tumor-specific photothermal therapy and photothermal assisted immunomanipulation to effectively treat malignant tumors. In tumor tissue, the hyperthermia induced by mGeNS@PVP triggered the release of DOX-mGeNS@PVP from AIMR as well as Ca^{2+} ion upon 980 nm NIR light irradiation. Notably, these methyl germanene nanosheets (mGeNS) exhibit exceptional photothermal conversion efficiency (PCE) of 60.6%, and the AIMR platform could control the slow-release kinetics of mGeNS@PVP, thereby enhancing their tumor accumulation, penetration, and cellular internalization *in vivo*. The released DOX-mGeNS@PVP and Ca^{2+} exert their effects through multiple cellular pathways by inducing ER stress, mitochondrial dysfunction, and DNA damage response, synergistically potentiating the secretion of various immunostimulatory DAMPs, such as CRT, ATP, and HMGB1, thereby promoting the cancer immunity cycle. As a result, a robust "abscopal effect" in distant untreated tumors was obtained owing to enhanced infiltration of tumor-infiltrating cytotoxic T cells and decreased Treg. Taken together, we envision that our mGeNS integrated with Ca^{2+} base hydrogel would maximize the effect of mGeNS in modulating tumor immunity.

In summary, we believe that the utilization of mGeNS is the step towards enabling a novel thermosensitive hydrogel-based therapeutic platform and paving the way for the application of smart photothermal reagents toward postoperative tumor management and inhibition of metastasis. We propose that this "AIMR" strategy and integrated hydrogel platform have potential applications in the postoperative treatment of various cancers. Moreover, this approach could be adapted for use with other materials possessing similar immune adjuvant or photo-stimulated immunotherapy functions. Further studies are necessary to evaluate the efficacy of the proposed strategy in metastatic and inoperable tumor models. Moreover, hydrogel reservoirs can be engineered to incorporate various stimulus-responsive immunotherapeutic nanoagents or biomolecules, potentially creating localized "immune factories" for the elimination of residual tumor cells.

Chapter 5: Conclusions and Suggestions for Future Research

5.1 Major findings and conclusion

In conclusion, this thesis explored the multifaceted applications of functionalized nanomaterials in T cell-based biosensing and immunotherapy, underscoring their transformative potential in the diagnosis and treatment of cancer. Across three interconnected studies, we harnessed the unique properties of these nanomaterials to develop innovative solutions for real-time monitoring of T-cell states, sensitive detection of tumor-related genetic mutations, and enhanced immunotherapy strategies.

Chapter 2 introduced a novel AIEgen-based nanoprobe, AIEgen@F127-AptCD8, capable of accurately detecting pH_i in T cells, which serves as a reliable biomarker for monitoring T cell activation and differentiation states. The nanocore of this probe comprises a pair of AIE dyes, TPE-AMC (pH-sensitive moiety) and TPE-TCF, that form a donor-acceptor pair for sensitive detection of pH_i by dual emitting enhancement analysis. The nanoprobe exhibits a distinctly sensitive narrow range of pH_i values (from 6.0 to 7.4) that can precisely distinguish the differentiated lymphocytes from naïve ones based on their distinct pH_i profiles. This work provided a non-invasive tool to monitor activated and nonactivated T cell pH in real time, revealing that activated CD8+ T cells demonstrate lower pHi (6.49 ± 0.09) than the naïve cells (7.26 ± 0.11). In addition, we demonstrated that the glycolytic product profiles (ATP and LA) in T cells strongly correlate with their pH_i profiles, ascertaining the reliability of probing pH_i for predicting T cell states. The specificity and dynamic detection capabilities of this nanoprobe make it a promising tool for indirectly and non-invasively monitoring T cell activation and differentiation states.

Chapter 3 focuses on the application of mGeNS as an aptamer-based biosensor to the field of genetic diagnostics. Building upon the promising optical properties of GeT-NSs, we developed a fluorescence-based biosensor platform, GeT-NSs@FAM-cDNA, for the rapid and sensitive detection of the breast cancer mutant gene BRCA1, known to play a crucial role in T cell maturation and function. The unique optical properties of methyl germanene, including its

ability to quench and restore fluorescence in response to target DNA interaction, enabled rapid and precise genetic analysis. Our work demonstrated the potential of GeT-NSs as a superior fluorescence dye quencher based on the FRET mechanism, enabling ratiometric fluorescence emission analysis (I_{520}/I_{640} nm) for quantitative and selective detection of BRCA1 mutant sequences. GeT-NSs@FAM-cDNA nanoprobe could identify BRCA1 genes with rapid detection around 0.5 h and good sensitivity at the pM level without amplification. Further studies underway include investigating the effect between different differentiation states of T cells and BRCA1 mutations. The present study elucidates the fluorescence quenching mechanism underlying GeT-NSs, thereby establishing a basis for the prospective utilization of these materials in fluorescence sensing applications.

Building upon the findings from the previous studies, chapter 4 addressed the challenges of immune-mediated adverse side effects and insufficient immunogenicity in cancer immunotherapy. By leveraging the photothermal properties of Ge-based nanosheet, we developed a composite hydrogel platform, termed AIMR. This platform is based on photothermal-triggered immunotherapeutic, utilizing NIR light irradiation to promote the programmatic release of DOX-mGeNS@PVP and Ca^{2+} from AIMR. The composite hydrogel is designed to induce tumor *in situ* vaccine production, converting 'cold' tumors into 'hot' tumors based on the ICD mechanism, which is used to eliminate primary and inhibit distant untreated tumors. The synergistic interplay of these components potentiates the immunogenic cycle, thereby augmenting anti-tumor immunity through an increase in the infiltration of CD4+ and CD8+ T cells, a concomitant reduction in Tregs, and the promotion of inflammatory cytokine release. Importantly, this work achieves excellent immunotherapy effects without the assistance of immune checkpoint inhibitors. The strategy proposed in this work effectively solves the shortcomings of Ge-based nanosheets that are easily metabolized or degraded, and increases the accumulation of nanosheets in tumors, thereby achieving excellent therapeutic effects. Overall, this work suggests that the proposed "AIMR" strategy and integrated hydrogel platform are promising for application in the postoperative treatment of various malignancies,

especially in combination with other immune adjuvant properties or photo-stimulated immunotherapy functions.

Collectively, these studies demonstrate the versatility of functionalized nanomaterials in addressing key challenges in T cell-based biosensing and immunotherapy. The AIEgen-based nanoprobe offers a non-invasive tool for monitoring T cell states, and the GeT-NSs based biosensor platform enables rapid and sensitive detection of BRCA1 gene, providing insights into cancer-related gene mutations impact on T cell function. Furthermore, the "AIMR" hydrogel system leverages the superior photothermal-stimulated immunotherapy ability of mGeNs@PVP to overcome the limitations of conventional tumor therapy approaches, paving the way for more effective and personalized cancer treatments. These findings not only contribute to the fundamental understanding of nanomaterial-based T cell biosensing and immunotherapy but also hold significant promise for translational applications in cancer diagnostics, personalized medicine, and the development of novel immunotherapeutic strategies.

5.2 Recommendations for future work

Future research directions for the projects outlined in this thesis focus on optimizing and expanding the applications of functionalized nanomaterials in T cell-based biosensing and immunotherapy.

For the first project, future studies could focus on optimizing the AIEgen-based nanoprobe for broader applications in monitoring various T cell subtypes and their activation states. This could involve the development of multiplexed probes capable of simultaneously detecting multiple biomarkers, thereby providing a more comprehensive understanding of T cell dynamics in different immunological contexts. Furthermore, in the AIEgen-based nanoprobe, efforts should be directed towards optimizing its design to utilize near-infrared (NIR) wavelengths, which offer deeper tissue penetration and reduced scattering, thereby enhancing in vivo imaging accuracy. In addition, developing methodologies for dynamic pHi probing in live animal models will enable real-time tracking of T cell states during immune responses. In

addition, exploring the integration of these nanoprobes with advanced imaging techniques could enhance their utility in real-time, in vivo monitoring of immune responses.

For the second project, building on the promising results of the GeT-NSs@FAM-cDNA biosensor for BRCA1 detection, future research could investigate the application of this platform for other cancer-related genetic mutations and their impact on T cell function. Expanding the range of detectable genetic targets could significantly enhance the diagnostic capabilities of this technology. It is suggested that exploring its capabilities for detecting BRCA1-related microRNAs could provide complementary insights into breast cancer and T cell interactions. Investigating the relationship between BRCA1 gene expression levels and the differentiation states of T cells or breast cancer cells could reveal new therapeutic targets. Furthermore, studies could explore the potential of combining this biosensor with other molecular diagnostic tools to improve the accuracy and speed of genetic analysis in clinical settings.

For the third project, AIMR hydrogel platform presents a novel approach to cancer immunotherapy, and future work could focus on optimizing its formulation and delivery mechanisms to maximize therapeutic efficacy. Investigating the combination of AIMR with other immunotherapeutic agents, such as immune checkpoint inhibitors or cytokine therapies, could further potentiate its anti-tumor effects. Additionally, preclinical and clinical studies are necessary to evaluate the safety, efficacy, and scalability of this platform for potential use in personalized cancer treatment regimens. Furthermore, evaluating the platform's effectiveness in metastatic and inoperable tumor models will assess its potential for integration into treatment regimens for advanced cancers. Collectively, these future directions aim to advance the development of nanomaterial-based technologies for more effective and personalized cancer diagnostics and therapies.

References

[1] Thun, M.J., J.O. DeLancey, M.M. Center, A. Jemal, and E.M. Ward, *The global burden of cancer: priorities for prevention.* Carcinogenesis, 2010. **31**(1): p. 100-10.

[2] Anand, P., A.B. Kunnumakkara, C. Sundaram, K.B. Harikumar, S.T. Tharakan, O.S. Lai, B. Sung, and B.B. Aggarwal, *Cancer is a preventable disease that requires major lifestyle changes.* Pharm Res, 2008. **25**(9): p. 2097-116.

[3] Zhang, Y. and Z. Zhang, *The history and advances in cancer immunotherapy: understanding the characteristics of tumor-infiltrating immune cells and their therapeutic implications.* Cellular & Molecular Immunology, 2020. **17**(8): p. 807-821.

[4] Kim, R., M. Emi, and K. Tanabe, *Cancer immunoediting from immune surveillance to immune escape.* Immunology, 2007. **121**(1): p. 1-14.

[5] Nicholson, L.B., *The immune system.* Essays in Biochemistry, 2016. **60**(3): p. 275-301.

[6] Bercovici, N., M.T. Duffour, S. Agrawal, M. Salcedo, and J.P. Abastado, *New methods for assessing T-cell responses.* Clinical & Experimental Metastasis, 2000. **7**(6): p. 859-64.

[7] Whitesides, G.M.J.N.b., *The'right'size in nanobiotechnology.* 2003. **21**(10): p. 1161-1165.

[8] Zandonella, C.J.N., *Cell nanotechnology: The tiny toolkit.* 2003. **423**(6935): p. 10-13.

[9] Zhang, S.J.N.b., *Fabrication of novel biomaterials through molecular self-assembly.* 2003. **21**(10): p. 1171-1178.

[10] Gao, D. and Z. Yuan, *Photoacoustic-Based Multimodal Nanoprobes: from Constructing to Biological Applications.* International Journal of Biological Sciences, 2017. **13**(4): p. 401-412.

[11] Poncette, L., J. Bluhm, and T. Blankenstein, *The role of CD4 T cells in rejection of solid tumors.* Current Opinion in Immunology, 2022. **74**: p. 18-24.

[12] Lees, J.R., *CD8+ T cells: The past and future of immune regulation.* Cellular Immunology, 2020. **357**: p. 104212.

[13] Koh, C.H., S. Lee, M. Kwak, B.S. Kim, and Y. Chung, *CD8 T-cell subsets: heterogeneity, functions, and therapeutic potential.* Experimental & Molecular Medicine, 2023. **55**(11): p. 2287-2299.

[14] Seder, R.A., P.A. Darrah, and M. Roederer, *T-cell quality in memory and protection: implications for vaccine design.* Nature Reviews Immunology, 2008. **8**(4): p. 247-58.

[15] Gasteiger, G., M. Ataide, and W.J.I.r. Kastenmüller, *Lymph node–an organ for T-cell activation and pathogen defense.* Immunological reviews, 2016. **271**(1): p. 200-220.

[16] Weninger, W., N. Manjunath, and U.H. von Andrian, *Migration and differentiation of CD8+ T cells.* Immunological Reviews, 2002. **186**(1): p. 221-33.

[17] Arens, R. and S.P.J.I.r. Schoenberger, *Plasticity in programming of effector and memory CD8+ T-cell formation.* Immunological reviews, 2010. **235**(1): p. 190-205.

[18] Nel, A.E. and J.F. Miller, *Nano-Enabled COVID-19 Vaccines: Meeting the Challenges of Durable Antibody Plus Cellular Immunity and Immune Escape.* ACS Nano, 2021. **15**(4): p. 5793-5818.

[19] Dogra, P., H.E. Ghoneim, H.A. Abdelsamed, and B.J.E.j.o.i. Youngblood, *Generating long-lived CD8+ T-cell memory: Insights from epigenetic programs.* European journal of

immunology, 2016. **46**(7): p. 1548-1562.
[20] Laidlaw, B.J., J.E. Craft, and S.M. Kaech, *The multifaceted role of CD4(+) T cells in CD8(+) T cell memory.* Nature Reviews Immunology, 2016. **16**(2): p. 102-11.
[21] Mempel, T.R. and C.A. Bauer, *Intravital imaging of CD8+ T cell function in cancer.* Clinical & Experimental Metastasis, 2009. **26**(4): p. 311-27.
[22] Naito, Y., K. Saito, K. Shiiba, A. Ohuchi, K. Saigenji, A. Nagura, and H. Ohtani, *CD8 T cells infiltrated within cancer cell nests as a prognostic factor in human colorectal cancer.* Cancer Research, 1998. **58**(16): p. 3491-3494.
[23] Sun, L., Y. Su, A. Jiao, X. Wang, and B. Zhang, *T cells in health and disease.* Signal Transduction and Targeted Therapy, 2023. **8**(1): p. 235.
[24] Diao, H. and M. Pipkin, *Stability and flexibility in chromatin structure and transcription underlies memory CD8 T-cell differentiation [version 1; peer review: 2 approved].* F1000research, 2019. **8**(1278).
[25] Golubovskaya, V. and L. Wu, *Different Subsets of T Cells, Memory, Effector Functions, and CAR-T Immunotherapy.* Cancers, 2016. **8**(3).
[26] Reading, J.L., F. Gálvez-Cancino, C. Swanton, A. Lladser, K.S. Peggs, and S.A.J.I.r. Quezada, *The function and dysfunction of memory cd 8+ T cells in tumor immunity.* Immunological reviews, 2018. **283**(1): p. 194-212.
[27] Gray, S.M., S.M. Kaech, and M.M.J.I.r. Staron, *The interface between transcriptional and epigenetic control of effector and memory CD 8+ T-cell differentiation.* The international journal of biochemistry & cell biology, 2014. **261**(1): p. 157-168.
[28] Chen, Y., R. Zander, A. Khatun, D.M. Schauder, and W. Cui, *Transcriptional and Epigenetic Regulation of Effector and Memory CD8 T Cell Differentiation.* Frontiers in Immunology, 2018. **9**: p. 2826.
[29] Podshivalova, K. and D.R. Salomon, *MicroRNA regulation of T-lymphocyte immunity: modulation of molecular networks responsible for T-cell activation, differentiation, and development.* Critical Reviews™ in Immunology, 2013. **33**(5): p. 435-76.
[30] Petrus-Reurer, S., M. Romano, S. Howlett, J.L. Jones, G. Lombardi, and K. Saeb-Parsy, *Immunological considerations and challenges for regenerative cellular therapies.* Communications Biology, 2021. **4**(1): p. 798.
[31] Maimela, N.R., S. Liu, and Y. Zhang, *Fates of CD8+ T cells in Tumor Microenvironment.* Computational and Structural Biotechnology, 2019. **17**: p. 1-13.
[32] Almeida, L., M. Lochner, L. Berod, and T. Sparwasser. *Metabolic pathways in T cell activation and lineage differentiation*. in *Seminars in immunology*. 2016. Elsevier.
[33] Cammann, C., A. Rath, U. Reichl, H. Lingel, M. Brunner-Weinzierl, L. Simeoni, B. Schraven, and J.A. Lindquist, *Early changes in the metabolic profile of activated CD8(+) T cells.* BMC Cell Biol, 2016. **17**(1): p. 28.
[34] Chen, C., H. Zheng, E.M. Horwitz, S. Ando, K. Araki, P. Zhao, Z.G. Li, M.L. Ford, R. Ahmed, and C.K. Qu, *Mitochondrial metabolic flexibility is critical for CD8 T cell antitumor immunity.* Science Advances, 2023. **9**(49): p. eadf9522.
[35] Ježek, P., L.J.T.i.j.o.b. Hlavatá, and c. biology, *Mitochondria in homeostasis of reactive oxygen species in cell, tissues, and organism.* The international journal of biochemistry

& cell biology, 2005. **37**(12): p. 2478-2503.
[36] Reina-Campos, M., N.E. Scharping, and A.W. Goldrath, *CD8(+) T cell metabolism in infection and cancer.* Nature Reviews Immunology, 2021. **21**(11): p. 718-738.
[37] Cao, J., S. Liao, F. Zeng, Q. Liao, G. Luo, and Y. Zhou, *Effects of altered glycolysis levels on CD8+ T cell activation and function.* Cell Death & Disease, 2023. **14**(7): p. 407.
[38] Raskov, H., A. Orhan, J.P. Christensen, and I. Gogenur, *Cytotoxic CD8(+) T cells in cancer and cancer immunotherapy.* British Journal of Cancer, 2021. **124**(2): p. 359-367.
[39] Disis, M.L., *Immune regulation of cancer.* Journal of Clinical Oncology, 2010. **28**(29): p. 4531-8.
[40] Bader, J.E., K. Voss, and J.C. Rathmell, *Targeting Metabolism to Improve the Tumor Microenvironment for Cancer Immunotherapy.* Molecular Cell, 2020. **78**(6): p. 1019-1033.
[41] Jass, J.R., *Lymphocytic infiltration and survival in rectal cancer.* Journal of Clinical Pathology, 1986. **39**(6): p. 585-9.
[42] Fu, Q., N. Chen, C. Ge, R. Li, Z. Li, B. Zeng, C. Li, Y. Wang, Y. Xue, X. Song, H. Li, and G. Li, *Prognostic value of tumor-infiltrating lymphocytes in melanoma: a systematic review and meta-analysis.* Oncoimmunology, 2019. **8**(7): p. 1593806.
[43] Wilke, C.M., K. Wu, E. Zhao, G. Wang, and W. Zou, *Prognostic significance of regulatory T cells in tumor.* International Journal of Cancer, 2010. **127**(4): p. 748-58.
[44] Plitas, G., C. Konopacki, K. Wu, P.D. Bos, M. Morrow, E.V. Putintseva, D.M. Chudakov, and A.Y. Rudensky, *Regulatory T Cells Exhibit Distinct Features in Human Breast Cancer.* Immunity, 2016. **45**(5): p. 1122-1134.
[45] Hu, S., H. Duan, Y. Lu, and S. Huang, *The genes regulating sensitivity of tumor cells to T cell-mediated killing: could they be potential personalized immunotherapeutic targets in head and neck squamous cell carcinoma?* Discover Oncology, 2023. **14**(1): p. 199.
[46] Tan, W.C.C., S.N. Nerurkar, H.Y. Cai, H.H.M. Ng, D. Wu, Y.T.F. Wee, J.C.T. Lim, J. Yeong, and T.K.H. Lim, *Overview of multiplex immunohistochemistry/immunofluorescence techniques in the era of cancer immunotherapy.* Cancer Communications 2020. **40**(4): p. 135-153.
[47] Allam, M., T. Hu, J. Lee, J. Aldrich, S.S. Badve, Y. Gokmen-Polar, M. Bhave, S.S. Ramalingam, F. Schneider, and A.F. Coskun, *Spatially variant immune infiltration scoring in human cancer tissues.* npj Precision Oncology, 2022. **6**(1): p. 60.
[48] Stack, E.C., C. Wang, K.A. Roman, and C.C. Hoyt, *Multiplexed immunohistochemistry, imaging, and quantitation: a review, with an assessment of Tyramide signal amplification, multispectruml imaging and multiplex analysis.* Methods, 2014. **70**(1): p. 46-58.
[49] Tassignon, J., W. Burny, S. Dahmani, L. Zhou, P. Stordeur, B. Byl, and D. De Groote, *Monitoring of cellular responses after vaccination against tetanus toxoid: Comparison of the measurement of IFN-γ production by ELISA, ELISPOT, flow cytometry and real-time PCR.* Journal of Immunological Methods, 2005. **305**(2): p. 188-198.
[50] Wieder, E., *Real-time monitoring of immune responses.* Cytotherapy, 2002. **4**(4): p. 347-352.
[51] Chang, X., Y. Zheng, and K. Xu, *Single-Cell RNA Sequencing: Technological Progress*

and Biomedical Application in Cancer Research. Mol Biotechnol, 2024. **66**(7): p. 1497-1519.

[52] Wu, X., X. Yang, Y. Dai, Z. Zhao, J. Zhu, H. Guo, and R. Yang, *Single-cell sequencing to multi-omics: technologies and applications.* Biomarker Research, 2024. **12**(1): p. 110.

[53] Chen, Y., J. Song, Q. Ruan, X. Zeng, L. Wu, L. Cai, X. Wang, and C. Yang, *Single-cell sequencing methodologies: from transcriptome to multi-dimensional measurement.* Small Methods, 2021. **5**(6): p. 2100111.

[54] Fritzsch, F.S., C. Dusny, O. Frick, and A. Schmid, *Single-cell analysis in biotechnology, systems biology, and biocatalysis.* Annual review of chemical and biomolecular engineering, 2012. **3**(1): p. 129-155.

[55] Mehrotra, P., *Biosensors and their applications - A review.* Journal of Oral Biology and Craniofacial Research, 2016. **6**(2): p. 153-9.

[56] Chuah, S. and V. Chew, *High-dimensional immune-profiling in cancer: implications for immunotherapy.* Journal for ImmunoTherapy of Cancer, 2020. **8**(1): p. e000363.

[57] Gupta, S.L., S. Basu, V. Soni, and R.K. Jaiswal, *Immunotherapy: an alternative promising therapeutic approach against cancers.* Molecular Biology Reports 2022. **49**(10): p. 9903-9913.

[58] Xia, Y., M. Sun, H. Huang, and W.L. Jin, *Drug repurposing for cancer therapy.* Signal Transduction and Targeted Therapy, 2024. **9**(1): p. 92.

[59] Chaplin, D.D., *Overview of the immune response.* Journal of Allergy and Clinical Immunology, 2010. **125**(2 Suppl 2): p. S3-23.

[60] Waldman, A.D., J.M. Fritz, and M.J. Lenardo, *A guide to cancer immunotherapy: from T cell basic science to clinical practice.* Nature Reviews Immunology, 2020. **20**(11): p. 651-668.

[61] Trujillo, J.A., R.F. Sweis, R. Bao, and J.J. Luke, *T Cell-Inflamed versus Non-T Cell-Inflamed Tumors: A Conceptual Framework for Cancer Immunotherapy Drug Development and Combination Therapy Selection.* Cancer Immunol Res, 2018. **6**(9): p. 990-1000.

[62] Dang, B.N., T.K. Kwon, S. Lee, J.H. Jeong, and S. Yook, *Nanoparticle-based immunoengineering strategies for enhancing cancer immunotherapy.* Journal of Controlled Release, 2024. **365**: p. 773-800.

[63] Quail, D.F. and J.A. Joyce, *Microenvironmental regulation of tumor progression and metastasis.* Nat Med, 2013. **19**(11): p. 1423-37.

[64] Liu, Y.T. and Z.J. Sun, *Turning cold tumors into hot tumors by improving T-cell infiltration.* Theranostics, 2021. **11**(11): p. 5365-5386.

[65] Wang, D.R., X.L. Wu, and Y.L. Sun, *Therapeutic targets and biomarkers of tumor immunotherapy: response versus non-response.* Signal Transduction and Targeted Therapy, 2022. **7**(1): p. 331.

[66] Rosenberg, S.A., N.P. Restifo, J.C. Yang, R.A. Morgan, and M.E. Dudley, *Adoptive cell transfer: a clinical path to effective cancer immunotherapy.* Nature Reviews Cancer, 2008. **8**(4): p. 299-308.

[67] Berraondo, P., M.F. Sanmamed, M.C. Ochoa, I. Etxeberria, M.A. Aznar, J.L. Perez-Gracia,

M.E. Rodriguez-Ruiz, M. Ponz-Sarvise, E. Castanon, and I. Melero, *Cytokines in clinical cancer immunotherapy.* British Journal of Cancer, 2019. **120**(1): p. 6-15.

[68] Sun, Q., Z. Hong, C. Zhang, L. Wang, Z. Han, and D. Ma, *Immune checkpoint therapy for solid tumours: clinical dilemmas and future trends.* Signal Transduction and Targeted Therapy, 2023. **8**(1): p. 320.

[69] He, X. and C. Xu, *Immune checkpoint signaling and cancer immunotherapy.* Cell Research, 2020. **30**(8): p. 660-669.

[70] Murciano-Goroff, Y.R., A.B. Warner, and J.D. Wolchok, *The future of cancer immunotherapy: microenvironment-targeting combinations.* Cell Research, 2020. **30**(6): p. 507-519.

[71] Fan, T., M. Zhang, J. Yang, Z. Zhu, W. Cao, and C. Dong, *Therapeutic cancer vaccines: advancements, challenges, and prospects.* Signal Transduction and Targeted Therapy, 2023. **8**(1): p. 450.

[72] Liu, J., M. Fu, M. Wang, D. Wan, Y. Wei, and X. Wei, *Cancer vaccines as promising immuno-therapeutics: platforms and current progress.* Journal of Hematology & Oncology, 2022. **15**(1): p. 28.

[73] Muntasell, A., A.C. Berger, and P.A. Roche, *T cell-induced secretion of MHC class II-peptide complexes on B cell exosomes.* EMBO J, 2007. **26**(19): p. 4263-72.

[74] Xie, N., G. Shen, W. Gao, Z. Huang, C. Huang, and L. Fu, *Neoantigens: promising targets for cancer therapy.* Signal Transduction and Targeted Therapy, 2023. **8**(1): p. 9.

[75] Schooten, E., A. Di Maggio, P.M.v.B. en Henegouwen, and M.M.J.C.t.r. Kijanka, *MAGE-A antigens as targets for cancer immunotherapy.* Cancer treatment reviews, 2018. **67**: p. 54-62.

[76] Berman, T.A. and J.T.J.C. Schiller, *Human papillomavirus in cervical cancer and oropharyngeal cancer: one cause, two diseases.* Cancer, 2017. **123**(12): p. 2219-2229.

[77] Zhu, S., T. Zhang, L. Zheng, H. Liu, W. Song, D. Liu, Z. Li, and C.X. Pan, *Combination strategies to maximize the benefits of cancer immunotherapy.* Journal of Hematology & Oncology, 2021. **14**(1): p. 156.

[78] Lin, D., Y. Shen, and T. Liang, *Oncolytic virotherapy: basic principles, recent advances and future directions.* Signal Transduction and Targeted Therapy, 2023. **8**(1): p. 156.

[79] Song, S., Y. Qin, Y. He, Q. Huang, C. Fan, and H.-Y.J.C.S.R. Chen, *Functional nanoprobes for ultrasensitive detection of biomolecules.* 2010. **39**(11): p. 4234-4243.

[80] Wang, J. and X.J.N. Qu, *Recent progress in nanosensors for sensitive detection of biomolecules.* 2013. **5**(9): p. 3589-3600.

[81] Sharmiladevi, P., K. Girigoswami, V. Haribabu, and A. Girigoswami, *Nano-enabled theranostics for cancer.* Materials Advances, 2021. **2**(9): p. 2876-2891.

[82] Paras, K. Yadav, P. Kumar, D.R. Teja, S. Chakraborty, M. Chakraborty, S.S. Mohapatra, A. Sahoo, M.M.C. Chou, C.T. Liang, and D.R. Hang, *A Review on Low-Dimensional Nanomaterials: Nanofabrication, Characterization and Applications.* Nanomaterials (Basel), 2022. **13**(1).

[83] Byakodi, M., N.S. Shrikrishna, R. Sharma, S. Bhansali, Y. Mishra, A. Kaushik, and S. Gandhi, *Emerging 0D, 1D, 2D, and 3D nanostructures for efficient point-of-care*

biosensing. Biosensors and Bioelectronics: X, 2022. **12**: p. 100284.
[84] Chi, X., D. Huang, Z. Zhao, Z. Zhou, Z. Yin, and J. Gao, *Nanoprobes for in vitro diagnostics of cancer and infectious diseases.* Biomaterials, 2012. **33**(1): p. 189-206.
[85] Azzazy, H.M.E. and M.M.H. Mansour, *In vitro diagnostic prospects of nanoparticles.* Clinica Chimica Acta, 2009. **403**(1): p. 1-8.
[86] Lan, H., M. Jamil, G. Ke, and N. Dong, *The role of nanoparticles and nanomaterials in cancer diagnosis and treatment: a comprehensive review.* Am J Cancer Res, 2023. **13**(12): p. 5751-5784.
[87] Cheng, Z., M. Li, R. Dey, and Y. Chen, *Nanomaterials for cancer therapy: current progress and perspectives.* J Hematol Oncol, 2021. **14**(1): p. 85.
[88] Kiran, A.V.R., G.K. Kumari, P.T. Krishnamurthy, and R.R.J.B.S. Khaydarov, *Tumor microenvironment and nanotherapeutics: intruding the tumor fort.* 2021. **9**(23): p. 7667-7704.
[89] De Crozals, G., R. Bonnet, C. Farre, and C. Chaix, *Nanoparticles with multiple properties for biomedical applications: A strategic guide.* Nano Today, 2016. **11**(4): p. 435-463.
[90] Chehelgerdi, M., M. Chehelgerdi, O.Q.B. Allela, R.D.C. Pecho, N. Jayasankar, D.P. Rao, T. Thamaraikani, M. Vasanthan, P. Viktor, N. Lakshmaiya, M.J. Saadh, A. Amajd, M.A. Abo-Zaid, R.Y. Castillo-Acobo, A.H. Ismail, A.H. Amin, and R. Akhavan-Sigari, *Progressing nanotechnology to improve targeted cancer treatment: overcoming hurdles in its clinical implementation.* Molecular Cancer, 2023. **22**(1): p. 169.
[91] Song, S., Y. Qin, Y. He, Q. Huang, C. Fan, and H.-Y. Chen, *Functional nanoprobes for ultrasensitive detection of biomolecules.* Chemical Society Reviews, 2010. **39**(11): p. 4234-4243.
[92] Wang, Y., B. Yan, and L. Chen, *SERS tags: novel optical nanoprobes for bioanalysis.* Chem Rev, 2013. **113**(3): p. 1391-428.
[93] Chen, G., Y.N. Qian, H. Zhang, A. Ullah, X.J. He, Z.G. Zhou, H. Fenniri, and J.L. Shen, *Advances in cancer theranostics using organic-inorganic hybrid nanotechnology.* Applied Materials Today, 2021. **23**: p. 101003.
[94] Alam, P., C. Climent, P. Alemany, and I.R. Laskar, *"Aggregation-induced emission" of transition metal compounds: Design, mechanistic insights, and applications.* Journal of Photochemistry and Photobiology C: Photochemistry Reviews, 2019. **41**: p. 100317.
[95] Chandross, E.A. and C.J. Dempster, *Intramolecular Excimer Formation and Fluorescence Quenching in Dinaphthylalkanes.* Journal of the American Chemical Society, 1970. **92**(12): p. 3586-+.
[96] Geim, A.K., *Graphene: status and prospects.* Science, 2009. **324**(5934): p. 1530-4.
[97] Huang, X., Z. Yin, S. Wu, X. Qi, Q. He, Q. Zhang, Q. Yan, F. Boey, and H.J.s. Zhang, *Graphene-based materials: synthesis, characterization, properties, and applications.* small, 2011. **7**(14): p. 1876-1902.
[98] Cao, X., C. Tan, X. Zhang, W. Zhao, and H.J.A.M. Zhang, *Solution-processed two-dimensional metal dichalcogenide-based nanomaterials for energy storage and conversion.* Advanced Materials, 2016. **28**(29): p. 6167-6196.
[99] Koski, K.J. and Y. Cui, *The new skinny in two-dimensional nanomaterials.* ACS Nano,

2013. **7**(5): p. 3739-43.
[100] Roy, S., K.A. Deo, K.A. Singh, H.P. Lee, A. Jaiswal, and A.K. Gaharwar, *Nano-bio interactions of 2D molybdenum disulfide.* Advanced Drug Delivery Reviews, 2022. **187**: p. 114361.
[101] Niknam, S., S.A. Dehdast, O. Pourdakan, M. Shabani, and M.K.J.N.R.J. Koohi, *Tungsten disulfide nanomaterials (WS2 NM) application in biosensors and nanomedicine: a review.* Nanomedicine Research Journal 2022. **7**(3): p. 214-226.
[102] Lu, F.S., F. Wang, L. Cao, C.Y. Kong, and X.C. Huang, *Hexagonal Boron Nitride Nanomaterials: Advances Towards Bioapplications.* Nanoscience and Nanotechnology Letters, 2012. **4**(10): p. 949-961.
[103] Mir, S.H., V.K. Yadav, and J.K. Singh, *Boron-Carbon-Nitride Sheet as a Novel Surface for Biological Applications: Insights from Density Functional Theory.* ACS Omega, 2019. **4**(2): p. 3732-3738.
[104] Agnihotri, A.S., A. Varghese, and M. Nidhin, *Transition metal oxides in electrochemical and bio sensing: A state-of-art review.* Applied Surface Science Advances, 2021. **4**: p. 100072.
[105] You, Y., C. Yang, X. Zhang, H. Lin, and J. Shi, *Emerging two-dimensional silicene nanosheets for biomedical applications.* Materials Today Nano, 2021. **16**: p. 100132.
[106] Chia, H.L., J. Sturala, R.D. Webster, and M. Pumera, *Functionalized 2D Germanene and Silicene Enzymatic System.* Advanced Functional Materials, 2021. **31**(16): p. 2011125.
[107] Ouyang, J., L. Zhang, L. Li, W. Chen, Z. Tang, X. Ji, C. Feng, N. Tao, N. Kong, T. Chen, Y.N. Liu, and W. Tao, *Cryogenic Exfoliation of 2D Stanene Nanosheets for Cancer Theranostics.* Nano-Micro Letters, 2021. **13**(1): p. 90.
[108] Ping, J.F., Z.X. Fan, M. Sindoro, Y.B. Ying, and H. Zhang, *Recent Advances in Sensing Applications of Two-Dimensional Transition Metal Dichalcogenide Nanosheets and Their Composites.* Advanced Functional Materials, 2017. **27**(19): p. 1605817.
[109] Hu, J. and M. Dong, *Recent advances in two-dimensional nanomaterials for sustainable wearable electronic devices.* Journal of Nanobiotechnology, 2024. **22**(1): p. 63.
[110] Rasul, M.G., A. Kiziltas, B. Arfaei, and R. Shahbazian-Yassar, *2D boron nitride nanosheets for polymer composite materials.* Npj 2d Materials and Applications, 2021. **5**(1): p. 56.
[111] Silva, F., H.P. Chang, J.A.C. Incorvia, M.J. Oliveira, B. Sarmento, S.G. Santos, F.D. Magalhaes, and A.M. Pinto, *2D Nanomaterials and Their Drug Conjugates for Phototherapy and Magnetic Hyperthermia Therapy of Cancer and Infections.* Small, 2024. **20**(13): p. e2306137.
[112] Putri, A.D., B.T. Murti, Y.B. Manga, S. Kanchi, Y.J. Huang, C.W. Peng, P.K. Yang, and C.M. Hsieh, *Whole-Cell Electrochemical Aptasensors for Cancer Diagnosis: Current Advances and Prospects.* Advanced Sensor Research, 2024. **3**(5): p. 2300151.
[113] Kong, R.M., L. Ding, Z. Wang, J. You, and F. Qu, *A novel aptamer-functionalized MoS2 nanosheet fluorescent biosensor for sensitive detection of prostate specific antigen.* Analytical and Bioanalytical Chemistry, 2015. **407**(2): p. 369-77.
[114] Kuang, F., T. Hui, Y. Chen, M. Qiu, and X. Gao, *Post-Graphene 2D Materials: Structures,*

Properties, and Cancer Therapy Applications. Advanced Healthcare Materials, 2024. **13**(5): p. e2302604.

[115] Ramesh, M., R. Janani, C. Deepa, and L. Rajeshkumar, *Nanotechnology-Enabled Biosensors: A Review of Fundamentals, Design Principles, Materials, and Applications.* Biosensors, 2022. **13**(1).

[116] Farka, Z., T. Jurik, D. Kovar, L. Trnkova, and P. Skladal, *Nanoparticle-Based Immunochemical Biosensors and Assays: Recent Advances and Challenges.* Chemical Reviews, 2017. **117**(15): p. 9973-10042.

[117] Doane, T. and C. Burda, *Nanoparticle mediated non-covalent drug delivery.* Advanced Drug Delivery Reviews, 2013. **65**(5): p. 607-21.

[118] Shen, M., J. Rusling, and C.K. Dixit, *Site-selective orientated immobilization of antibodies and conjugates for immunodiagnostics development.* Methods, 2017. **116**: p. 95-111.

[119] Fernández, M. and J. Orozco, *Advances in Functionalized Photosensitive Polymeric Nanocarriers.* Polymers, 2021. **13**(15): p. 2464.

[120] Lu, L., H. Huang, J. Zhou, W. Ma, S. Mackay, and Z. Wang, *BRCA1 mRNA expression modifies the effect of T cell activation score on patient survival in breast cancer.* BMC Cancer, 2019. **19**(1): p. 387.

[121] Liu, J., T. Wang, B. Xiao, M. Deng, P. Yu, and T. Qing, *Fluorometric determination of the breast cancer 1 gene based on the target-induced conformational change of a DNA template for copper nanoclusters.* Analytical Methods, 2021. **13**(5): p. 712-718.

[122] Zhong, D., K. Yang, Y. Wang, and X. Yang, *Dual-channel sensing strategy based on gold nanoparticles cooperating with carbon dots and hairpin structure for assaying RNA and DNA.* Talanta, 2017. **175**: p. 217-223.

[123] Li, K., Y. Chen, N. Zhu, S. Chen, M. Jia, L. Xue, M. Hao, and C. Zhang, *Real-time detection of T cell activation by visualizing TCR nanoclusters with a cholesterol derived aggregation-induced emission probe.* European Journal of Medicinal Chemistry, 2023. **247**: p. 115073.

[124] Cheng, L., X. Wang, F. Gong, T. Liu, and Z. Liu, *2D Nanomaterials for Cancer Theranostic Applications.* Advanced materials, 2020. **32**(13): p. e1902333.

[125] Fang, X., X. Wu, Z. Li, L. Jiang, W.S. Lo, G. Chen, Y. Gu, and W.T. Wong, *Biomimetic Anti-PD-1 Peptide-Loaded 2D FePSe(3) Nanosheets for Efficient Photothermal and Enhanced Immune Therapy with Multimodal MR/PA/Thermal Imaging.* Advanced Science, 2021. **8**(2): p. 2003041.

[126] Fang, X., X. Wu, Z. Li, L. Jiang, W.-S. Lo, G. Chen, Y. Gu, and W.-T. Wong, *Biomimetic Anti-PD-1 Peptide-Loaded 2D FePSe3 Nanosheets for Efficient Photothermal and Enhanced Immune Therapy with Multimodal MR/PA/Thermal Imaging.* Advanced Science, 2021. **8**(2): p. 2003041.

[127] Ahmed, E.M., *Hydrogel: Preparation, characterization, and applications: A review.* Journal of Advanced Research, 2015. **6**(2): p. 105-21.

[128]Revete, A., A. Aparicio, B.A. Cisterna, J. Revete, L. Luis, E. Ibarra, E.A. Segura Gonzalez, J. Molino, and D. Reginensi, *Advancements in the Use of Hydrogels for Regenerative*

Medicine: Properties and Biomedical Applications. International Journal of Biomaterials, 2022. **2022**: p. 3606765.

[129] Hoque, M., M. Alam, S.R. Wang, J.U. Zaman, M.S. Rahman, M.A.H. Johir, L.M. Tian, J.G. Choi, M.B. Ahmed, and M.H. Yoon, *Interaction chemistry of functional groups for natural biopolymer-based hydrogel design.* Materials Science & Engineering R-Reports, 2023. **156**: p. 100758.

[130] Huang, Y., B. Yin, and S.H.D. Wong, *Multicomponent Hydrogels in Clinical and Pharmaceutical Applications*. 2023: Royal Society of Chemisty.

[131] Andrgie, A.T. and H.-C. Tsai, *Hydrogels as local depots for on-demand therapeutic delivery: potential therapeutic approaches for tumor metastasis.* Materials Advances, 2024. **5**(9): p. 3629-3643.

[132] Fu, Y., X. Zhu, L. Ren, J. Wan, and H. Wang, *Syringeable Near-Infrared Light-Activated In Situ Immunogenic Hydrogel Boosts the Cancer-Immunity Cycle to Enhance Anticancer Immunity.* ACS Nano, 2024. **18**(23): p. 14877-14892.

[133] Kim, J., Y. Choi, D.-H. Kim, H.Y. Yoon, and K. Kim, *Injectable Hydrogel-Based Combination Cancer Immunotherapy for Overcoming Localized Therapeutic Efficacy.* pharmaceutics, 2022. **14**(9): p. 1908.

[134] Farhood, B., M. Najafi, and K. Mortezaee, *CD8(+) cytotoxic T lymphocytes in cancer immunotherapy: A review.* J. Cell. Physiol., 2019. **234**(6): p. 8509-8521.

[135] Iwahori, K., *Cytotoxic CD8(+) Lymphocytes in the Tumor Microenvironment.* Adv. Exp. Med. Biol., 2020. **1224**: p. 53-62.

[136] Wong, W.K., B. Yin, A. Rakhmatullina, J. Zhou, and S.H.D. Wong, *Engineering advanced dynamic biomaterials to optimize adoptive T-cell immunotherapy.* Eng. Regen., 2021. **2**: p. 70-81.

[137] MacIver, N.J., R.D. Michalek, and J.C. Rathmell, *Metabolic regulation of T lymphocytes.* Annu. Rev. Immunol., 2013. **31**: p. 259-83.

[138] Liu, H., H. Yang, X. Chen, Y. Lu, Z. Zhang, J. Wang, M. Zhang, L. Xue, F. Xue, and G. Liu, *Cellular metabolism modulation in T lymphocyte immunity.* Immunology., 2014: p. doi: 10.1111/imm.12321.

[139] Janelle, V. and J.S. Delisle, *T-Cell Dysfunction as a Limitation of Adoptive Immunotherapy: Current Concepts and Mitigation Strategies.* Cancers (Basel). 2021. **13**(4).

[140] Pennock, N.D., J.T. White, E.W. Cross, E.E. Cheney, B.A. Tamburini, and R.M. Kedl, *T cell responses: naive to memory and everything in between.* Adv. Physiol. Educ., 2013. **37**(4): p. 273-83.

[141] Gattinoni, L., D.J. Powell, S.A. Rosenberg, and N.P. Restifo, *Adoptive immunotherapy for cancer: building on success.* Nat. Rev. Immunol., 2006. **6**(5): p. 383-393.

[142] Shyer, J.A., R.A. Flavell, and W. Bailis, *Metabolic signaling in T cells.* Cell Res., 2020. **30**(8): p. 649-659.

[143] Wong, W.K., B. Yin, C.Y.K. Lam, Y. Huang, J. Yan, Z. Tan, and S.H.D. Wong, *The Interplay Between Epigenetic Regulation and CD8(+) T Cell Differentiation/Exhaustion for T Cell Immunotherapy.* Front. Cell Dev. Biol., 2021. **9**: p. 783227.

[144] Whitmire , J.K., J.T. Tan , and J.L. Whitton *Interferon-γ acts directly on CD8+ T cells to increase their abundance during virus infection.* J. Exp. Med., 2005. **201**(7): p. 1053-1059.

[145] Zhou, J., P. Nagarkatti, Y. Zhong, and M. Nagarkatti, *Characterization of T-cell memory phenotype after in vitro expansion of tumor-infiltrating lymphocytes from melanoma patients.* Anticancer Res., 2011. **31**(12): p. 4099-109.

[146] Renner, K., C. Bruss, A. Schnell, G. Koehl, H.M. Becker, M. Fante, A.-N. Menevse, N. Kauer, R. Blazquez, L. Hacker, S.-M. Decking, T. Bohn, S. Faerber, K. Evert, L. Aigle, S. Amslinger, M. Landa, O. Krijgsman, E.A. Rozeman, C. Brummer, P.J. Siska, K. Singer, S. Pektor, M. Miederer, K. Peter, E. Gottfried, W. Herr, I. Marchiq, J. Pouyssegur, W.R. Roush, S. Ong, S. Warren, T. Pukrop, P. Beckhove, S.A. Lang, T. Bopp, C.U. Blank, J.L. Cleveland, P.J. Oefner, K. Dettmer, M. Selby, and M. Kreutz, *Restricting Glycolysis Preserves T Cell Effector Functions and Augments Checkpoint Therapy.* Cell Rep., 2019. **29**(1): p. 135-150.e9.

[147] Almeida, L., M. Lochner, L. Berod, and T. Sparwasser, *Metabolic pathways in T cell activation and lineage differentiation.* Semin. Immunol., 2016. **28**(5): p. 514-524.

[148] O'Sullivan, D., *The metabolic spectrum of memory T cells.* Immunol. Cell Biol., 2019. **97**(7): p. 636-646.

[149] Wu, H., V. Estrella, M. Beatty, D. Abrahams, A. El-Kenawi, S. Russell, A. Ibrahim-Hashim, D.L. Longo, Y.K. Reshetnyak, A. Moshnikova, O.A. Andreev, K. Luddy, M. Damaghi, K. Kodumudi, S.R. Pillai, P. Enriquez-Navas, S. Pilon-Thomas, P. Swietach, and R.J. Gillies, *T-cells produce acidic niches in lymph nodes to suppress their own effector functions.* Nat. Commun., 2020. **11**(1): p. 4113.

[150] Reina-Campos, M., N.E. Scharping, and A.W. Goldrath, *CD8+ T cell metabolism in infection and cancer.* Nat. Rev. Immunol., 2021. **21**(11): p. 718-738.

[151] Li, B., Z. Gu, N. Kurniawan, W. Chen, and Z.P. Xu, *Manganese-Based Layered Double Hydroxide Nanoparticles as a T(1) -MRI Contrast Agent with Ultrasensitive pH Response and High Relaxivity.* Adv. Mater., 2017. **29**(29): p. 1700373.

[152] Huang, Y., T. Lv, T. Qin, Z. Xu, L. Wang, and B. Liu, *A DS2-specific flavonoid-based probe with a unique dual-emissive response to human serum albumin.* ChemComm., 2020. **56**(75): p. 11094-11097.

[153] Thomas, D., V. Rubio, V. Iragavarapu, E. Guzman, O.B. Pelletier, S. Alamgir, Q. Zhang, and M.J. Stawikowski, *Solvatochromic and pH-Sensitive Fluorescent Membrane Probes for Imaging of Live Cells.* ACS Chem. Neurosci., 2021. **12**(4): p. 719-734.

[154] Lou, X., M. Zhang, Z. Zhao, X. Min, A. Hakeem, F. Huang, P. Gao, F. Xia, and B.Z. Tang, *A photostable AIE fluorogen for lysosome-targetable imaging of living cells.* J. Mater. Chem. B., 2016. **4**(32): p. 5412-5417.

[155] Liu, J., Y. Li, L. Liu, Y. Gao, Y. Zhang, Z. Yin, F. Pi, and X. Sun, *Current Progress on Antibiotic Sensing Based on Ratiometric Fluorescent Sensors.* Bull Environ Contam Toxicol, 2021. **107**(2): p. 176-184.

[156] Reo, Y.J., Y.W. Jun, S. Sarkar, M. Dai, and K.H. Ahn, *Ratiometric Imaging of γ-Glutamyl Transpeptidase Unperturbed by pH, Polarity, and Viscosity Changes: A Benzocoumarin-*

Based Two-Photon Fluorescent Probe. Anal. Chem., 2019. **91**(21): p. 14101-14108.
[157] Li, R., J. Guo, Y. Duan, X. Liu, L. Gui, Y. Xu, X. Kong, Y. Li, H. Chen, and Z. Yuan, *Monitoring inflammation-cancer progression by cell viscosity, polarity and leucine aminopeptidase using multicolor fluorescent probe.* Chem. Eng. J., 2022. **435**: p. 135043.
[158] Gui, R., H. Jin, X. Bu, Y. Fu, Z. Wang, and Q. Liu, *Recent advances in dual-emission ratiometric fluorescence probes for chemo/biosensing and bioimaging of biomarkers.* Coord. Chem. Rev., 2019. **383**: p. 82-103.
[159] He, L., X. Yang, K. Xu, X. Kong, and W. Lin, *A multi-signal fluorescent probe for simultaneously distinguishing and sequentially sensing cysteine/homocysteine, glutathione, and hydrogen sulfide in living cells.* Chem. Sci., 2017. **8**(9): p. 6257-6265.
[160] Briggs, M.S., D.D. Burns, M.E. Cooper, and S.J. Gregory, *A pH sensitive fluorescent cyanine dye for biological applications.* ChemComm., 2000(23): p. 2323-2324.
[161] Yue, Y., F. Huo, S. Lee, C. Yin, and J. Yoon, *A review: the trend of progress about pH probes in cell application in recent years.* Analyst., 2017. **142**(1): p. 30-41.
[162] Wu, W.-C., C.-Y. Chen, Y. Tian, S.-H. Jang, Y. Hong, Y. Liu, R. Hu, B.Z. Tang, Y.-T. Lee, C.-T. Chen, W.-C. Chen, and A.K.Y. Jen, *Enhancement of Aggregation-Induced Emission in Dye-Encapsulating Polymeric Micelles for Bioimaging.* Adv. Funct. Mater., 2010. **20**(9): p. 1413-1423.
[163] Zhang, Q., B. Yin, J. Hao, L. Ma, Y. Huang, X. Shao, C. Li, Z. Chu, C. Yi, S.H.D. Wong, and M. Yang, *An AIEgen/graphene oxide nanocomposite (AIEgen@GO)-based two-stage "turn-on" nucleic acid biosensor for rapid detection of SARS-CoV-2 viral sequence.* Aggregate, 2022. **4**: p. e195.
[164] Zhang, Q., B. Yin, Y. Huang, Y. Gu, J. Yan, J. Chen, C. Li, Y. Zhang, S.H.D. Wong, and M. Yang, *A dual "turn-on" biosensor based on AIE effect and FRET for in situ detection of miR-125b biomarker in early Alzheimer's disease.* Biosens. Bioelectron., 2023. **230**: p. 115270.
[165] Liu, Y.Y., X. Zhang, K. Li, Q.C. Peng, Y.J. Qin, H.W. Hou, S.Q. Zang, and B.Z. Tang, *Restriction of Intramolecular Vibration in Aggregation-Induced Emission Luminogens: Applications in Multifunctional Luminescent Metal–Organic Frameworks.* Angew. Chem. Int. Ed., 2021. **60**(41): p. 22417-22423.
[166] Mei, J., N.L. Leung, R.T. Kwok, J.W. Lam, and B.Z.J.C.r. Tang, *Aggregation-induced emission: together we shine, united we soar!* Chem. Rev., 2015. **115**(21): p. 11718-11940.
[167] Dai, J., X. Dong, Q. Wang, X. Lou, F. Xia, and S. Wang, *PEG-Polymer Encapsulated Aggregation-Induced Emission Nanoparticles for Tumor Theranostics.* Adv. Healthc. Mater., 2021. **10**(24): p. e2101036.
[168] Qiao, W., T. Ma, S. Wang, L. Li, M. Liu, H. Jiang, Y. Wu, J. Zhu, and Z.a. Li, *Designing Squaraine Dyes with Bright Deep-Red Aggregation-Induced Emission for Specific and Ratiometric Fluorescent Detection of Hypochlorite.* Adv. Funct. Mater., 2021. **31**(45): p. 2105452.
[169] Wurthner, F., *Aggregation-Induced Emission (AIE): A Historical Perspective.* Angew. Chem. Int. Ed., 2020. **59**(34): p. 14192-14196.
[170] Hu, R., C. Dai, C. Wang, J. Lin, H. Hu, Z. Li, H. Lin, L. Ding, Y. Chen, and B. Zhang,

Engineering 2D Arsenic-Phosphorus Theranostic Nanosheets. Advanced Functional Materials, 2021. **31**(25).

[171] Kwok, R.T., C.W. Leung, J.W. Lam, and B.Z. Tang, *Biosensing by luminogens with aggregation-induced emission characteristics.* Chem. Soc. Rev., 2015. **44**(13): p. 4228-38.

[172] Cui, Y., R. Zhang, L. Yang, and S. Lv, *Self-carried AIE nanoparticles for in vitro non-invasive long-term imaging.* Chin. Chem. Lett., 2019. **30**(5): p. 1078-1082.

[173] Ma, H., R. Li, H. Meng, M. Tian, X. Zhang, Y. Liu, L. Li, J. Yuan, and Y. Wei, *A Versatile Theranostic Nanoplatform with Aggregation-Induced Emission Properties: Fluorescence Monitoring, Cellular Organelle Targeting, and Image-Guided Photodynamic Therapy.* Small., 2023. **19**(21): p. e2204778.

[174] Chen, Y.Y., *Cell fishing with DNA aptamers.* Nat. Biomed. Eng., 2019. **3**(10): p. 757-758.

[175] Casey, J.R., S. Grinstein, and J. Orlowski, *Sensors and regulators of intracellular pH.* Nat. Rev. Mol. Cell Biol., 2010. **11**(1): p. 50-61.

[176] Wang, Y.J., Y. Shi, Z. Wang, Z. Zhu, X. Zhao, H. Nie, J. Qian, A. Qin, J.Z. Sun, and B.Z. Tang, *A Red to Near-IR Fluorogen: Aggregation-Induced Emission, Large Stokes Shift, High Solid Efficiency and Application in Cell-Imaging.* Chemistry., 2016. **22**(28): p. 9784-91.

[177] Feng, Q., Y. Li, L. Wang, C. Li, J. Wang, Y. Liu, K. Li, and H. Hou, *Multiple-color aggregation-induced emission (AIE) molecules as chemodosimeters for pH sensing.* ChemComm., 2016. **52**(15): p. 3123-3126.

[178] Suthiwangcharoen, N. and R. Nagarajan, *Controlled design and construction of multifunctional nanoparticles by molecular self-assembly.* Rsc Adv. , 2014. **4**(20): p. 10076-10089.

[179] Zhang, W., K. Gilstrap, L. Wu, C.R. K, M.A. Moss, Q. Wang, X. Lu, and X. He, *Synthesis and characterization of thermally responsive Pluronic F127-chitosan nanocapsules for controlled release and intracellular delivery of small molecules.* ACS Nano., 2010. **4**(11): p. 6747-59.

[180] Zhang, H., Z. Zhao, A.T. Turley, L. Wang, P.R. McGonigal, Y. Tu, Y. Li, Z. Wang, R.T.K. Kwok, J.W.Y. Lam, and B.Z. Tang, *Aggregate Science: From Structures to Properties.* Adv. Mater., 2020. **32**(36): p. e2001457.

[181] Tao, M., J. Mao, Y. Bao, F. Liu, Y. Mai, S. Guan, S. Luo, Y. Huang, Z. Li, Y. Zhong, B. Wei, J. Pan, Q. Wang, L. Zheng, and B. Situ, *A Blood-Responsive AIE Bioprobe for the Ultrasensitive Detection and Assessment of Subarachnoid Hemorrhage.* Adv. Sci., 2023. **10**(8): p. e2205435.

[182] Constantinou, A.P., V. Nele, J.J. Doutch, J. S. Correia, R.V. Moiseev, M. Cihova, D.C.A. Gaboriau, J. Krell, V.V. Khutoryanskiy, M.M. Stevens, and T.K. Georgiou, *Investigation of the Thermogelation of a Promising Biocompatible ABC Triblock Terpolymer and Its Comparison with Pluronic F127.* Macromolecules., 2022. **55**(5): p. 1783-1799.

[183] Yin, G., Y. Li, S. Li, B. Xu, Q. Yang, Y. Zhang, J. Zhao, and X. Cao, *Hexaphenylbenzene based push-pull fluorophores displaying intriguing polarity-dependent fluorescence behavior, AIE(E) characteristics and mega-large Stokes shifts.* Dyes and Pigments, 2022.

198: p. 110013.
[184] Dong, J., K.M. Solntsev, and L.M. Tolbert, *Solvatochromism of the Green Fluorescence Protein Chromophore and Its Derivatives.* J. Am. Chem. Soc., 2006. **128**(37): p. 12038-12039.
[185] Freedy, A.M., M.J. Matos, O. Boutureira, F. Corzana, A. Guerreiro, P. Akkapeddi, V.J. Somovilla, T. Rodrigues, K. Nicholls, B. Xie, G. Jiménez-Osés, K.M. Brindle, A.A. Neves, and G.J.L. Bernardes, *Chemoselective Installation of Amine Bonds on Proteins through Aza-Michael Ligation.* J. Am. Chem. Soc., 2017. **139**(50): p. 18365-18375.
[186] Klak, M., M. Gomółka, T. Dobrzański, G. Tymicki, P. Cywoniuk, P. Kowalska, K. Kosowska, T. Bryniarski, A. Berman, A. Dobrzyń, J. Idaszek, W. Święszkowski, and M. Wszoła, *Irradiation with 365 nm and 405 nm wavelength shows differences in DNA damage of swine pancreatic islets.* PloS one., 2020. **15**(6): p. e0235052.
[187] Gao, W., J.M. Chan, and O.C. Farokhzad, *pH-Responsive Nanoparticles for Drug Delivery.* Mol. Pharm., 2010. **7**(6): p. 1913-1920.
[188] Hou, K., Z.-X. Wu, X.-Y. Chen, J.-Q. Wang, D. Zhang, C. Xiao, D. Zhu, J.B. Koya, L. Wei, J. Li, and Z.-S. Chen, *Microbiota in health and diseases.* Signal Transduct. Target. Ther. , 2022. **7**(1): p. 135.
[189] Yin, J., Y. Hu, and J. Yoon, *Fluorescent probes and bioimaging: alkali metals, alkaline earth metals and pH.* Chem. Soc. Rev., 2015. **44**(14): p. 4619-4644.
[190] Chagri, S., D.Y.W. Ng, and T. Weil, *Designing bioresponsive nanomaterials for intracellular self-assembly.* Nat. Rev. Chem., 2022. **6**(5): p. 320-338.
[191] Liu, Y., X. Chen, X. Liu, W. Guan, and C. Lu, *Aggregation-induced emission-active micelles: synthesis, characterization, and applications.* Chem. Soc. Rev., 2023. **52**(4): p. 1456-1490.
[192] Lyons, G.E., T. Moore, N. Brasic, M. Li, J.J. Roszkowski, and M.I. Nishimura, *Influence of Human CD8 on Antigen Recognition by T-Cell Receptor–Transduced Cells.* Cancer Res., 2006. **66**(23): p. 11455-11461.
[193] Kacherovsky, N., Cardle, II, E.L. Cheng, J.L. Yu, M.L. Baldwin, S.J. Salipante, M.C. Jensen, and S.H. Pun, *Traceless aptamer-mediated isolation of CD8(+) T cells for chimeric antigen receptor T-cell therapy.* Nat. Biomed. Eng., 2019. **3**(10): p. 783-795.
[194] Michl, J., K.C. Park, and P. Swietach, *Evidence-based guidelines for controlling pH in mammalian live-cell culture systems.* Commun. Biol., 2019. **2**(1): p. 144.
[195] Bo, Y. and H. Wang, *Biomaterial-Based In Situ Cancer Vaccines.* Advanced materials, 2023. **n/a**(n/a): p. e2210452.
[196] More, K.N., S.-K. Mun, J. Kang, J.-J. Kim, S.-T. Yee, and D.-J. Chang, *Molecular design of fluorescent pH sensors based on reduced rhodol by structure-pKa relationship for imaging of lysosome.* Dyes Pigm. , 2021. **184**: p. 108785.
[197] Cai, Y., C. Gui, K. Samedov, H. Su, X. Gu, S. Li, W. Luo, H.H.Y. Sung, J.W.Y. Lam, R.T.K. Kwok, I.D. Williams, A. Qin, and B.Z. Tang, *An acidic pH independent piperazine–TPE AIEgen as a unique bioprobe for lysosome tracing.* Chem. Sci., 2017. **8**(11): p. 7593-7603.
[198] Phan, J.R., D.M. Do, M.C. Truong, C. Ngo, J.H. Phan, S.K. Sharma, A. Schilke, C.C.

Mefferd, J.V. Villarama, D. Lai, A. Consul, B.P. Hedlund, S.M. Firestine, and E. Abel-Santos, *An Aniline-Substituted Bile Salt Analog Protects both Mice and Hamsters from Multiple Clostridioides difficile Strains.* Antimicrob. Agents Chemother. , 2022. **66**(1): p. e0143521.

[199] Du, M., N. Kalia, G. Frumento, F. Chen, and Z. Zhang, *Biomechanical properties of human T cells in the process of activation based on diametric compression by micromanipulation.* Med. Eng. Phys., 2017. **40**: p. 20-27.

[200] Pollizzi, K.N., A.T. Waickman, C.H. Patel, I.H. Sun, and J.D. Powell, *Cellular Size as a Means of Tracking mTOR Activity and Cell Fate of CD4+ T Cells upon Antigen Recognition.* PLoS ONE., 2015. **10**(4): p. e0121710.

[201] Goulding, J., V. Tahiliani, and S. Salek-Ardakani, *OX40:OX40L axis: emerging targets for improving poxvirus-based CD8+ T-cell vaccines against respiratory viruses.* Immunol. Rev., 2011. **244**(1): p. 149-68.

[202] Oh, J., X. Xia, W.K.R. Wong, S.H.D. Wong, W. Yuan, H. Wang, C.H.N. Lai, Y. Tian, Y.P. Ho, H. Zhang, Y. Zhang, G. Li, Y. Lin, and L. Bian, *The Effect of the Nanoparticle Shape on T Cell Activation.* Small., 2022. **18**(36): p. e2107373.

[203] Wilkinson, L. and T. Gathani, *Understanding breast cancer as a global health concern.* British Journal of Radiology, 2022. **95**(1130): p. 20211033.

[204] Fu, X., W. Tan, Q. Song, H. Pei, and J. Li, *BRCA1 and Breast Cancer: Molecular Mechanisms and Therapeutic Strategies.* Frontiers in Cell and Developmental Biology, 2022. **10**: p. 813457.

[205] Wu, B., L. Qi, H.-C. Chiang, H. Pan, X. Zhang, A. Greenbaum, E. Stark, L.-J. Wang, Y. Chen, B.R. Haddad, D. Clagett, C. Isaacs, R. Elledge, A. Horvath, Y. Hu, and R. Li, *BRCA1 deficiency in mature CD8+ T lymphocytes impairs antitumor immunity.* Journal for ImmunoTherapy of Cancer, 2023. **11**(2): p. e005852.

[206] Gross, E., N. Arnold, J. Goette, U. Schwarz-Boeger, and M. Kiechle, *A comparison of BRCA1 mutation analysis by direct sequencing, SSCP and DHPLC.* Human Genetics, 1999. **105**(1-2): p. 72-8.

[207] Tian, H., A. Jaquins-Gerstl, N. Munro, M. Trucco, L.C. Brody, and J.P. Landers, *Single-strand conformation polymorphism analysis by capillary and microchip electrophoresis: a fast, simple method for detection of common mutations in BRCA1 and BRCA2.* Genomics, 2000. **63**(1): p. 25-34.

[208] Wallace, A.J., *New challenges for BRCA testing: a view from the diagnostic laboratory.* European Journal of Human Genetics, 2016. **24 Suppl 1**(Suppl 1): p. S10-8.

[209] Tan, C., G. Xie, S. Wu, C. Song, J. Zhang, X. Yi, J. Wang, and H. Tang, *Simultaneous detection of breast cancer biomarkers circROBO1 and BRCA1 based on a CRISPR-Cas13a/Cas12a system.* Biosensors and Bioelectronics, 2024. **258**: p. 116373.

[210] Yadav, P.K., A. Kumar, S. Upadhyay, A. Kumar, A. Srivastava, M. Srivastava, and S.J.M.A. Srivastava, *2D material–based surface plasmon resonance biosensors for applications in different domains: an insight.* Microchimica Acta, 2024. **191**(7): p. 1-30.

[211] Britto, J.S., X. Guan, T.K.A. Tran, Z. Lei, R. Bahadur, V. Patel, X. Zhang, S.L. Wong, and A.J.S.S. Vinu, *Emerging multifunctional carbon-nanomaterial-based biosensors for*

cancer diagnosis. Small Science, 2024. **4**(3): p. 2300221.
[212] Yıldır, M.H., G. Kurtay, W. Bouali, A.A. Genç, and N.J.M.J. Erk, *Redefining precision in cancer treatment: a novel electrochemical approach using bimetal oxide composites for Niraparib quantification.* Microchemical Journal, 2024. **196**: p. 109618.
[213] Khazaei, M., M.S. Hosseini, A.M. Haghighi, and M. Misaghi, *Nanosensors and their applications in early diagnosis of cancer.* Sensing and Bio-Sensing Research, 2023. **41**: p. 100569.
[214] Sharma, A., P. Verwilst, M. Li, D. Ma, N. Singh, J. Yoo, Y. Kim, Y. Yang, J.H. Zhu, H. Huang, X.L. Hu, X.P. He, L. Zeng, T.D. James, X. Peng, J.L. Sessler, and J.S. Kim, *Theranostic Fluorescent Probes.* Chemical Reviews, 2024. **124**(5): p. 2699-2804.
[215] Ma, Y., M. Song, L. Li, X. Lao, Y. Liu, M.-c. Wong, M. Yang, H. Chen, J.J.B. Hao, and Bioelectronics, *Attomolar-level detection of respiratory virus long-chain oligonucleotides based on FRET biosensor with upconversion nanoparticles and Au–Au dimer.* Biosensors and Bioelectronics 2024. **243**: p. 115778.
[216] Catingan, S.D. and A. Moores, *Recent Progress in Surface-Enhanced Fluorescence Using Gold Nanorods.* Acs Applied Nano Materials, 2024.
[217] Acharya, R., T.V. Patil, S.D. Dutta, J. Lee, K. Ganguly, H. Kim, A. Randhawa, and K.T.J.A.M.T. Lim, *Single-Walled Carbon Nanotube-Based Optical Nano/Biosensors for Biomedical Applications: Role in Bioimaging, Disease Diagnosis, and Biomarkers Detection.* Advanced Materials Technologies, 2024: p. 2400279.
[218] Raghunathan, M., A. Kapoor, A. Mohammad, P. Kumar, R. Singh, S.C. Tripathi, K. Muzammil, and D.B.J.L. Pal, *Advances in two-dimensional transition metal dichalcogenides-based sensors for environmental, food, and biomedical analysis: A review.* Luminescence, 2024. **39**(3): p. e4703.
[219] Song, K., X.M. Su, W. Zhao, F.J. Ai, A. Umar, and S. Baskoutas, *Functional inorganic nanomaterials for optical cancer theranostics.* Chemical Engineering Journal, 2024. **485**: p. 150067.
[220] Parvin, N., Q. Jin, Y. Wei, R. Yu, B. Zheng, L. Huang, Y. Zhang, L. Wang, H. Zhang, M. Gao, H. Zhao, W. Hu, Y. Li, and D. Wang, *Few-Layer Graphdiyne Nanosheets Applied for Multiplexed Real-Time DNA Detection.* Advanced materials, 2017. **29**(18): p. 1606755.
[221] Davami, A. and M. Aarabi, *Effect of MoS_2 and (phosphorene, germanene, borophene) hybrid structure on the performance of an SPR biosensor for detection of bacteria.* Optical Review, 2024: p. 1-10.
[222] Jiang, S., S. Butler, E. Bianco, O.D. Restrepo, W. Windl, and J.E. Goldberger, *Improving the stability and optical properties of germanane via one-step covalent methyl-termination.* Nature Communications, 2014. **5**(1): p. 3389.
[223] Ang, W.L., J. Sturala, N. Antonatos, Z. Sofer, and A. Bonanni, *Effect of surface chemistry on bio-conjugation and bio-recognition abilities of 2D germanene materials.* Nanoscale, 2021. **13**(3): p. 1893-1903.
[224] Xue, T., S.R. Bongu, H. Huang, W. Liang, Y. Wang, F. Zhang, Z. Liu, Y. Zhang, H. Zhang, and X. Cui, *Ultrasensitive detection of microRNA using a bismuthene-enabled fluorescence quenching biosensor.* Chemical Communications, 2020. **56**(51): p. 7041-

7044.
[225] Zhao, C., Z. Wang, P. Yu, F. Zhang, and X. Xu, *High performance 1.9 μm passively Q-switched bulk laser with germanene as a saturable absorber.* Optics Express, 2023. **31**(15): p. 24717-24729.
[226] Guo, Y.Q., Y.C. Zhao, S.L. Wang, C. Jiang, and J.Y. Zhang, *Relationship between the zeta potential and the chemical agglomeration efficiency of fine particles in flue gas during coal combustion.* Fuel, 2018. **215**: p. 756-765.
[227] Jia, Q.Q., H.M. Ji, and X. Bai, *Selective sensing property of triclinic WO nanosheets towards ultra-low concentration of acetone.* Journal of Materials Science-Materials in Electronics, 2019. **30**(8): p. 7824-7833.
[228] Liu, Y., P. Bhattarai, Z. Dai, and X. Chen, *Photothermal therapy and photoacoustic imaging via nanotheranostics in fighting cancer.* Chemical Society Reviews, 2019. **48**(7): p. 2053-2108.
[229] Nam, J., S. Son, L.J. Ochyl, R. Kuai, A. Schwendeman, and J.J. Moon, *Chemo-photothermal therapy combination elicits anti-tumor immunity against advanced metastatic cancer.* Nature communications, 2018. **9**(1): p. 1074.
[230] Wang, S., L. Zhang, J. Zhao, M. He, Y. Huang, and S. Zhao, *A tumor microenvironment–induced absorption red-shifted polymer nanoparticle for simultaneously activated photoacoustic imaging and photothermal therapy.* Science Advances, 2021. **7**(12): p. eabe3588.
[231] Liu, Y., K. Ai, J. Liu, M. Deng, Y. He, and L. Lu, *Dopamine-melanin colloidal nanospheres: an efficient near-infrared photothermal therapeutic agent for in vivo cancer therapy.* Advanced materials, 2013. **25**(9): p. 1353-1359.
[232] Yan, J., B. Li, P. Yang, J. Lin, and Y. Dai, *Progress in light-responsive lanthanide nanoparticles toward deep tumor theranostics.* Advanced Functional Materials, 2021. **31**(42): p. 2104325.
[233] Yin, B., W.K.H. Ho, X. Xia, C.K.W. Chan, Q. Zhang, Y.M. Ng, C.Y.K. Lam, J.C.W. Cheung, J. Wang, M. Yang, and S.H.D. Wong, *A Multilayered Mesoporous Gold Nanoarchitecture for Ultraeffective Near-Infrared Light-Controlled Chemo/Photothermal Therapy for Cancer Guided by SERS Imaging.* Small, 2023. **19**(6): p. 2206762.
[234] Yan, B., C. Liu, S. Wang, H. Li, J. Jiao, W.S.V. Lee, S. Zhang, Y. Hou, Y. Hou, X. Ma, H. Fan, Y. Lv, and X. Liu, *Magnetic hyperthermia induces effective and genuine immunogenic tumor cell death with respect to exogenous heating.* Journal of Materials Chemistry B, 2022. **10**(28): p. 5364-5374.
[235] Cui, X., Q. Ruan, X. Zhuo, X. Xia, J. Hu, R. Fu, Y. Li, J. Wang, and H. Xu, *Photothermal Nanomaterials: A Powerful Light-to-Heat Converter.* Chemical Reviews, 2023. **123**(11): p. 6891-6952.
[236] Kang, X., Y. Zhang, J. Song, L. Wang, W. Li, J. Qi, and B.Z. Tang, *A photo-triggered self-accelerated nanoplatform for multifunctional image-guided combination cancer immunotherapy.* Nature Communications, 2023. **14**(1): p. 5216.
[237] Krysko, D.V., A.D. Garg, A. Kaczmarek, O. Krysko, P. Agostinis, and P.J.N.r.c.

Vandenabeele, *Immunogenic cell death and DAMPs in cancer therapy.* 2012. **12**(12): p. 860-875.

[238] Krysko, D.V., A.D. Garg, A. Kaczmarek, O. Krysko, P. Agostinis, and P. Vandenabeele, *Immunogenic cell death and DAMPs in cancer therapy.* Nature Reviews Cancer, 2012. **12**(12): p. 860-875.

[239] Sen, S., M. Won, M.S. Levine, Y. Noh, A.C. Sedgwick, J.S. Kim, J.L. Sessler, and J.F. Arambula, *Metal-based anticancer agents as immunogenic cell death inducers: the past, present, and future.* Chemical Society Reviews, 2022. **51**(4): p. 1212-1233.

[240] Li, H., Q. Luo, H. Zhang, X. Ma, Z. Gu, Q. Gong, and K. Luo, *Nanomedicine embraces cancer radio-immunotherapy: mechanism, design, recent advances, and clinical translation.* Chemical Society Reviews, 2023. **52**(1): p. 47-96.

[241] Hu, K., L. Xie, Y. Zhang, M. Hanyu, Z. Yang, K. Nagatsu, H. Suzuki, J. Ouyang, X. Ji, J. Wei, H. Xu, O.C. Farokhzad, S.H. Liang, L. Wang, W. Tao, and M.-R. Zhang, *Marriage of black phosphorus and Cu2+ as effective photothermal agents for PET-guided combination cancer therapy.* Nature Communications, 2020. **11**(1): p. 2778.

[242] Huang, X., Y. Lu, M. Guo, S. Du, and N. Han, *Recent strategies for nano-based PTT combined with immunotherapy: from a biomaterial point of view.* Theranostics, 2021. **11**(15): p. 7546-7569.

[243] Hu, K., L. Xie, Y. Zhang, M. Hanyu, Z. Yang, K. Nagatsu, H. Suzuki, J. Ouyang, X. Ji, J. Wei, H. Xu, O.C. Farokhzad, S.H. Liang, L. Wang, W. Tao, and M.R. Zhang, *Marriage of black phosphorus and Cu(2+) as effective photothermal agents for PET-guided combination cancer therapy.* Nat Commun, 2020. **11**(1): p. 2778.

[244] Liu, S., X. Pan, and H. Liu, *Two-dimensional nanomaterials for photothermal therapy.* Angewandte Chemie, 2020. **132**(15): p. 5943-5953.

[245] Zhao, F., Y. Feng, and W. Feng, *Germanium-based monoelemental and binary two-dimensional materials: Theoretical and experimental investigations and promising applications.* InfoMat, 2022. **4**(11): p. e12365.

[246] Fusco, L., A. Gazzi, G. Peng, Y. Shin, S. Vranic, D. Bedognetti, F. Vitale, A. Yilmazer, X. Feng, B. Fadeel, C. Casiraghi, and L.G. Delogu, *Graphene and other 2D materials: a multidisciplinary analysis to uncover the hidden potential as cancer theranostics.* Theranostics, 2020. **10**(12): p. 5435-5488.

[247] Ren, X., W. Liu, H. Zhou, J. Wei, C. Mu, Y. Wan, X. Yang, A. Nie, Z. Liu, X. Yang, and Z. Luo, *Biodegradable 2D GeP nanosheets with high photothermal conversion efficiency for multimodal cancer theranostics.* Chemical Engineering Journal, 2022. **431**: p. 134176.

[248] Feng, C., J. Ouyang, Z. Tang, N. Kong, Y. Liu, L. Fu, X. Ji, T. Xie, O.C. Farokhzad, and W. Tao, *Germanene-Based Theranostic Materials for Surgical Adjuvant Treatment: Inhibiting Tumor Recurrence and Wound Infection.* Matter, 2020. **3**(1): p. 127-144.

[249] Rosli, N.F., N. Rohaizad, J. Sturala, A.C. Fisher, R.D. Webster, and M. Pumera, *Siloxene, Germanane, and Methylgermanane: Functionalized 2D Materials of Group 14 for Electrochemical Applications.* Advanced Functional Materials, 2020. **30**(21): p. 1910186.

[250] Ge, M., M. Zong, D. Xu, Z. Chen, J. Yang, H. Yao, C. Wei, Y. Chen, H. Lin, and J. Shi, *Freestanding germanene nanosheets for rapid degradation and photothermal conversion.*

Materials Today Nano, 2021. **15**: p. 100119.
[251] Liu, Z., Y. Dai, Z. Zheng, and B. Huang, *Covalently-terminated germanane GeH and GeCH3 for hydrogen generation from catalytic hydrolysis of ammonia borane under visible light irradiation.* Catalysis Communications, 2019. **118**: p. 46-50.
[252] Molle, A., J. Goldberger, M. Houssa, Y. Xu, S.-C. Zhang, and D. Akinwande, *Buckled two-dimensional Xene sheets.* Nature Materials, 2017. **16**(2): p. 163-169.
[253] Ye, X.-S., Z.-G. Shao, H. Zhao, L. Yang, and C.-L. Wang, *Intrinsic carrier mobility of germanene is larger than graphene's: first-principle calculations.* RSC Advances, 2014. **4**(41): p. 21216-21220.
[254] Cho, J.M., J. Chae, S.R. Jeong, M.J. Moon, D.Y. Shin, and J.H. Lee, *Immune activation of Bio-Germanium in a randomized, double-blind, placebo-controlled clinical trial with 130 human subjects: Therapeutic opportunities from new insights.* PLoS One, 2020. **15**(10): p. e0240358.
[255] Bellani, S., A. Bartolotta, A. Agresti, G. Calogero, G. Grancini, A. Di Carlo, E. Kymakis, and F. Bonaccorso, *Solution-processed two-dimensional materials for next-generation photovoltaics.* Chemical Society Reviews, 2021. **50**(21): p. 11870-11965.
[256] Wu, B., J. Liang, X. Yang, Y. Fang, N. Kong, D. Chen, and H. Wang, *A Programmable Peptidic Hydrogel Adjuvant for Personalized Immunotherapy in Resected Stage Tumors.* Journal of the American Chemical Society, 2024. **146**(12): p. 8585-8597.
[257] Liu, M., Y. Ishida, Y. Ebina, T. Sasaki, T. Hikima, M. Takata, and T. Aida, *An anisotropic hydrogel with electrostatic repulsion between cofacially aligned nanosheets.* Nature, 2015. **517**(7532): p. 68-72.
[258] Yu, Z., J. Guo, M. Hu, Y. Gao, and L. Huang, *Icaritin Exacerbates Mitophagy and Synergizes with Doxorubicin to Induce Immunogenic Cell Death in Hepatocellular Carcinoma.* ACS Nano, 2020. **14**(4): p. 4816-4828.
[259] Zhu, Y.-X., H.-R. Jia, G. Gao, G.-Y. Pan, Y.-W. Jiang, P. Li, N. Zhou, C. Li, C. She, N.W. Ulrich, Z. Chen, and F.-G. Wu, *Mitochondria-acting nanomicelles for destruction of cancer cells via excessive mitophagy/autophagy-driven lethal energy depletion and phototherapy.* Biomaterials, 2020. **232**: p. 119668.
[260] Jeong, S.D., B.-K. Jung, H.M. Ahn, D. Lee, J. Ha, I. Noh, C.-O. Yun, and Y.-C. Kim, *Immunogenic Cell Death Inducing Fluorinated Mitochondria-Disrupting Helical Polypeptide Synergizes with PD-L1 Immune Checkpoint Blockade.* Advanced Science, 2021. **8**(7): p. 2001308.
[261] Mekahli, D., G. Bultynck, J.B. Parys, H. De Smedt, and L. Missiaen, *Endoplasmic-reticulum calcium depletion and disease.* Cold Spring Harb Perspect Biol, 2011. **3**(6).
[262] Raffaello, A., C. Mammucari, G. Gherardi, and R. Rizzuto, *Calcium at the Center of Cell Signaling: Interplay between Endoplasmic Reticulum, Mitochondria, and Lysosomes.* Trends in Biochemical Sciences, 2016. **41**(12): p. 1035-1049.
[263] Liu, X., B. Li, F. Fu, K. Xu, R. Zou, Q. Wang, B. Zhang, Z. Chen, and J. Hu, *Facile synthesis of biocompatible cysteine-coated CuS nanoparticles with high photothermal conversion efficiency for cancer therapy.* Dalton Transactions, 2014. **43**(30): p. 11709-15.
[264] Tian, Q., F. Jiang, R. Zou, Q. Liu, Z. Chen, M. Zhu, S. Yang, J. Wang, J. Wang, and J. Hu,

Hydrophilic Cu9S5 nanocrystals: a photothermal agent with a 25.7% heat conversion efficiency for photothermal ablation of cancer cells in vivo. ACS Nano, 2011. **5**(12): p. 9761-71.

[265] Sun, S., Y. Song, J. Chen, M. Huo, Y. Chen, and L. Sun, *NIR -I and NIR-II irradiation tumor ablation using NbS(2) nanosheets as the photothermal agent.* Nanoscale, 2021. **13**(43): p. 18300-18310.

[266] Liu, Z.H., Y. Dai, Z.K. Zheng, and B.B. Huang, *Covalently-terminated germanane GeH and GeCH*

for hydrogen generation from catalytic hydrolysis of ammonia borane under visible light irradiation. Catalysis Communications, 2019. **118**: p. 46-50.

[267] Chou, S.S., B. Kaehr, J. Kim, B.M. Foley, M. De, P.E. Hopkins, J. Huang, C.J. Brinker, and V.P. Dravid, *Chemically Exfoliated MoS2 as Near-Infrared Photothermal Agents.* 2013. **52**(15): p. 4160-4164.

[268] Xie, H., Z. Li, Z. Sun, J. Shao, X.-F. Yu, Z. Guo, J. Wang, Q. Xiao, H. Wang, Q.-Q. Wang, H. Zhang, and P.K. Chu, *Metabolizable Ultrathin Bi2Se3 Nanosheets in Imaging-Guided Photothermal Therapy.* 2016. **12**(30): p. 4136-4145.

[269] Yang, Z., R. Cheng, C. Zhao, N. Sun, H. Luo, Y. Chen, Z. Liu, X. Li, J. Liu, and Z. Tian, *Thermo- and pH-dual responsive polymeric micelles with upper critical solution temperature behavior for photoacoustic imaging-guided synergistic chemo-photothermal therapy against subcutaneous and metastatic breast tumors.* Theranostics, 2018. **8**(15): p. 4097-4115.

[270] Peng, L., X. Mei, J. He, J. Xu, W. Zhang, R. Liang, M. Wei, D.G. Evans, and X. Duan, *Monolayer Nanosheets with an Extremely High Drug Loading toward Controlled Delivery and Cancer Theranostics.* Advanced Materials, 2018. **30**(16): p. 1707389.

[271] Ma, N., M.K. Zhang, X.S. Wang, L. Zhang, J. Feng, and X.Z. Zhang, *NIR Light-Triggered Degradable MoTe2Nanosheets for Combined Photothermal and Chemotherapy of Cancer.* Advanced Functional Materials, 2018. **28**(31).

[272] Zhu, Y., Y. Wang, G.R. Williams, L. Fu, J. Wu, H. Wang, R. Liang, X. Weng, and M. Wei, *Multicomponent Transition Metal Dichalcogenide Nanosheets for Imaging-Guided Photothermal and Chemodynamic Therapy.* Advanced Science, 2020. **7**(23): p. 2000272.

[273] Li, X., D. Xi, M. Yang, W. Sun, X. Peng, and J. Fan, *An Organic Nanotherapeutic Agent Self-Assembled from Cyanine and Cu (II) for Combined Photothermal and Chemodynamic Therapy.* Advanced Healthcare Materials, 2021. **10**(20): p. e2101008.

[274] Hu, R.Z., C. Dai, C.M. Wang, J. Lin, H. Hu, Z.F. Li, H. Lin, L. Ding, Y. Chen, and B. Zhang, *Engineering 2D Arsenic-Phosphorus Theranostic Nanosheets.* Advanced Functional Materials, 2021. **31**(25): p. 2101660.

[275] Lei, Z., W. Zhu, S. Xu, J. Ding, J. Wan, and P. Wu, *Hydrophilic MoSe2 Nanosheets as Effective Photothermal Therapy Agents and Their Application in Smart Devices.* ACS Appl Mater Interfaces, 2016. **8**(32): p. 20900-8.

[276] Xu, D.Q., X.J. He, E. Obeng, Z.Y. Ye, J.L. Shen, and X. Ding, *Two-dimensional NbS nanosheets with hyperthermia for killing bacteria to promote infected wound healing.* Materials & Design, 2022. **223**: p. 111124.

[277] Jia, C., F. Zhang, J. Lin, L. Feng, T. Wang, Y. Feng, F. Yuan, Y. Mai, X. Zeng, and Q. Zhang, *Black phosphorus-Au-thiosugar nanosheets mediated photothermal induced anti-tumor effect enhancement by promoting infiltration of NK cells in hepatocellular carcinoma.* Journal of Nanobiotechnology, 2022. **20**(1): p. 90.

[278] Yu, J., W. Yin, X. Zheng, G. Tian, X. Zhang, T. Bao, X. Dong, Z. Wang, Z. Gu, X. Ma, and Y. Zhao, *Smart MoS2/Fe3O4 Nanotheranostic for Magnetically Targeted Photothermal Therapy Guided by Magnetic Resonance/Photoacoustic Imaging.* Theranostics, 2015. **5**(9): p. 931-45.

[279] Chng, E.L., Z. Sofer, and M. Pumera, *MoS(2) exhibits stronger toxicity with increased exfoliation.* Nanoscale, 2014. **6**(23): p. 14412-8.

[280] Zhu, H., Z. Lai, Y. Fang, X. Zhen, C. Tan, X. Qi, D. Ding, P. Chen, H. Zhang, and K. Pu, *Ternary Chalcogenide Nanosheets with Ultrahigh Photothermal Conversion Efficiency for Photoacoustic Theranostics.* Small, 2017. **13**(16).

[281] Zhu, H., Z. Lai, Y. Fang, X. Zhen, C. Tan, X. Qi, D. Ding, P. Chen, H. Zhang, and K. Pu, *Ternary Chalcogenide Nanosheets with Ultrahigh Photothermal Conversion Efficiency for Photoacoustic Theranostics.* Small, 2017. **13**(16): p. 1604139.

[282] Xu, D., J. Liu, Y. Wang, Y. Jian, W. Wu, and R. Lv, *Black Phosphorus Nanosheet with High Thermal Conversion Efficiency for Photodynamic/Photothermal/Immunotherapy.* ACS Biomaterials Science & Engineering, 2020. **6**(9): p. 4940-4948.

[283] Ren, X.N., W.L. Liu, H.J. Zhou, J.S. Wei, C.P. Mu, Y. Wan, X.Q. Yang, A.M. Nie, Z.Y. Liu, X.L. Yang, and Z.Q. Luo, *Biodegradable 2D GeP nanosheets with high photothermal conversion efficiency for multimodal cancer theranostics.* Chemical Engineering Journal, 2022. **431**: p. 134176.

[284] Zheng, P., B. Ding, Z. Jiang, W. Xu, G. Li, J. Ding, and X. Chen, *Ultrasound-Augmented Mitochondrial Calcium Ion Overload by Calcium Nanomodulator to Induce Immunogenic Cell Death.* Nano Letters, 2021. **21**(5): p. 2088-2093.

[285] Chen, R., R. Kang, and D. Tang, *The mechanism of HMGB1 secretion and release.* Experimental & Molecular Medicine, 2022. **54**(2): p. 91-102.

[286] Bianchi, M.E., M.P. Crippa, A.A. Manfredi, R. Mezzapelle, P. Rovere Querini, and E. Venereau, *High-mobility group box 1 protein orchestrates responses to tissue damage via inflammation, innate and adaptive immunity, and tissue repair.* Immunological Reviews, 2017. **280**(1): p. 74-82.

[287] Sun, Y., Y. Liu, X. Ma, and H. Hu, *The Influence of Cell Cycle Regulation on Chemotherapy.* International Journal of Molecular Sciences, 2021. **22**(13).

[288] Feng, B., F. Zhou, B. Hou, D. Wang, T. Wang, Y. Fu, Y. Ma, H. Yu, and Y. Li, *Binary Cooperative Prodrug Nanoparticles Improve Immunotherapy by Synergistically Modulating Immune Tumor Microenvironment.* Advanced Materials, 2018. **30**(38): p. 1803001.

[289] Tanaka, T., M. Narazaki, and T. Kishimoto, *IL-6 in inflammation, immunity, and disease.* Cold Spring Harb Perspect Biol 2014. **6**(10): p. a016295.

[290] Almanza, A., A. Carlesso, C. Chintha, S. Creedican, D. Doultsinos, B. Leuzzi, A. Luís, N. McCarthy, L. Montibeller, S. More, A. Papaioannou, F. Püschel, M.L. Sassano, J. Skoko,

P. Agostinis, J. de Belleroche, L.A. Eriksson, S. Fulda, A.M. Gorman, S. Healy, A. Kozlov, C. Muñoz-Pinedo, M. Rehm, E. Chevet, and A. Samali, *Endoplasmic reticulum stress signalling - from basic mechanisms to clinical applications.* Febs j, 2019. **286**(2): p. 241-278.

[291] Pessa, J.C., J. Joutsen, and L. Sistonen, *Transcriptional reprogramming at the intersection of the heat shock response and proteostasis.* Molecular Cell, 2024. **84**(1): p. 80-93.

[292] Luo, B. and A.S. Lee, *The critical roles of endoplasmic reticulum chaperones and unfolded protein response in tumorigenesis and anticancer therapies.* Oncogene, 2013. **32**(7): p. 805-18.

[293] Feng, S., H. Li, Y. Tai, J. Huang, Y. Su, J. Abramowitz, M.X. Zhu, L. Birnbaumer, and Y. Wang, *Canonical transient receptor potential 3 channels regulate mitochondrial calcium uptake.* Proceedings of the National Academy of Sciences, 2013. **110**(27): p. 11011-11016.

[294] Pinton, P., C. Giorgi, R. Siviero, E. Zecchini, and R. Rizzuto, *Calcium and apoptosis: ER-mitochondria Ca2+ transfer in the control of apoptosis.* Oncogene, 2008. **27**(50): p. 6407-18.

[295] Huang, Y., Q. Zhang, C.Y.K. Lam, C. Li, C. Yang, Z. Zhong, R. Zhang, J. Yan, J. Chen, B. Yin, S.H.D. Wong, and M. Yang, *An Aggregation-Induced Emission-Based Dual Emitting Nanoprobe for Detecting Intracellular pH and Unravelling Metabolic Variations in Differentiating Lymphocytes.* ACS Nano, 2024. **18**(24): p. 15935-15949.

[296] Luckheeram, R.V., R. Zhou, A.D. Verma, and B. Xia, *CD4(+)T cells: differentiation and functions.* Clinical and Developmental Immunology, 2012. **2012**: p. 925135.

[297] Wu, J., J. Chen, Y. Feng, S. Zhang, L. Lin, Z. Guo, P. Sun, C. Xu, H. Tian, and X. Chen, *An immune cocktail therapy to realize multiple boosting of the cancer-immunity cycle by combination of drug/gene delivery nanoparticles.* Science Advances, 2020. **6**(40): p. eabc7828.

[298] Tanaka, A. and S. Sakaguchi, *Regulatory T cells in cancer immunotherapy.* Cell Research, 2017. **27**(1): p. 109-118.